Santiago Sanchez

Stability Investigation of Power Electronics Systems

A Microgrid Case

Thesis for the degree of Philosophiae Doctor

Trondheim, March 2015

Norwegian University of Science and Technology
Faculty of Information Technology,
Mathematics and Electrical Engineering
Department of Electric Power Engineering

NTNU – Trondheim
Norwegian University of
Science and Technology

NTNU
Norwegian University of Science and Technology

Thesis for the degree of Philosophiae Doctor

Faculty of Information Technology, Mathematics and Electrical Engineering
Department of Electric Power Engineering

ISBN 978-82-326-0658-0 (printed ver.)
ISBN 978-82-326-0659-7 (electronic ver.)
ISSN 1503-8181

Doctoral theses at NTNU, 2015:2

Printed by NTNU Grafisk senter

Contents

List of Figures

List of Tables

Abbreviations

AC alternative current

CIGRE Conseil International des Grands Reseaux Electriques

CPL Constant power load

DC Direct current

DG Distributed generator

ES Energy storage

IEEE Institute of Electrical and Electronics Engineers

KF Kalman filter

PEX Power exchanger device

PI Proportional integral controller

PLL Phase locked loop

PV Photo-voltaic system

PWM Pulse width modulation

RES Renewable energy source

RLSE Recursive least squares estimator

VSC Voltage source converter

VSI Voltage source inverter

Abstract

This thesis is focused on the stability of systems containing high power electronic devices. The study mainly involves the exchanger device in a hybrid current microgrid. This microgrid has a topology with a DC bus and an AC bus. The stability analysis was performed for a small signal during short- and long-term perturbation. The short-term tests are presented in the frequency domain with the Nyquist stability criteria. This method has several practical advantages that facilitate its implementation. The long-term tests use eigenvalues and a semi-recursive method to estimate the low frequency equivalent of the microgrid. A continuation method has been applied to analyze the stability of the system with the full information about the microgrid. The loadability and controllability of the system has been tested with this method.

Acknowledgements

I would like to thank first to my supervisor Professor Marta Molinas for all her guidance. The Department of Electrical Power Engineering at Norwegian University of Science and Technology.

Thanks to my family for all their support, my girlfriend Emma for all her help.

I would also thank to my friends at NTNU, Trondheim and around the world.

Chapter 1

Introduction

The aim of this chapter is to describe the reasons for this research and to state its objectives. The state of the art in micro-grids and stability of systems with high power electronic devices is also presented, and the contributions are highlighted. The chapter also describes the problem and the methodology used to solve it.

Energy in future distribution systems will come from renewable and non-renewable sources as well as energy storage (ES) devices [4–6]. These types of system will power electronic devices to link the sources or loads with the electrical grid. Such distribution systems are promising to develop into what can be defined as an interaction of multiple micro-grids (i.e. a cluster of them). A microgrid is a small electrical network operated in isolation from the main grid (See below for a full definition). This isolated network comprises sufficient generating resources, and operates in a deliberate and controlled way [7].

An electrical power system at distribution level fed by renewable energy sources (RES) is a good way to use available clean energy. In addition, more and more distributed generation devices (DG) that capture a particular type of renewable energy and converts it to electrical energy are being installed at homes or buildings. Most of these DG inject the power generated into the distribution grid through power electronic systems. This type of grid, called a micro-grid, is defined as an autonomous grid that has a set of generation devices, storage systems and loads. They are connected to the same low or medium voltage grid. Micro-grids can also operate connected or islanded from the main distribution system [8].

The increased application of power electronic devices in DGs at the distribution level has resulted in the addition of new types of non-linearities to the system dynamics. Furthermore, these new properties can result in unknown be-

haviour in this new class of power systems leading to possible lost of stability. It is important to study the aggregated effect of a large number of power electronic devices in the distribution systems based on existent AC topologies as well as new hybrid AC-DC buses. The correct and safe operation of the microgrid has to be ensured. The analysis of stable behavior is important to ensure the correct operation of the microgrid. Therefore, stability is the main area of study in this thesis. Consequently, it is necessary to identify the characteristics that influence the stability of microgrids with devices based on power electronics.

1.0.1 Hypothesis

Systems formed by the aggregation of power electronic devices that interconnect renewable and nonrenewable energy sources first have non-linear dynamics because of their switched behavior. This type of device can be controlled with both linear and non-linear methods, which adds complexity to the dynamic. It can be assumed that a system with many aggregated power electronic devices will also be non-linear. However, non-linear phenomena associated with these aggregated systems have not been reported. Additionally, power electronic systems do not have inertia, in contrast with classical power systems which do. Therefore, the damping of oscillations resulting from the inertia in systems based on electrical machines are not present in power electronic systems, and it is necessary to identify new properties in the behavior of the new system. One approach is to analyze aggregated power electronics with an equivalent dynamic system, in the form of an equivalent impedance.

1.1 Objectives

1.1.1 General

The main objective of the research is to identify the phenomena that affect the stability of a micro-grid fed by multiple renewable energy sources, non renewable energy sources and loads with power electronic interfaces.

1.1.2 Specific

- To classify and to model by simulation the micro-grid structures suitable for the future operation of the distribution system.
- To select the most accurate modeling methodologies for a power electronics system with renewable energy sources.
- To verify the theoretical model obtained by an experimental test.

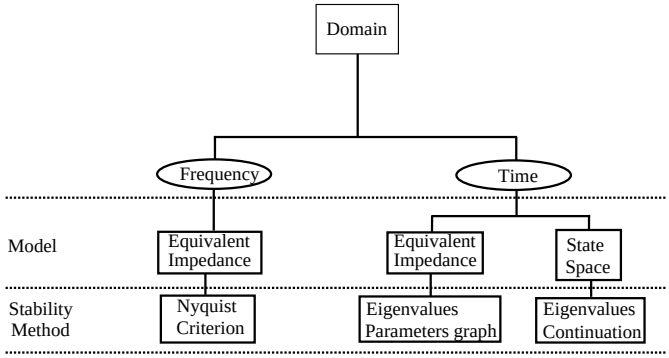

Figure 1.1: Methodology diagram.

- To select techniques to study the stability of microgrids.
- To determine the degree of influence of the parameters and devices on the stability.
- To determine by simulation the potential relevant sources of instability in the micro-grids to establish design guidelines that can guarantee system stability.

1.2 Description of the problem and methodology

The Thesis was developed to determine the models and the techniques to study the stability of a distribution voltage level microgrid based on power electronics devices for two cases. Figure 1.1 shows the model and stability method required depending on the domain of representation. In the first part, the information of these devices is not available and they are considered as black-boxes, and in the second part, all information about the devices and network connection is available.

The research was developed to study the stability at the interconnection points of a voltage source converter (*i.e. the DC and AC sides*). This system is used in the microgrid to link the DC with the AC buses. Hence, two main analysis have been considered: small signal stability study with short- and long-term problems.

The first part of this research presents the small signal stability study and the theory of impedance representation at the coupling point of the converter with the microgrid [9]. The stability test uses the Nyquist criteria [10, 11].

The second part takes into account the problem of long-term signal stability at the DC coupling point in the microgrid. Here, the condition of existence of equilibria of systems with loads consuming constant power has been stated, as described in [12], and the stability tested using a representation of the microgrid with a Thevenin's equivalent circuit in the time domain [13]. This equivalent is coupled with the long-term signal representation of the constant power load, *i.e.* the converter used to connect the DC and AC buses of the microgrid. The inner loop dynamics has been neglected, *i.e.* current or voltage controllers [14]. The stability test then uses the eigenvalues of this reduced system to obtain a set of boundary curves.

The third part of this research examines how the transition of the system states influences the stability of a DC microgrid [15]. The methodology uses the continuation algorithm for fixed points [3]. Information about the microgrid topology and parameters is necessary to apply the method. Finally, the use of eigenvalues for each point in the state-parameter space defines the stability or instability of the system.

This theoretical approach complemented with experimental results for short- and long-term dynamics of power electronic converters.

1.3 State of the art

Some authors have proposed a coordinate operation for the micro-grid. Sophisticated communication systems are required to control the generation/storage and to maintain a constant voltage and frequency [16–18]; some of the information required is the forecast of the demanded load, fuel prices (for thermal distributed generation), and physical constraints. A second option is to operate the micro-grid like a primary controller of a conventional power system, which does not require communication between the distributed generation elements and uses droop control to maintain safe operation [19]. With this method, communication involving supervisory control can be applied to the outer loops. The reference signals can be sent from the supervisor to each of the sources of the system. This is in order to improve the grid response, as occurs in hierarchical control.

The microgrid can have different structures. One of its structures involves the interconnection of the DG, storage systems and loads to a DC bus [4, 20–23] (Fig. 1.2). For distribution systems with AC coupling points, the radial and ring configurations can be adopted as the structure of the micro-grid [7, 24]. Another

structure that uses AC and DC buses, which are connected through a AC/DC bidirectional power electronic coupler is presented in [25].

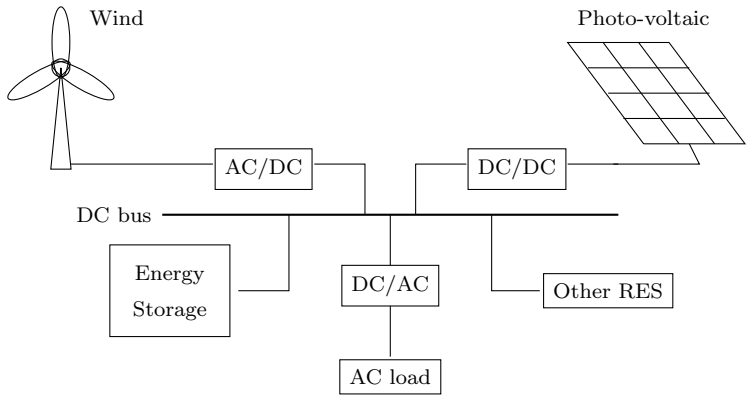

Figure 1.2: Typical DC microgrid structure in isolation mode.

Micro-grid structures are relatively new; thus, their stability has been substantially less investigated than that of their predecessor, the classical power system. The DG based on power electronic devices adds new properties to the system such as discrete operation, which in turn introduces a new type of non-linearity. In addition, the DG lacks physical inertia and the dynamics of the controller determine the behavior of the power electronic devices in the system, and also affects the properties of the energy sources behind the power electronic devices. Little is known about the combined effect of these properties when the power electronics devices are interacting with one another in the same system. Indeed, the range of potential phenomena has not been yet identified. Some of these properties have been investigated in isolation by some authors using different levels of assumptions and simplifications for modelling the components of the system. Most of these studies have assumed ideal conditions for the analysis of the components because they are more concerned with the functionality of individual components than with the overall influence of such components in the system.

The linear stability of DC systems has been analyzed in [11, 26–28], and the continuous monitoring of small signal stability was proposed in [29]. In this analysis, the stability is monitored and prevent from crossing a frequency response margin criteria that uses the current or the voltage as parameters. In [10], a review of the methods used to analyze the stability of systems with electronic devices is presented. One of the method is phasor modeling of electronic circuits, which takes into consideration firing angle and harmonics, but this in turn makes the

models larger and more complex. Another method used in [30] involves the analysis of the system on the *dq* reference frame. This method averages the duty ratio, linearizes the system around an operation point, and applies generalized Nyquist criteria with a matrix representation. A third method is reduced order modeling, which is described in [31]. This is tested on an inverter and describes the AC output impedance. In [31] the resulting impedance (i. e. the frequency response) depended mainly on the transfer function of the controller. Finally [32–36] describe a technique for modeling the small-signal input impedance of line frequency AC-DC converters for the purpose of linear stability analyses such as the Nyquist criteria. The method uses harmonic linearization and Fourier analysis. Several studies have also used linear analysis to study the instability derived from converter control-grid interactions, or from a constant power behavior [20, 37–39].

Power electronic systems add fast non-linear dynamics to the micro-grid. These non-linear dynamics have not yet been characterized and the nature of these nonlinearities compared to the nonlinearities of classical power system is not well known. These systems can excite resonance, which, if sustained or under damped can lead to grid failure. Hence, some designs of power electronic devices include non-linear analysis by introducing bifurcation theory. The stability boundary of a dynamic voltage restorer, taking into account the variation of the switching function, and the distribution static compensator without considering the switching function, is shown in [40, 41].

1.3.1 Gaps in the state of the art

Previous studies have provided tools to assess the stability of individual power electronic devices at the connection node with other power system. The thesis identifies the following unresolved issues that need to be addressed.

- Electrical networks present different topologies and voltage level characteristics. One of the objectives of this thesis is to identify a possible microgrid distribution level system that presents similar characteristics as the classical distribution power system, in which renewable DG are the main energy source.
- None of the publications listed above reports the stability of a microgrid with DC-AC buses in which the DGs are the main sources of the system.
- It is necessary to identify the advantages and disadvantages of stability techniques for short and long term representations of microgrids with DGs based on power electronic devices.

- Unfortunately, many of the publications reporting stability studies do not include a detailed analysis of influence of the loadability and controllers applied to the power electronics devices in a microgrid.

1.4 Contributions

The contributions can be summarized as follows.

- A microgrid system was designed to test and to verify the stability analysis method by the frequency and time domain techniques. This microgrid has a DC and an AC bus, therefore the distributed generators and loads were coupled at these buses [9].
- Small signal representation of the system. The small signal representation was carried out by linear approximation of a system using the concept of harmonic balance. The stability criteria are based on the Nyquist test of the minor loop for a Thevenin or a Norton circuit equivalent [9].
- For the long-term signal representation, a theoretical study was developed to determine the conditions for the existence of equilibrium in systems with constant power loads (CPLs) (*i.e. the power exchange device in the microgrid*) [12].
- An equivalent system of the microgrid at the coupling point of the power exchanger device was also developed for the long-term signal representation by using a semi-recursive parameter estimation of the mentioned equivalent. This estimation of the equivalent impedance is used with the respective representation of the device under test and a map of stability boundaries in the parameter space was developed [13].
- The fast and slow dynamics of a DC-microgrid were analyzed with the application of the known continuation theory [42].

1.5 Scope

The research is based on the study of stability in future systems supplied through power electronics. The stability tests have been performed in a microgrid with DC and AC buses. The coordination algorithms of microgrids are beyond the scope of this Thesis. A master/slave coordination for the converters was used at the DC bus and a frequency and voltage droop control was used for the inverters at the AC bus [43]. This research is focused on:

- Small signal short-term representation at the point of common coupling.
- Small signal short-term stability.
- Long-term stability at the point of common coupling.
- Use of the continuation theory to study the boundaries of stability for loadability and controllability tests.

1.6 List of publications

The results of this project have been published in journals and conference proceedings. The publications are listed below.

1.6.1 Journal papers

- **Sanchez Acevedo, Santiago**; Molinas Cabrera, Maria Marta; Large signal stability analysis at the common coupling point of a DC microgrid: A grid impedance estimation approach based on a recursive method, IEEE Transactions on Energy Conversion, Volume PP, number 99, Pages 1-10, 2014, ISSN 0885-8969.
- **Sanchez Acevedo, Santiago**; Molinas Cabrera, Maria Marta; Degree of influence of system states transition on the stability of a DC microgrid,IEEE Transactions on Smart Grid, Volume 5, number 5, Pages 2535-2542, 2014.
- **Sanchez Acevedo, Santiago**; Ortega, Romeo; Grino, Robert; Bergna, Gilbert; Molinas Cabrera, Maria Marta; Conditions for Existence of Equilibria of Systems With Constant Power Loads, IEEE Transactions on Circuits and Systems I: Regular Papers, July, Volume 61, number 7, 2014.
- **Sanchez Acevedo, Santiago**; Molinas Cabrera, Maria Marta; Degano, Marco; Zanchetta, Pericle, Stability evaluation of a DC micro-grid and future interconnection to an AC system, Renewable Energy, Elsevier, Volume 62, February 2014, Pages 649-656, ISSN 0960-1481.
- **Sanchez Acevedo, Santiago**; Molinas Cabrera, Maria Marta; Identifying Unstable Region of Operation in a Micro-grid System. Energy procedia E journal, Elsevier, Technoport 2012 - Sharing Possibilities and 2nd Renewable Energy Research Conference (RERC2012) pp 1-10, 2012.

Submitted journal papers

- **Sanchez Acevedo, Santiago**; Soolot, Amir; Molinas Cabrera, Maria Marta; Stability analysis of a photo-voltaic and renewable energy systems based on permanent magnet generator: connection to DC nanogrids. Electric Power System Research. Submitted in 2014.

1.6.2 Conference papers

- **Sanchez Acevedo, Santiago**; Molinas Cabrera, Maria Marta. Evaluation of the system parameters degree of influence on the stability of a DC microgrid. In IEEE procedings Powertech 2013, June, Grenoble, France, 2013.

- **Sanchez Acevedo, Santiago**; Molinas Cabrera, Maria Marta. Evaluation of Non-active Current Compensation in Smart Grids, IEEE Innovative Smart Grid Technologies Europe 2012, ISGT-EUROPE (ISBN 978-1-4673-2596-7), pp 1-8, October, 2012.

- Holtsmark, Nathalie; **Sanchez Acevedo, Santiago**; Molinas Cabrera, Maria Marta. Speed regulation of a wind turbine with current source or matrix converter: Tuning procedure. I: IEEE COMPEL 2012: 13th Workshop on Control and Modeling for Power Electronics. IEEE conference proceedings 2012 ISBN 978-1-4244-9373-9. s. 1-6.

- **Sanchez Acevedo, Santiago**; Molinas Cabrera, Maria Marta; Garces, Alejandro. A Current-Coupled Topology for Grid Integration of Wind Turbines in Micro-Grids. Power Energy Society T&D Conference and Exposition 2012 (ISBN:978-1-4673-1933-1); 2012-05-07 - 2012-05-10

- **Sanchez Acevedo, Santiago**; Molinas Cabrera, Maria Marta. "Assessment of a stability analysis tool for constant power loads in dc-grids," in 15TH International power electronics and motion control conference, EPE-PEMC 2012 ECCE Europe, Novid Sad, Serbia, sep. 2012, pp. 1 -5.

- **Sanchez Acevedo, Santiago**; Molinas Cabrera, Maria Marta. "Assessing the validity of a propose stability analysis method in a three phase system with constant power load," in Power Electronics for Distributed Generation Systems (PEDG), 2012 3rd IEEE International Symposium on, june 2012, pp. 41 -45.

- Reza, Parseh; Kansanen, Kimmo; **Sanchez Acevedo, Santiago**; Molinas Cabrera, Maria Marta. Real-Time Compression of Measurements in Distribution Grids, IEEE SmartGridComm 2012 Symposium- Network, 2012.

- **Sanchez Acevedo, Santiago**; Molinas Cabrera, Maria Marta. Modeling of Switching Power Interfaces for Smart-Grid Stability Studies. Innovative Smart Grid Technologies IEEE PES ISGT 2011 Europe (ISBN: 978-1-4577-1422-1); 2011-12-05 - 2011-12-07.
- **Sanchez Acevedo, Santiago**; Molinas Cabrera, Maria Marta. Power Electronics Modeling Fidelity: Impact on Stability Estimate of Micro-grid Systems. IEEE PES Conference on Innovative Smart Grid Technology, Asia (ISGT2011) (ISBN:978-1-4577-0874-9); 2011-11-13 - 2011-11-16

1.6.3 Poster presentations

- **Sanchez Acevedo, Santiago**; Molinas Cabrera, Maria Marta; Garces Ruiz, Alejandro. A current-coupled topology for grid integration of wind turbines in micro-grids. Indian Week- NTNU, Trondheim; 2011-11-05 - 2011-11-07.

1.7 Layout of the thesis

The thesis is organized as follow:

Chapter 2 presents a discussion about distributed generation, the concept of a microgrid and their various topologies. A brief description of stability of dynamic systems is given.

In Chapter 3 the microgrid used as a benchmark in this Thesis is described, and the converters and control loops are also presented.

Chapter 4 investigates small signal short-term stability of the frequency representation of the microgrid equivalent and the device under test. The Nyquist criterion is used to evaluate the stability.

In Chapter 5 the long-term stability is studied. The theory is based on a situation in which information is lacking about the microgrid and the impedance equivalent is required. A recursive parameter estimation technique was applied to solve this problem, in a method resembling a black/gray box approach.

The loadability and controllability tests are described in Chapter 6. The mathematical tool used to study the stability here is the numerical continuation of fixed points.

Finally, the conclusions of this Thesis are presented in Chapter 7.

Chapter 2

Aspects of islanded small scale power systems

This chapter presents a basic description of microgrids, different types of electrical power systems based on microgrids, the promising increase of microgrids at the distribution level, and the control coordinations that can handle this kind of topology. In Addition, the chapter reviews the stability tests used in systems with a high number of interconnected power electronic devices.

2.1 Application of small scale electric power systems

Power systems in ships, aircrafts, communication and data centers use a small power network that can be defined as a microgrid [21, 22, 44, 45]. This type of system uses multiple energy sources, which can be interconnected by power electronics devices. The aim of this setup is to distribute the power coming from the sources into multiple loads in the grid. One of the main characteristics of these systems is the use of multiple generation points very close to the loads, which contrasts with classical transmission networks that are characterized by a long distance between the generation and the load. The hierarchical control philosophy is also another important feature.

2.1.1 Definition of a microgrid

Microgrids have been defined by several authors and working groups [17, 46, 47] as follows:
The microgrid is a small-scale power system composed of distributed generators

(DGs) and loads operated as a collective unit. The energy source of the DGs is solar power, wind power, fuel cells or gas cogeneration. The DG unit can also be composed of energy storage modules, such as batteries, flywheels and super capacitors. This system can turn many consumers of electricity into producers. Microgrids can be found in residential buildings, commercial buildings, industrial compounds and rural locations.

The IEEE standard 1547_4-2011 is a set of guidelines for the design, operation and integration of distributed resource island systems with electric power systems [48], and includes the following definitions:

Distributed resource island systems: sometimes referred to as *microgrids*, are used for the intentional islands in electric power systems (EPSs). DR island systems are EPSs that: (1) have DR and load; (2) have the ability to disconnect from and parallel with the area EPS; (3) include the local EPS and may include portions of the area EPS; and (4) are planned. DR island systems can be either local EPS islands or area EPS islands.

2.2 Topology

The various topologies described in the literature involve a main AC and/or DC bus. Radial and mesh topologies are the most frequently used architectures for the connection of DGs. The main configuration is the radial form, which resembles closely classical distribution systems. This configuration is shown in Fig. 2.1. A point of common coupling is connected to link the AC grid through a static transfer switch (STS) [24, 49]. In some systems with a multi-terminal interconnection, the microgrid adopts a ring-like topology.

Figure 2.2 and Fig. 2.3 show various radial topologies. Four types of standalone microgrids are shown along with the type of connectors and the energy sources. The efficiency, economical cost and fuel consumption of these systems was compared in [1]. Topology 1 shows a centralized AC coupled hybrid power system. The wind generator (WG) is coupled directly to the AC grid, whereas the photovoltaic system (PV) uses converters to link to the grid. The energy storage system uses the battery bank (BB) with a double configuration to couple it with the AC grid. Both the diesel generator (DiG) and the load are coupled directly. In topology 2, a DC bus is used to couple the energy sources (WG, PV) with the energy storage system. This DC bus is linked to the AC side through a pair of converters, and the load and the DiG are at the AC bus. Figure 2.3 shows

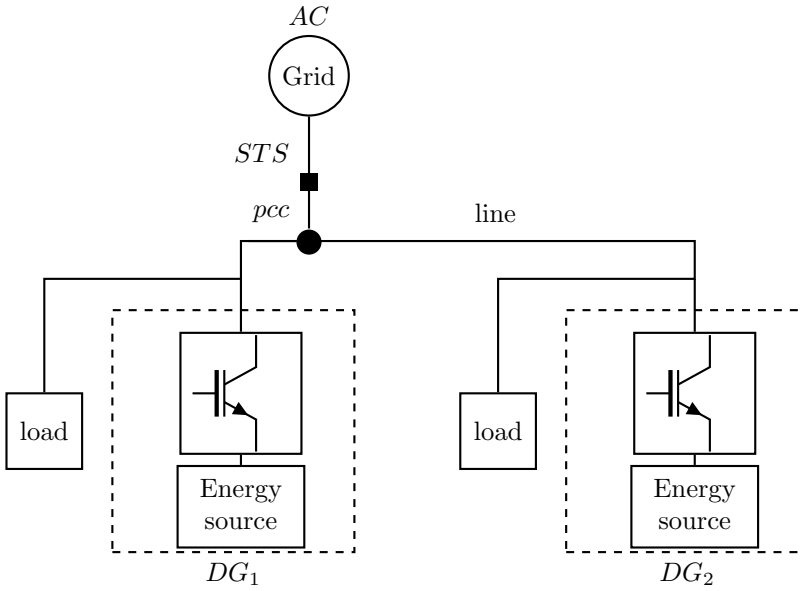

Figure 2.1: Radial topology.

two more radial topologies. In topology 3, the DC bus is centralized. In this configuration the AC source (DiG) uses a combination of converters to inject the power. The load is also connected to the DC bus by two converters. Topology 4 contains two buses. The energy sources are connected according to their primary current characteristics. The PV system and the BB are at the DC bus, whereas the DiG, WG and the load at the AC bus. However, the two buses can exchange power through a couple of converters (DC-DC and DC-AC). The surplus of power at the DC side is injected into the AC side by a power exchanger device. Therefore, the deficit of power at the DC bus is also compensated by the power exchanger device [25].

The efficiency of power consumption as a function of the directly consumed power of each power source was studied in [1] forthe different topologies and is presented in Fig. 2.4. For the PV system, comparison of the efficiency in the four topologies reveals that the efficiency of topology 2, 3 or 4 is higher than that of topology 1 for a directly consumed power below 85% (Fig. 2.4a) [1]. This conclusion can be obtained by calculating the area under the curves with a Riemann sum. The efficiency per unit area each topology, $A_{PV} = [A_{Topology1}, A_{Topology2}, A_{Topology3}, A_{Topology4}]$ is equal to $A_{PV} = [0.832, 0.873, 0.873, 0.873]$. Figure 2.4b shows the power consumption efficiencies of the different topologies for

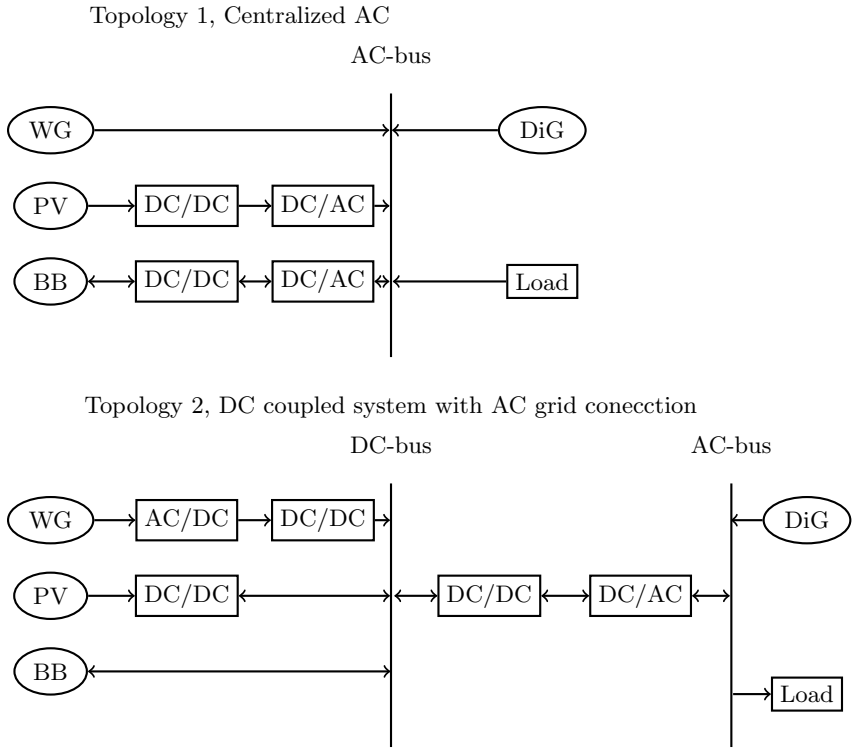

Figure 2.2: Radial topology: structures 1 and 2 [1].

the wind power generator. From Fig. 2.4b [1], it can be concluded that topology 4 is the most efficient. Again, if the area under the curve is used $A_{WG} = [A_{Topology1}, A_{Topology2}, A_{Topology3}, A_{Topology4}]$ is equal to $A_{WG} = [0.872, 0.840, 0.840, 0.893]$, confirming that topology 4 has the highest efficiency. Finally, Fig. 2.4c shows the efficiencies of the various topologies for for the DiG. Topologies 2 and 4 presents are the most efficient for this energy source. The area under the curve $A_{DiG} = [A_{Topology1}, A_{Topology2}, A_{Topology3}, A_{Topology4}]$ is equal to $A_{DiG} = [0.875, 0.896, 0.841, 0.896]$. Thus, topologies 2 and 4 show the best performance.

A losses analysis can be carried out based on the efficiency areas determined above to identify the best topology. Using the areas from the efficiency ($A_{efficiency}$), the area of losses (A_{losses}) can be calculated as in (2.1).

$$A_{losses} = 1 - A_{efficiency} \tag{2.1}$$

The losses comparison in Fig. 2.5 shows the area of losses for each topology as

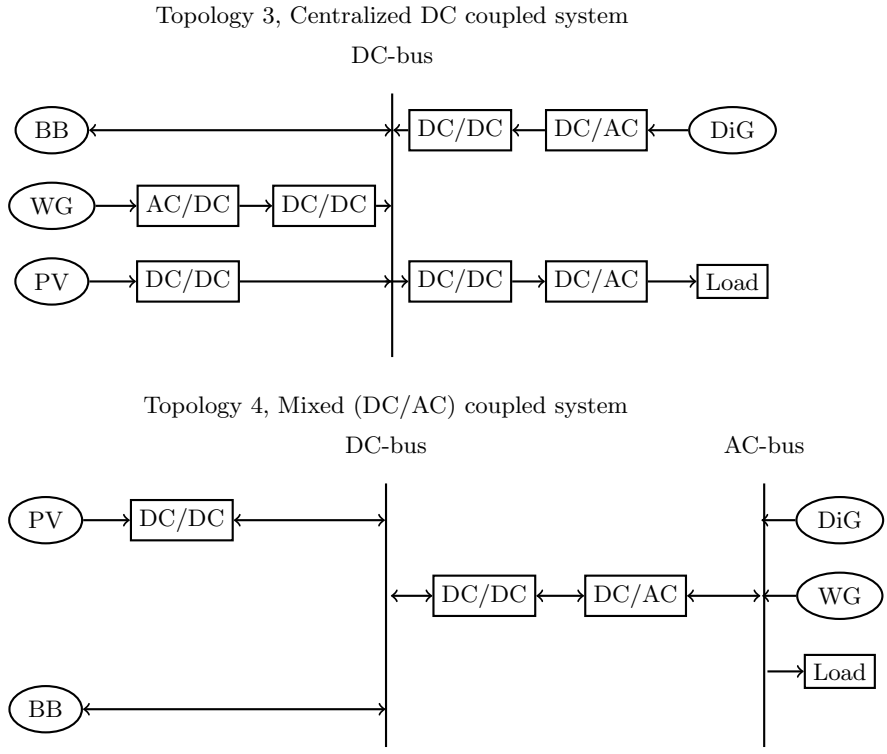

Figure 2.3: Radial topology: structures 3 and 4 [1].

a function of each energy source. The best performance was obtained with the topology 4, and variant of this topology is used as a test-bench in this research. Topology 4 clearly has the smallest area of losses for each energy source.

2.3 Advantages of distributed generation

In this section, a list of advantages for the use of DGs is presented [50, 51]. The use of DGs in microgrids has several potential benefits as follows:

- Ability to meet the increasing energy demand around the world, which can be achieved without modifying the capabilities of transmission systems.
- The use of fossil fuels may decline or can be kept constant with the integration of renewable energy.
- Losses are reduced avoiding large transmission lines for the transportation of the generated electrical energy.

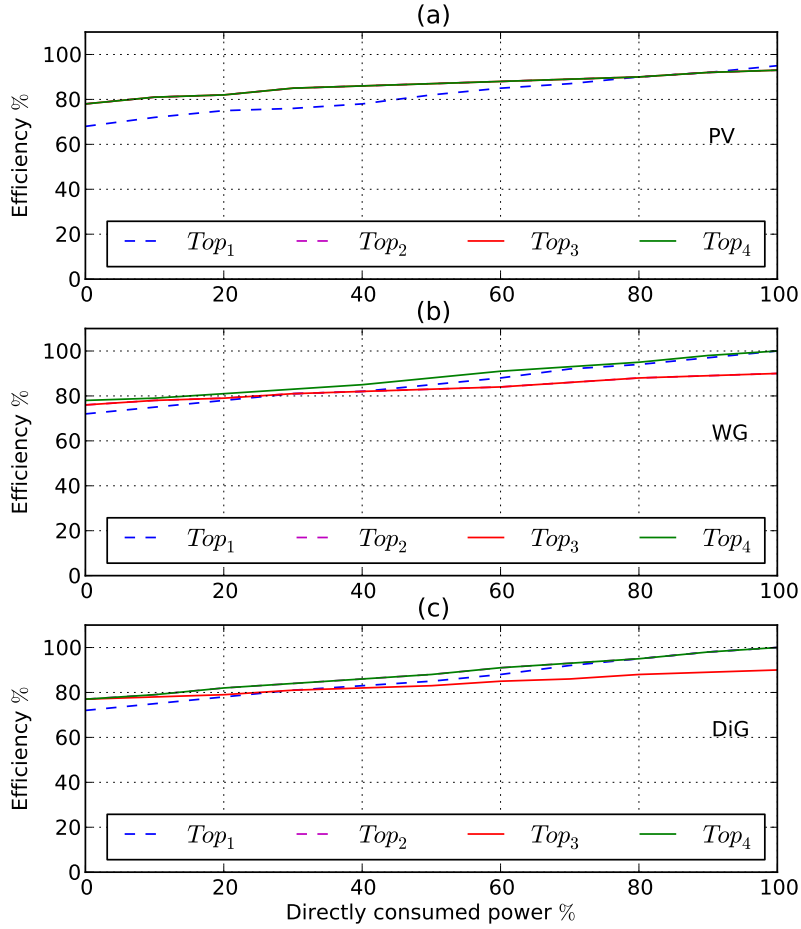

Figure 2.4: Comparison of power consumption by the different topologies (Top), from [1]. Directly consumed power for the PV source (a), directly consumed power for the WG source (b), and directly consumed power for the DiG source (c)

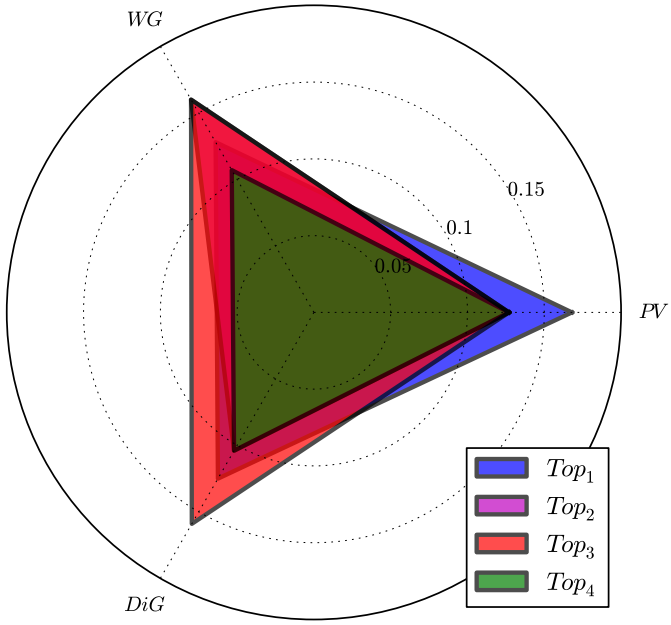

Figure 2.5: Comparison of the area of losses in the different topologies (Top) as a function of the energy source: PV, WG and DiG.

- Improvement in power quality with the use of controlled power electronics.
- Power can be supplied continuously with the integration of DGs in microgrids.
- Reactive power compensation can be improved at the distribution level. The compensation is local.
- Microgrids avoid blackouts and loss of productivity during the island mode.
- The transient can be completely controlled thanks to the use of power electronics in the DG.
- Flexible distribution networks can be made with microgrid clusters; therefore, faults can be quickly isolated and removed.

2.4 Stability of dynamic systems

A summary of the mathematical tools used in studies related to the stability of electrical power systems is shown in Fig. 2.6 [52]. Nyquist and Bode are the main criteria for stability analysis in the frequency domain, whereas non-linear analysis and linear analysis involving classical eigenvalues and Lyapunov tests are the main criteria in the time domain. Non-linear stability can be studied by the Lyapunov criteria as a computational tool (*i.e.* with Lyapunov exponent) or the Lyapunov function and bifurcation points can be identified by continuation methods.

Power system stability and driving force instability criteria have been classified according to their time scale: short-term and long-term [3] (Table 2.1). Stability problems may involve generator rotor angle stability. One problem is undamped electromechanical oscillations, and a second is monotonic rotor acceleration, which leads to loss of synchronism. The first type of instability involves small disturbances and is called steady state or small signal. The second type is initiated by large disturbances and is called transient or large-disturbance stability.

Rotor angle stability, based on electromechanical dynamics and transient dynamics as a measure of transient stability and generator transient reactance, is defined as short-term stability, within the range of few seconds.

As has been established for classical systems in [3], when the short-term dynamics are stable they eventually die out some time after a disturbance, and the system enters a slower time frame. Several dynamic components are related in this time frame, including transformer tap changers, generator limiters, boilers,

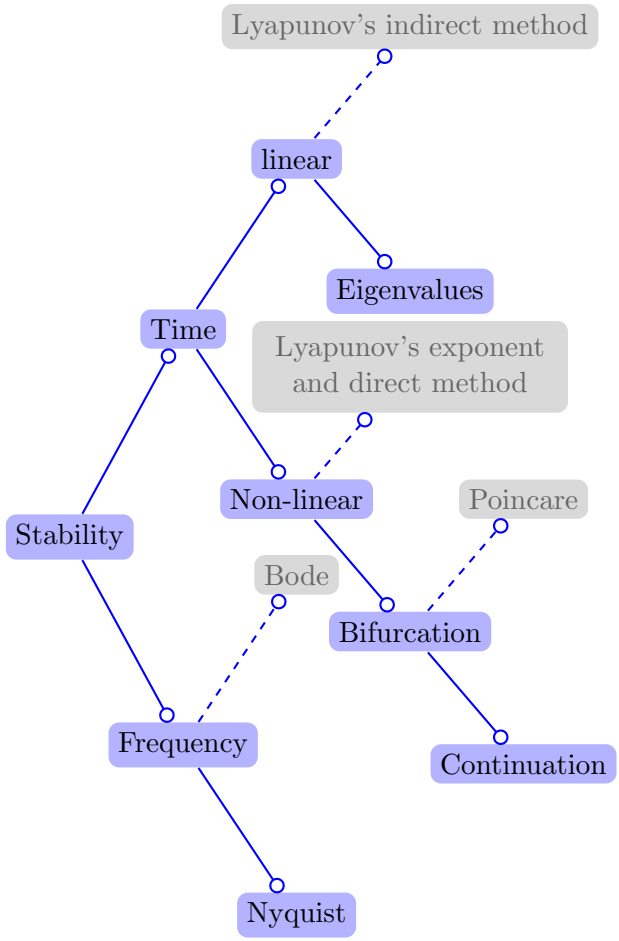

Figure 2.6: Path of the tools for stability studies in each of the domain.

etc. This time frame lasts for several minutes and is called the long-term time scale.

This classification also applies to microgrids (Fig. 2.7). The factors involved differ from those of the classical power system, due to the lack of inertia from generators (*e.g.* rotating electrical machines). In systems with many power electronics devices, short-term stability involves the interaction of the inner controllers and the passive elements used to store energy during switching operations [27]. At the distribution level, the lines show resistive behavior. Therefore, the states in the lines respond quickly to changes in the operation point. These changes can be associated with small changes in the power consumed by the loads.

Table 2.1: Classical power system stability classification [3].

Time scale	Generator-driven		Load-driven
short-term	rotor angle stability		short-term
	steady-state	transient	voltage stability
long-term	frequency stability		long-term voltage stability

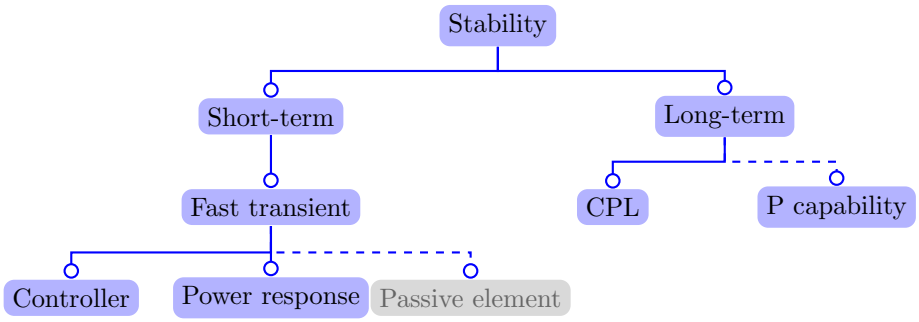

Figure 2.7: Classification of the stability of microgrids.

Systems with power electronics acting as a load are correlated with constant power load characteristics. The analysis of power electronic devices has shown that the controllers of the current or voltage are faster than the outer loop controllers used to regulate power [53]. The long-term signal problem in power electronics based systems is related for this time frame. Several groups of researchers have focused on a particular stability problem, the negative impedance behavior of the constant power load (CPL), which can be a characteristic of power electronic devices [14, 45]. The small signal stability test has been applied to automotive systems with the CPL mentioned above.

The droop controller and the power capability of the converters in the microgrid[1] can take part of the long-term study. The droop controller of power electronic devices is slower than the inner controllers, which regulate the currents and voltages of the storage elements (*i.e.* inductors and capacitors). Hence, when the short term dynamics are stable and have been rejected, the system starts to operate in the slower stage [54, 55]. One of the assumptions of the droop controller is that the current and the voltage are in steady state [54]; however, this

[1]This statement has been shown in networks with just power electronic converters as sources.

Table 2.2: Bandwidth for the controllers of a VSC operating in a microgrid [2].

Level	Type	BW	Response
0	current	20 kHz	short-term
0	voltage	5 kHz	short-term
1	droop	30 Hz	long-term
2	secondary	3 Hz	long-term

assumption is not necessarily true bacause interference or interaction between short and long term dynamics may exist. In [54, 55], the stability problem was reduced to a linear analysis with eigenvalues of the gains in the droop controllers. The authors in [2] present a hierarchical strategy to control the microgrid based on power electronic devices. The bandwidth of each control loop is described in Table 2.2. According to this hierarchical control strategy, the slow behavior of the droop and secondary controllers affect the long-term stability of microgrids. Finally, the power capability of the converter defines the power limitations in the design of the converter.

Table 2.2 shows the bandwidths (BW) of the multiple control loops applied to a voltage source converter (VSC) for a hierarchical control strategy in microgrids [2]. Figure 2.8 presents this strategy; i and v are the current and voltage measured from the converter, respectively. Hi and Hv are the controllers for current and voltage, respectively. P is the active power and Q is the reactive power. The references of frequency and voltage are ω_{ref} and V_{ref}, respectively. The controller called level 0 has been applied to the current of the inductor and voltage of the capacitor of an LCL filter. The level 1 controller is a droop controller (*e.g.* active power-frequency and reactive power-voltage in inductive networks) and the level 2 controller is the secondary or restoration controller. This part compensates the voltage and frequency deviations generated by the droop controller effect,and thus increases or reduces the active and reactive power injected into the system for every change of load or generation inside the microgrid. The microgrid voltage and frequency are sensed and compared with the references ω_{ref} and V_{ref}. The errors obtained are sent to the droop controllers to restore the voltage and frequency of the system. The behavior of the droop controller is slower than that of the current controller, with a rate of 0.15%.

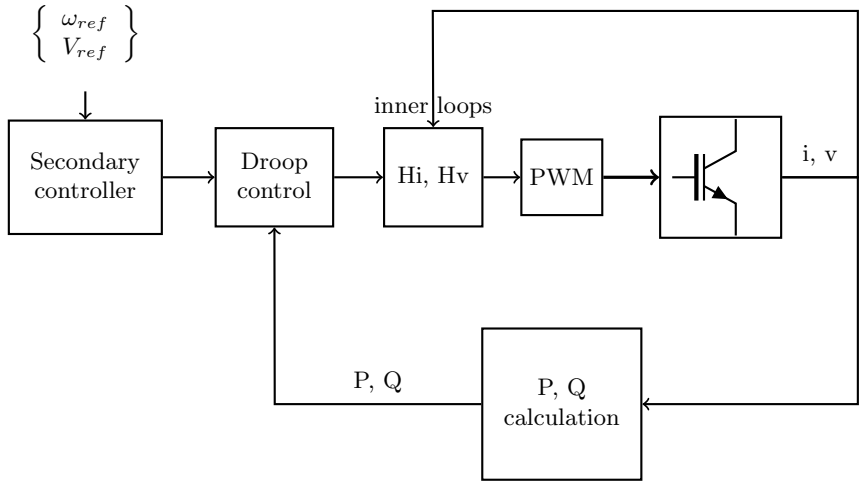

Figure 2.8: Primary and secondary control based on hierarchical management strategy [2].

Chapter 3

Microgrids in distribution systems

This chapter describes the topology of the microgrid used as a test-bench in this research. The concept of droop and secondary control are described. Finally, this chapter describes the design of the PI controller and the converters used in the mixed DC-AC microgrid.

3.1 Microgrid containing DC and AC buses coupled through a power exchanger device

3.1.1 Topology

The complete hybrid current DC-AC microgrid is presented in Fig. 3.1. The nodes from $i \in \{1, ..., 5\}$ form the direct current side, whereas the nodes from $i \in \{6, ..., 8\}$ are part of the alternative current system. The power can be exchanged between the DC and AC side through a converter called the power exchanger device, P_{ex}. Components of the grid assumed can communicate with an energy management system to coordinate operations. In this way the multiple converters can inject, consume or exchange power.

The topology described in Fig. 3.1 is based on a segment of the CIGRE benchmark low voltage micro-grid [7], with some modifications: the microgrid operates with direct current and includes a point of power exchange with an AC microgrid that has distributed generators. The voltage at the DC and AC sides is 400 V and 200 V, respectively. The line parameters are calculated for a service connection feeder with 16 mm^2 Cu, and the main line with 120 mm^2 Al XLPE. They are also described in Appendix A Table A.1. R_{li} is the resistive load at the DC bus at node

i, and S_l represents the AC load at the node i. The loads at the DC bus are up to R_{l4}, and the AC loads start at S_{l6}. The line between the nodes is $Line_{(i-1)-i}$, and its resistance and inductance values are r and L, respectively. The distance between each node is 30 m. The DC system is composed of a wind turbine (WT) with 5kW of power (DG_1), with a permanent magnet generator and a diode bridge rectifier, followed by the DC-DC converter. The second renewable source (DG_2) is a photo-voltaic (PV) 5kW system. It can operate at maximum power extraction and is connected to a DC-DC converter to regulate the voltage supplied to the grid. The third distributed resource is a battery bank (ES_1), which is involved in power sharing. It is coupled to the grid by a DC-DC bidirectional converter. The power can be exported or imported by a voltage source converter (P_{ex}) connected to the AC system. Power sharing within the DC grid can be coordinated by droop control P-V. Finally, the AC grid is composed of an energy storage device (ES_2) and a DG unit (DG_3) with a rated power of 12 kVA. Therefore, the loads are configured to enable the system operate to in island mode. Classical droop control can be applied to the AC side, with P-ω and $Q - V$ droops.

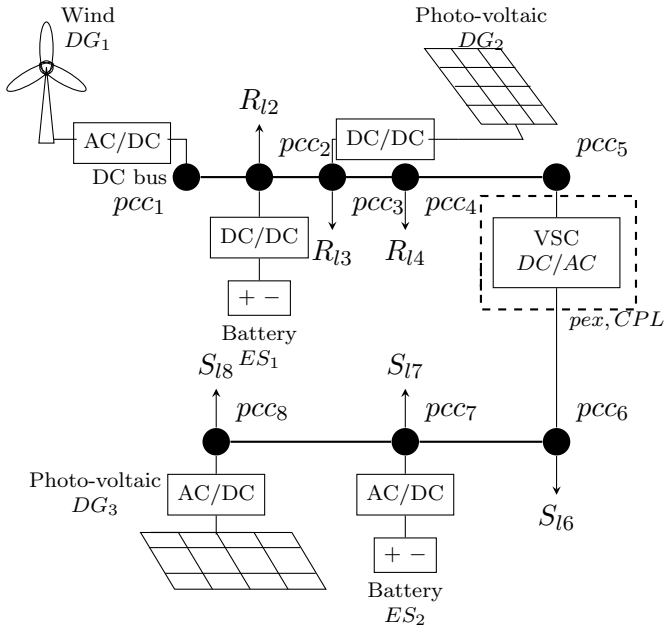

Figure 3.1: Structure of the DC-AC micro-grid.

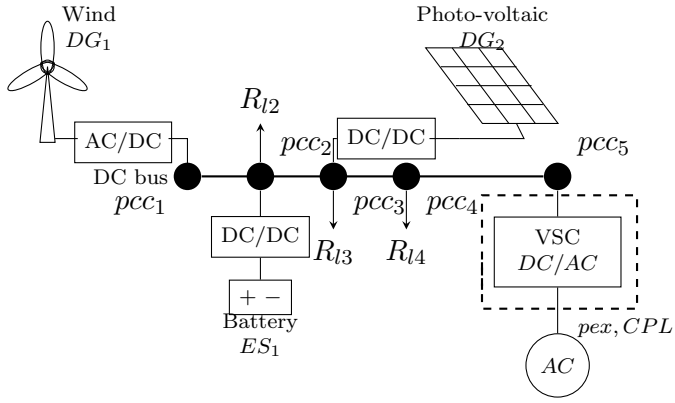

Figure 3.2: Topology of the DC microgrid

3.2 DC bus microgrid

The topology described in Fig. 3.2 is based on the DC section of the full model (shown in Fig. 3.1). The parameters are described in Appendix A Table A.1. R_{li} represents the load in the node pcc_i with $i \in \{1, ..., 5\}$ (the line is the described in the previous section). The system is composed of the distributed generator DG_1. The second power supply, DG_2, uses a DC-DC converter to regulate the power supplied to the microgrid. The third distributed resource is based on an energy storage system (ES_1) which is involved in power sharing, and is coupled to the grid by a DC-DC bidirectional converter. The power can be exported or imported by a voltage source converter (P_{ex}) connected to an AC system. The rated power is 12 kW. The resistive and inductive characteristics of the line were obtained by the lines used in [7].

The DC microgrid used in this thesis has the following coordination: DG_1 controls the voltage of the DC bus, DG_2 and ES_1 inject constant current into the network and the Pex consumes power from the DC microgrid.
The power balance of the DC microgrid is:

$$P_{Pex} + P_{R_{l2}} + P_{R_{l3}} + P_{R_{l4}} = P_{DG_1} + P_{DG_2} + P_{ES_1}$$

The dynamic equivalents of the distributed generators and exchanger device required to develop the network equivalent and to obtain the differential equations are described in the next subsection.

3.2.1 Dynamic equations of the LV DC microgrid network

The distributed generators and the Pex device are represented as a dynamic equivalent in Fig. 3.3. DG_1 is described as an ideal voltage source (v_{dg1}), based on the voltage control strategy used. DG_2 and ES_1 have an ideal current source equivalent to describe their dynamics in the network (I_{dg2} and I_{es1}, respectively). The power exchanger Pex is presented as a current type load, with current i_{pex}.

A general form of currents and voltages is used within each element to develop the state space representation of this network. The set of differential equations of the grid shown in Fig. 3.4 are annotated according to the branch and link numbers defined by the adopted topology. Therefore, each element has the variables i_{gk} and v_{gk} (which are the grid current and voltage, respectively) and $k \in \{1, ..., 16\}$[1]. Table 3.1 shows how the microgrid network of Fig. 3.3 relates to the links and branches of the tree presented in Fig. 3.4 and lists the variables of each element. The line resistances are r_{e1}, r_l, r_{l2} and r_{l3}. The line inductances are L_{e1}, L_l, L_{l2} and $L_{l3} = 3L_l + L_{fvsc}$. Finally, the capacitance for the P_{ex} device connection is C_{pex}.

The dynamics of the network are described by (3.1) to (3.5). These equations were obtained by the application of proper tree topology [56][2]. It is necessary to use the class of complete networks, in which the current in the inductors and the voltage in the capacitors can be used as the state variables of the system [57]. The state variables for the network are $x = [i_{g3}, i_{g7}, i_{g11}, i_{g14}, v_{g15}]^T$. Therefore, the remaining variables i_{gk} and v_{gk} can be defined as functions of the states x. Hence, the sources of the system at this stage of the analysis are $v_{g1} = V_{dg1}$, $i_{g5} = I_{es1}$, $i_{g9} = I_{dg2}$ and $i_{g16} = i_{pex}$.

The first differential equation of the system is obtained by applying Kirchhoff's voltage law to the loop formed with the nodes $pcc_1 - 0 - pcc_2 - pcc_1$.

$$\frac{d}{dt} i_{g3} = \frac{R_{l2}(i_{g7} - i_{g5}) - (R_{l2} + r_{e1}) i_{g3} + v_{g1}}{L_{e1}} \tag{3.1}$$

The second differential equation of the network is obtained by applying Kirchhoff's voltage law to the loop formed with the nodes $pcc_2 - 0 - pcc_3 - pcc_2$.

[1] For the sake of simplicity the argument t has been removed in the time functions.

[2] A proper tree of a network is defined as one whose branches contain every capacitive element of the network or every capacitive element plus resistive elements

Fig. 3.3	Fig. 3.4	
Element	Element (type)	Variables
v_{dg1}	1 (branch)	v_{g1}, i_{g1}
r_{e1}	2 (branch)	v_{g2}, i_{g2}
L_{e1}	3 (link)	v_{g3}, i_{g3}
R_{l2}	4 (branch)	v_{g4}, i_{g4}
I_{es1}	5 (link)	v_{g5}, i_{g5}
r_l	6 (branch)	v_{g6}, i_{g6}
L_l	7 (link)	v_{g7}, i_{g7}
R_{l3}	8 (branch)	v_{g8}, i_{g8}
I_{dg2}	9 (branch)	v_{g9}, i_{g9}
r_{l2}	10 (branch)	v_{g10}, i_{g10}
L_{l2}	11 (link)	v_{g11}, i_{g11}
R_{l4}	12 (branch)	v_{g12}, i_{g12}
r_{l3}	13 (branch)	v_{g13}, i_{g13}
L_{l3}	14 (link)	v_{g14}, i_{g14}
C_{pex}	15 (branch)	v_{g15}, i_{g15}
Pex	16 (link)	v_{g16}, i_{g16}

Table 3.1: Relationship between the dynamic equivalent elements and variables used in the grid.

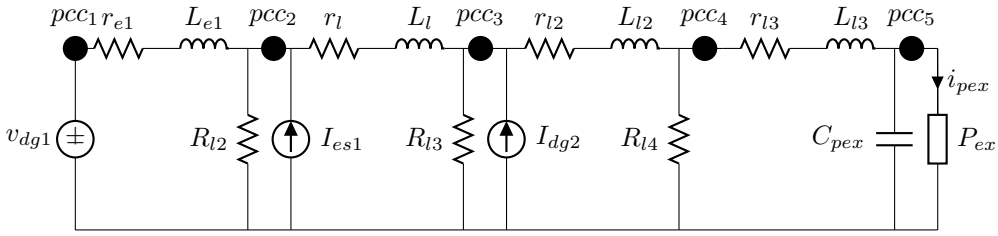

Figure 3.3: Dynamic equivalents of the devices in the grid.

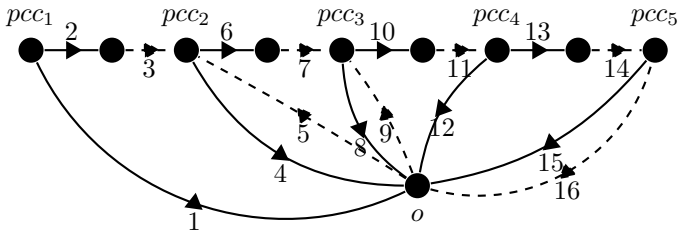

Figure 3.4: Tree schematic of the dynamic equivalents, showing the branches (solid) and links (dashed).

$$\frac{d}{dt}i_{g7} = \frac{R_{l3}(i_{g11} - i_{g9}) - (R_{l3} + r_l + R_{l2})i_{g7} + R_{l2}(i_{g3} + i_{g5})}{L_l} \tag{3.2}$$

The third differential equation of the network is obtained by applying Kirchhoff's voltage law to the loop formed with the nodes $pcc_3 - 0 - pcc_4 - pcc_3$.

$$\frac{d}{dt}i_{g11} = \frac{R_{l4}i_{g14} - (r_{l2} + R_{l4} + R_{l3})i_{g11} + R_{l3}(i_{g7} + i_{g9})}{L_{l2}} \tag{3.3}$$

The fourth differential equation of the network is obtained by applying Kirchhoff's voltage law to the loop formed with the nodes $pcc_4 - 0 - pcc_5 - pcc_4$.

$$\frac{d}{dt}i_{g14} = \frac{R_{l4}i_{g11} - v_{g15} - (r_{l3} + R_{l4})i_{g14}}{L_{l3}} \tag{3.4}$$

The final differential equation of the network is obtained by applying Kirchhoff's current law to the node pcc_5.

$$\frac{d}{dt}v_{g15} = \frac{i_{g14} - i_{g16}}{C_{pex}} \tag{3.5}$$

3.3 AC bus microgrid

The AC microgrid is shown in Fig. 3.5. The nodes from $i \in \{6, ..., 8\}$ are part of the AC system. The power can be exchanged between the DC and AC side through the power exchanger device P_{ex}. Components of the grid assumed can communicate to coordinate the operation of the multiple converters used to inject, consume or exchange power. The topology of this system is shown in Fig. 3.5. The parameters are described in appendix A Table A.1. S_{li} represents the load in the node i and the AC loads are range S_{l6} to S_{l8}. The DC system is connected to the AC system by a voltage source converter (P_{ex}) (*i.e. the power exchanger device or constant power load at the DC bus*). The remaining AC microgrid is composed of an energy storage device (ES_2) and a DG unit (DG_3). Hence, the loads are configured such that the system operates in island mode.

The coordination algorithms for power sharing are beyond the scope of this research. Therefore, one coordination was chosen for the stability tests for the sake of simplicity. The P_{ex} injects constant power into the AC microgrid under the coordination chosen for the AC side of the microgrid. The P_{ex} is controlled with a current loop. DG_3 and ES_2 control the voltage of the AC microgrid with the help of a droop controller and secondary controller in each device. Droop control and secondary control are described in the next section.

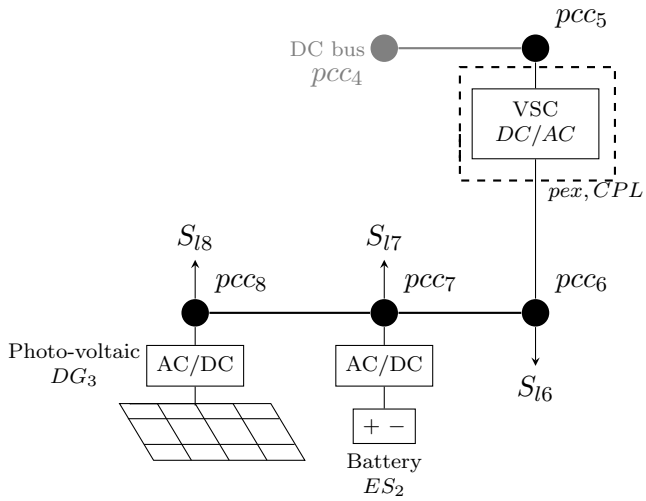

Figure 3.5: Structure of the AC micro-grid.

3.4 Droop control for power electronics systems

3.4.1 AC droop

The active and reactive power of the grid are controlled by the voltage source inverters (VSI) operating in island mode. Their aim is to regulate voltage and frequency around their nominal values [58]. An inner controller may be to regulate the currents. This controller is developed in the synchronous reference frame, and the second loop controls the voltage in each axis. In addition, a PLL estimates the electrical angle over the quadrature axis.

In this case, voltage and frequency control at the distribution level depend on the transmission control scheme. Classical droop control is applied and LCL filters are used in the VSI. In classical transmission droop control, the frequency is controlled by the active power. This strategy has been applied here, even when the impedance angle of a distribution line is small due to the low X/R line ratio. Classical $\omega - P$ droop control can be performed with the LCL filters at the inverter terminals; the inductor connected to the grid provides the inductive characteristic of the network and the reactive power controls the voltage at the grid connection point [2, 59, 60]. The control strategy for a voltage source inverter operating in island mode is described by (3.6), and (3.7) and shown in Fig. 3.4.1.

$$\omega = \omega_{ref} - \rho_P(P - P_{ref}) \tag{3.6}$$

$$V = V_{ref} - \rho_\omega(Q - Q_{ref}) \tag{3.7}$$

where, ω_{ref} and V_{ref} are the angular electrical frequency and the voltage mag-

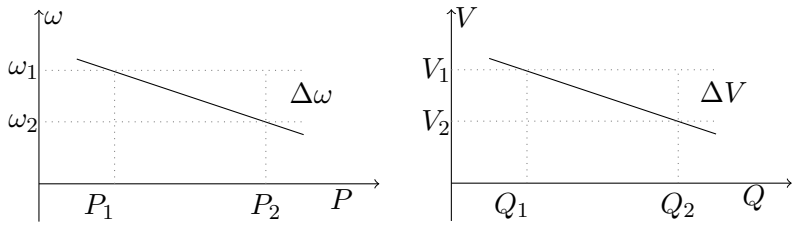

Figure 3.6: AC droop characteristics for $\omega - P$ and $V - Q$.

nitude of the grid, respectively. The nominal power values are P_{ref} for the active, and Q_{ref} for the reactive power. The controller parameters provide the slopes of

the relations $\Delta\omega/\Delta P$ and $\Delta V/\Delta Q$ [2, 61]. The selection of these values are:

$$\rho_\omega = \frac{\Delta\omega}{P_{max}} \tag{3.8}$$

$$\rho_V = \frac{\Delta V}{Q_{max}} \tag{3.9}$$

where $\Delta\omega$ and ΔV are the maximum differences in voltage and angular frequency allowed in the system and P_{max} and Q_{max} are the maximum active and reactive power supplied by the converter respectively. The output power of each VSI can be adjusted by changing the P_{ref} but maintaining the defined droop parameter; this is necessary when the load set point is known.

However, droop control only shares the power load of the system between the converters; when more power is supplied by each device, the voltages and frequency of the system are reduced. Hence, the system has a hierarchical architecture to keep the voltage and frequency at their nominal values. The use of a secondary controller ensures that the drooped voltage and frequency return to the nominal operation point [60]. This is recommended for isolated power systems and is known as automatic generation control (AGC) with integral action. In this work, secondary control is based on that reported in [2], but will be applied here to a decentralized system. The controller is described as:

$$\delta\omega = k_{p,\omega}(\omega_{ref} - \omega) + k_{i,\omega}\int(\omega_{ref} - \omega)dt \tag{3.10}$$

$$\delta E = k_{p,E}(E_{ref} - E) + k_{i,E}\int(E_{ref} - E)dt \tag{3.11}$$

where the gains of the secondary controllers are $k_{p,\omega}$, $k_{i,\omega}$, $k_{p,E}$, and $k_{i,E}$, The variable E is equal to the peak value of the AC voltage and E_{ref} is the reference voltage at the terminals of the VSI. Figure 3.7 shows a single phase representation of the configuration of this system. C_{dc} is the capacitor used in the DC side, L_{ac} is the filter inductance used in the VSI, C_{ac} is the capacitance at the AC filter (which helps to control the AC voltage), i_{dg} is the output current, and v_{dg} is the voltage at the capacitance. The LCL filter is formed by an inductance equal to the L_{ac} placed after the AC capacitor.

3.4.2 DC droop

The DC power control can be obtained from the analysis of a droop controller in an AC system with a low X/R relation. Furthermore, in systems where the reactance

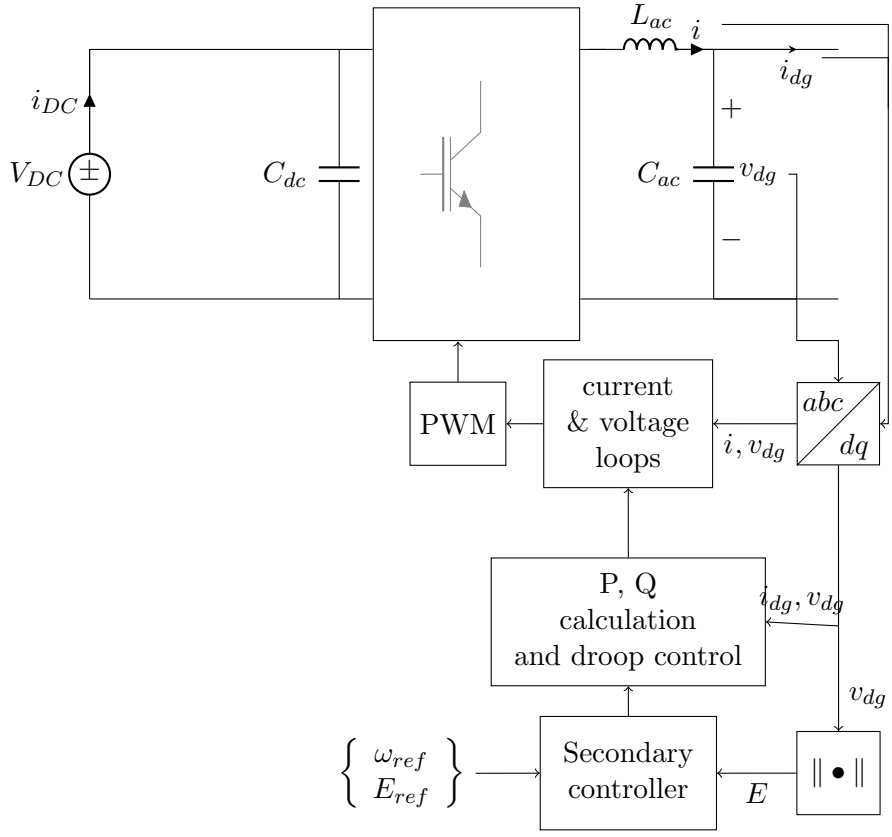

Figure 3.7: DG used to control the AC grid voltage and frequency.

has been neglected, the power can be controlled by a characteristic $V - P$ [62]. Hence, changes in active power are obtained by changing the voltage (instead the $\Delta\omega$, as was the case in the previous section). Therefore, the characteristic gain can be called ρ_{vp} and the selection is:

$$\rho_{vp} = \frac{\Delta V}{P_{max}} \tag{3.12}$$

3.5 Power electronics converters used in the microgrid

3.5.1 Control strategy in DC and AC converters

Converters keep the voltage constant in the DC micro-grid according to the strategy described in [19]. This strategy is based on hierarchical control with multiple loops. Figure 3.8 shows a primary controller with an inner loop that

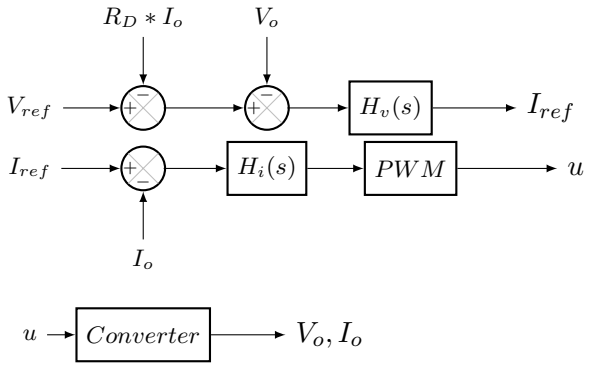

Figure 3.8: Primary control method for the DC converters.

controls the current injected into the system. An outer loop controls the voltage at the terminals of the converter. Hence, operation in island mode is ensured and communication between the sources can be avoided. The grid can operate under constant voltage at the point of common coupling with a primary power-voltage droop controller, which enables power sharing at the DC side and classical droop at the AC side [19]. The maximum voltage variation is defined as $\Delta V = \pm 4\%$. This method is based on measurements of the voltage and current in the terminals of the converter. In Fig. 3.8, $V_{ref} and\ I_{ref}$ are the reference voltage and current, respectively[3]. R_D is a virtual output impedance, $H_v(s)$, $H_i(s)$ are the voltage and current controllers, respectively. V_o and I_o are the voltage and current of the converter, respectively.

3.5.2 PI controller model

The typical controller used in industry for the class of converters listed in this research is the PI controller. Hence, due to its frequent use industry, the role that it plays in microgrid stability is discussed in this section [53]. The dynamic model for the PI adds one state variable to the system, introducing feedback and regulating output. The standard model used in the control of power electronics is shown in Fig. 3.9.

$$\dot{\gamma}_l = y_{ref} - y \tag{3.13}$$

$$u = K_p(y_{ref} - y) + K_i\gamma_l - d \tag{3.14}$$

where y_{ref} is the reference value, y is the output of the system, u is the controller

[3]For the sake of simplicity the argument s has been omitted.

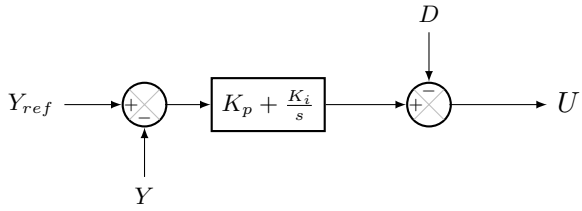

Figure 3.9: Block diagram in the Laplace domain for standard control in power electronics.

output, d is a decoupling term, and K_p and K_i are the proportional and integral gains, respectively. The additional PI controller state is γ_l, where the suffix l represents the different PI loops.

For the block representation, (3.13) and (3.14) can be represented in the Laplace domain as:

$$U = (K_p + \frac{K_i}{s})(Y_{ref} - Y) - D \tag{3.15}$$

The system can be represented in a general form as:

$$H(s) = \frac{b}{s} \tag{3.16}$$

b is a parameter of the plant [53]. The proportional plus integral controller is $G_c(s) = K_p + K_i/s$ [63]. The closed loop characteristic polynomial equation is:

$$A(s) = s^2 + K_p b s + b K_i \tag{3.17}$$

The standard second order equation is $s^2 + 2\rho\omega_o s + \omega_o^2$, where ω_o determines the response speed and ρ is the damping ratio (*e.g. determines the shape of the response*). Equating this with (3.17) the controller can be designed as:

$$K_p = \frac{2\rho\omega_o}{b} \tag{3.18}$$

$$K_i = \frac{\omega_o^2}{b} \tag{3.19}$$

If the controller is:

$$G_c(s) = K_p + \frac{K_p}{T_i s}, \tag{3.20}$$

The PI can be designed as:

$$K_p = \frac{2\rho\omega_o}{b} \tag{3.21}$$

$$T_i = \frac{2\rho}{\omega_o} \tag{3.22}$$

The chosen damping coefficient is $\rho = 0.7$, a value that yields a good step response and a damped oscillation [63].

3.5.3 Voltage Source Converter

The voltage source converter presented in Fig. 3.10 is connected at the DC side to a grid equivalent and to an ideal AC system. The dynamic equations are described in (3.23)-(3.27).

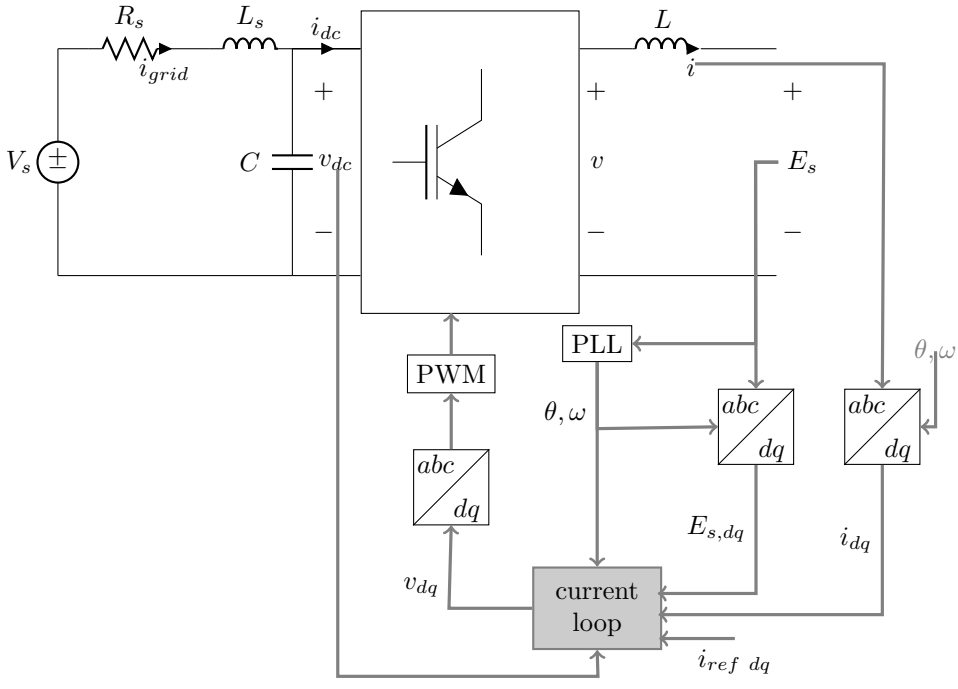

Figure 3.10: Source and single phase equivalent converter system.

$$\frac{di_d}{dt} = \frac{v_d - E_{sd} + \omega L i_q - r i_d}{L} \tag{3.23}$$

$$\frac{di_q}{dt} = \frac{v_q - E_{sq} - \omega L i_d - r i_q}{L} \tag{3.24}$$

$$\frac{dv_{dc}}{dt} = \frac{i_{grid} - i_{dc}}{C} \tag{3.25}$$

$$i_{dc} = \frac{3}{2}(s_{gd} i_d + s_{gq} i_q) \tag{3.26}$$

$$s_{gk} = \frac{v_k}{v_{dc}} \tag{3.27}$$

where $E_{s,k}$ with $k \in \{d, q\}$ is the voltage of the AC grid in the direct or quadrature axes. The current in the filter inductance L is i_k. The voltage at the switch terminals of the converter is v_k. The DC voltage is v_{dc}, the current at the DC side of the converter is i_{dc}, the duty commands are s_{gk}, the electrical frequency is ω, and the current flowing from the DC grid is i_{grid}. The controller as presented in [53] for this system is described with the set of equations in (3.28)-(3.31).

$$v_d = k_p \left(i_{refd} - i_d\right) + k_i \gamma_d - \omega L i_q + (\alpha e^{-\alpha t}) E_{sd} \tag{3.28}$$

$$v_q = k_p \left(i_{refq} - i_q\right) + k_i \gamma_q + \omega L i_d + (\alpha e^{-\alpha t}) E_{sq} \tag{3.29}$$

$$\dot{\gamma_d} = i_{refd} - i_d \tag{3.30}$$

$$\dot{\gamma_q} = i_{refq} - i_q \tag{3.31}$$

where γ_k describe the states of the PI controller, α is the parameter of the first-order low-pass feedforward filter $H_f(s) = \alpha/(s + \alpha)$; this filter smooths the measured voltage $E_{s,k}$. The proportional and integral gains of the PI controller are k_p and k_i, respectively, and the reference currents for the direct and quadrature axes are $i_{ref\ k}$.

A design of the controller that gives correct behavior of the system under closed loop operation is shown for the proportional gain k_p and the integral gain k_i.

$$k_p = 2\rho\omega_o L \tag{3.32}$$

$$k_i = \omega_o^2 L \tag{3.33}$$

$$\omega_o = 2\pi \frac{f_{sw}}{n_i} \tag{3.34}$$

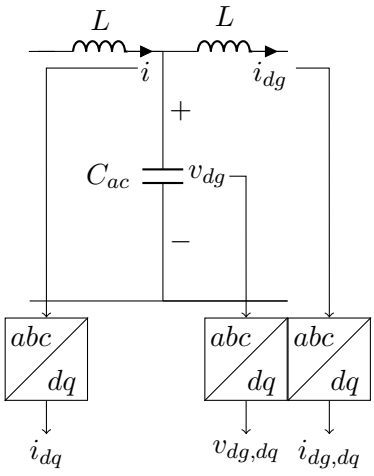

Figure 3.11: LCL filter used to control the voltage and frequency of the AC side of the microgrid.

The natural frequency ω_o requires a large value for the fast response of the controller. However, this value can not interfere with the switching action. Hence, the value is an order $(1/n_i)$ lower than the switching frequency f_{sw}.

Control of the voltage at the LCL filter of the DG

The second loop controled by a VSC is the voltage at the capacitor of the LCL filter of the DG unit. Here, it is assumed that the current i at the inductance is fast enough and provides input to the system (Fig. 3.11). The set of equations for AC voltage in the synchronous reference frame is:

$$C_{ac}\frac{d}{dt}v_{dg,d} = i_d - i_{dg,d} + \omega C_{ac} v_{dg,q} \tag{3.35}$$

$$C_{ac}\frac{d}{dt}v_{dg,q} = i_q - i_{dg,q} - \omega C_{ac} v_{dg,d} \tag{3.36}$$

where C_{ac} is the filter capacitor, ω is the electrical frequency, i_k with $k \in \{d, q\}$ is the input current or current injected from the internal inductor of the LCL filter. The current of the inductor connected to common nodes of the grid is $i_{dg,k}$, and the capacitor voltage is $v_{dg,k}$. The controller for the voltage at the capacitor is

defined as follows:

$$i_d = k_{p,v}(v_{refdg,d} - v_{dg,d}) + k_{i,v}\gamma_{v,d} + i_{dg,d} - \omega C_{ac} v_{dg,q} \tag{3.37}$$

$$i_q = k_{p,v}(v_{refdg,q} - v_{dg,q}) + k_{i,v}\gamma_{v,q} + i_{dg,q} + \omega C_{ac} v_{dg,d} \tag{3.38}$$

$$\dot{\gamma}_{v,d} = (v_{refdg,d} - v_{dg,d}) \tag{3.39}$$

$$\dot{\gamma}_{v,q} = (v_{refdg,q} - v_{dg,q}) \tag{3.40}$$

$$\tag{3.41}$$

where $\gamma_{v,k}$ with $k \in \{d, q\}$ is the PI controller state, $v_{refdg,k}$ is the reference voltage for each axis, $k_{p,v}$ is the proportional gain for the voltage controller and $k_{i,v}$ is the integral gain for the voltage controller. The natural frequency of the voltage loop $\omega_{o,v}$ is smaller than the natural frequency of the current loop described before. Therefore, the bandwidth of the voltage controller is smaller. The order for $\omega_{o,v}$ is defined by the gain $1/n_v$, where n_v is an integer and the selection uses maximum phase margin design [64] (e.g. the phase margin is typically chosen in the range of 30^o and 75^o). The natural frequency of the voltage loop $\omega_{o,v}$ is defined as in (3.42), to enable the application of hierarchical control. A design of the controller that includes $k_{p,v}$ and $k_{i,v}$ and gives correct behavior of the system under closed loop operation is:

$$\omega_{o,v} = \frac{\omega_o}{n_v} \tag{3.42}$$

$$k_{p,v} = 2\rho\omega_{o,v} C_{ac} \tag{3.43}$$

$$k_{i,v} = \omega_{o,v}^2 C_{ac} \tag{3.44}$$

Phase locked loop circuit

The converter system described above uses the synchronous reference frame; therefore, a phase locked loop (PLL) is required to obtain the variables as constant signals. The PLL system in Fig. 3.12 has been applied to the a-b-c signals [53, 65]. The dynamic model is described in (3.45).

$$\frac{d\theta}{dt} = \omega_{ref} + \Delta\omega = \omega_{ref} + (K_P(x_q - x_{qref}) + K_I \int (x_q - x_{qref})dt) \tag{3.45}$$

where, θ is the transformation angle, $x_k \forall k \in \{a, b, c\}$ is the measured variable for the PLL. x_{qref} is the reference synchronous variable and w_{ref} is the reference frequency speed. K_p and K_I are the proportional and the integral gains of the PI controller, respectively.

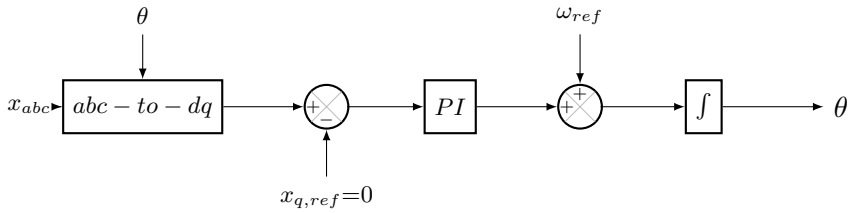

Figure 3.12: Block diagram of synchronous reference frame PLL.

3.5.4 DC bidirectional and boost converter

The characteristics of the bidirectional DC-DC converter enable the connection of an energy storage system. The unidirectional characteristics of the boost converter are used to connect renewable energy sources such as photovoltaic and wind energy conversion systems.

A vital component of microgrids operating in island or non-island mode is the energy storage device. This system , which is composed of a DC-DC bidirectional converter and a battery bank, is important because it can supply the necessary energy when the sources do not match the load demand. In this research, a bidirectional converter and an ideal DC source are used to emulate a full energy storage system. The dynamics of the bidirectional DC-DC converter in Fig. 3.13a are described by:

$$\frac{di_b}{dt} = -\frac{r_b}{L_b} i_b - \frac{v_{ob}}{L_b} + \frac{s_b v_{ib}}{L_b} \tag{3.46}$$

$$\frac{dv_{ib}}{dt} = \frac{i_s - s_b i_b}{C_b} \tag{3.47}$$

The parameters of the bidirectional converter are the inductance L_b, the resistance of the inductance r_b, the capacitance C_b, and the switching signal s_b. The state variables are the inductance current i_b and the capacitance voltage v_{ib}. Finally, the battery voltage is v_{ob} and the grid current is i_s.

In the case of the boost converter, the overall dynamics can also be represented by (3.46) and (3.47), and the battery voltage is the source voltage. The only assumption is that bidirectional current flow is not allowed ($i_b > 0 \ \forall t$). The dynamics of the boost in Fig. 3.13b are described by (3.48) and (3.49). The variable change $s_b = (1 - \varsigma_b)$ is allowed.

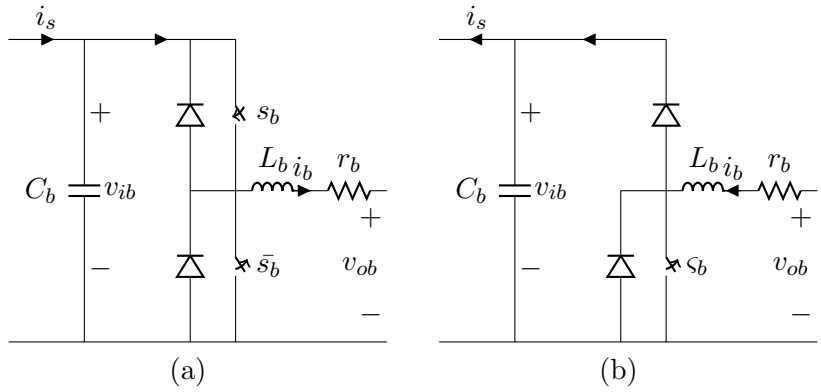

Figure 3.13: Bidirectional converter (a) and boost converter (b).

$$\frac{di_b}{dt} = -\frac{r_b}{L_b} i_b + \frac{v_{ob}}{L_b} - \frac{(1-\varsigma_b)v_{ib}}{L_b} \tag{3.48}$$

$$\frac{dv_{ib}}{dt} = \frac{(1-\varsigma_b)i_b - i_s}{C_b} \tag{3.49}$$

The current controller can be designed as:

$$k_p = 2\rho\omega_o L_b \tag{3.50}$$

$$k_i = \omega_o^2 L_b \tag{3.51}$$

$$\omega_o = 2\pi \frac{f_{sw}}{n_i} \tag{3.52}$$

If the voltage is controlled to regulate DC microgrid voltage, then the controller is:

$$k_{p,v} = 2\rho\omega_o C_b \tag{3.53}$$

$$k_{i,v} = \omega_{o,v}^2 C_b \tag{3.54}$$

$$\omega_{o,v} = \frac{\omega_o}{n_v} \tag{3.55}$$

The bandwidth of the voltage controller is lower than the bandwidth of the current control loop ($\omega_{o,v} < \omega_o$).

Table 3.2: Coordination between grid converters.

Device	Task
DG_1	Controls the DC voltage, master at the DC side.
DG_2, ES_1	Inject constant power, slaves at the DC side.
Pex	Consumes power from the DC side, operates as an slave.
DG_3, ES_2	Autonomous operation, secondary control to regulate voltage and frequency at the AC side.

3.6 Power sharing between distributed generators in the hybrid DC - AC microgrid

Many power sharing techniques are described in the literature [19,25,43,66]. The objective of these technique is to control both the voltage and frequency in the system. These techniques have been categorized as follows: master/slave control techniques, current/power sharing control techniques and voltage and frequency droop control techniques.

The coordination of DGs requires a master/slave at the DC side of the microgrid [43]. Therefore, the voltage is set to its nominal value and controlled by DG_1. The DC slaves inject constant power based on the reference set point. The AC side uses two autonomous DGs, which have internal loops to control the current and voltage. Additionally, droop control is used with a secondary controller to regulate the voltage and frequency of the AC side [60,67,68]. The operation of each device is summarized in table 3.2.

3.6.1 master/slave control technique

Basic master/slave coordination uses a voltage controlled converter as a master unit and current controlled converters as the slave units. The master unit maintains the output voltage, and generates the proper current commands for the slave units [69]. The coordination of the DC bus is based on centralized power management as realized in [25] (Fig. 3.14). In [25], an energy management system was applied to determine the operation modes of the individual converters. This

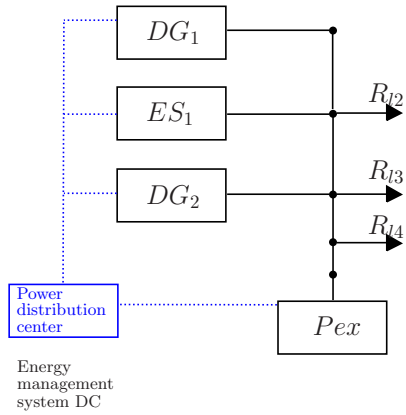

Figure 3.14: DC bus master/slave control technique.

system is based on microgrid power. The operation logic uses power from the DC microgrid ($P_{DC,Gen}$); it is defined as the total DC power generated minus both the total DC load and DC power line losses. If $P_{DC,Gen}$ is less than zero, the Pex must import power into the DC microgrid, but when $P_{DC,Gen} > 0$, the Pex can export the surplus of power. During the stability tests presented in this thesis, it is assumed that the available power from DG_1, DG_2 and ES_1 is higher than the load power (ES_1 can operates in idle, charging or discharging modes). This enables the export of power from the DC microgrid side to the AC microgrid bus. DG_1 controls the voltage of the DC microgrid, DG_2 injects power into the grid and ES_1 may be used in discharging or charging mode.

3.6.2 Time simulation of the microgrid

The simulation results of the hybrid microgrid are shown in the following figures. The system uses full switches in the devices. The time behavior has been low-pass filtered and re-sampled at 0.2 s to show a time frame of 120 s. Figure 3.15 shows the power sharing and the voltage of each DG at the DC side. The test reveals multiple operation points. Pex starts to consume power from the DC side of the microgrid at 5 s. The power consumed increases at 20 and 40 s. The operation of ES_1 is changed at 60 s, from source to load operation. The power consumed by ES_1 increases at 80 s. Finally, ES_1 suddenly disconnects from the microgrid at 100 s.

Figure 3.16 presents the power sharing for ES_2 and DG_3 at the AC side. A

linear load is switched on and off every 5 s from 90 s onwards. The AC voltage at the node pcc_8, the frequency, the d-q voltages and currents of the DGs at the AC side are shown in Fig. 3.17.

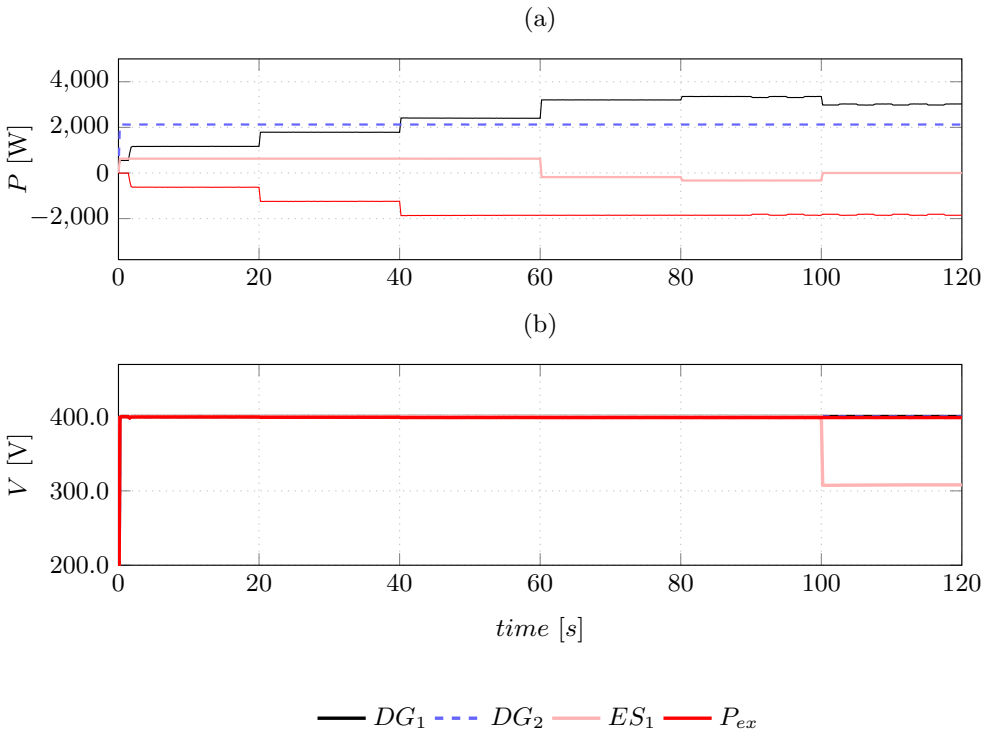

Figure 3.15: Power sharing for the DGs and Pex at the DC side. Power (a) and DC voltages (b).

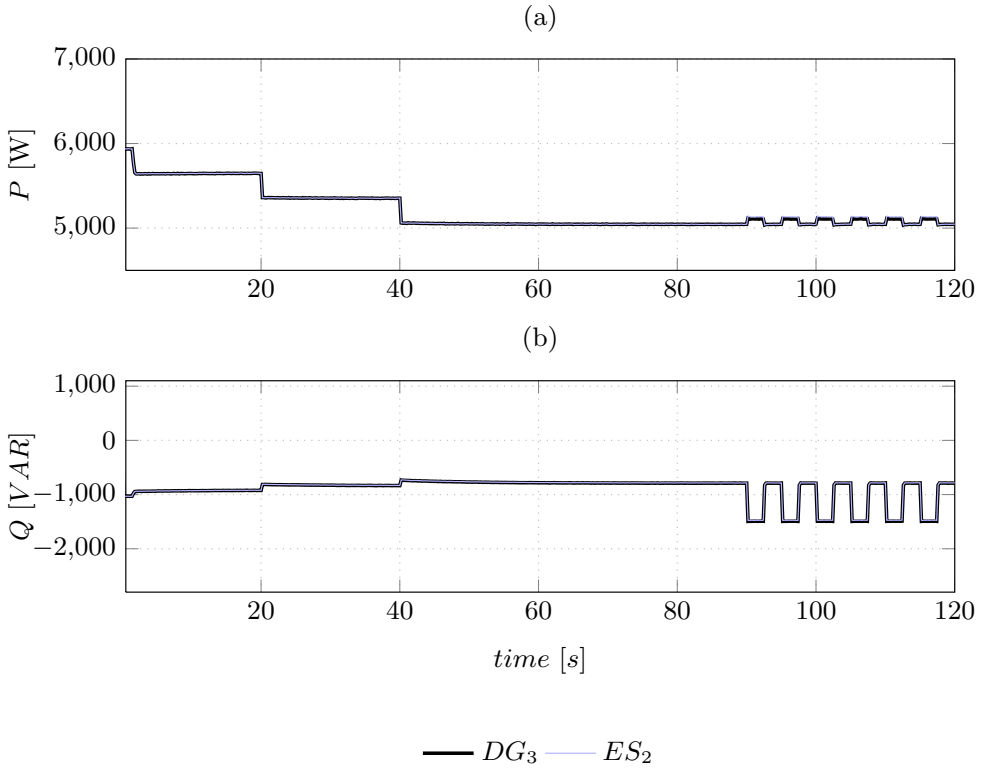

Figure 3.16: Power sharing for the DGs at the AC side. Active power (a) and reactive power (b).

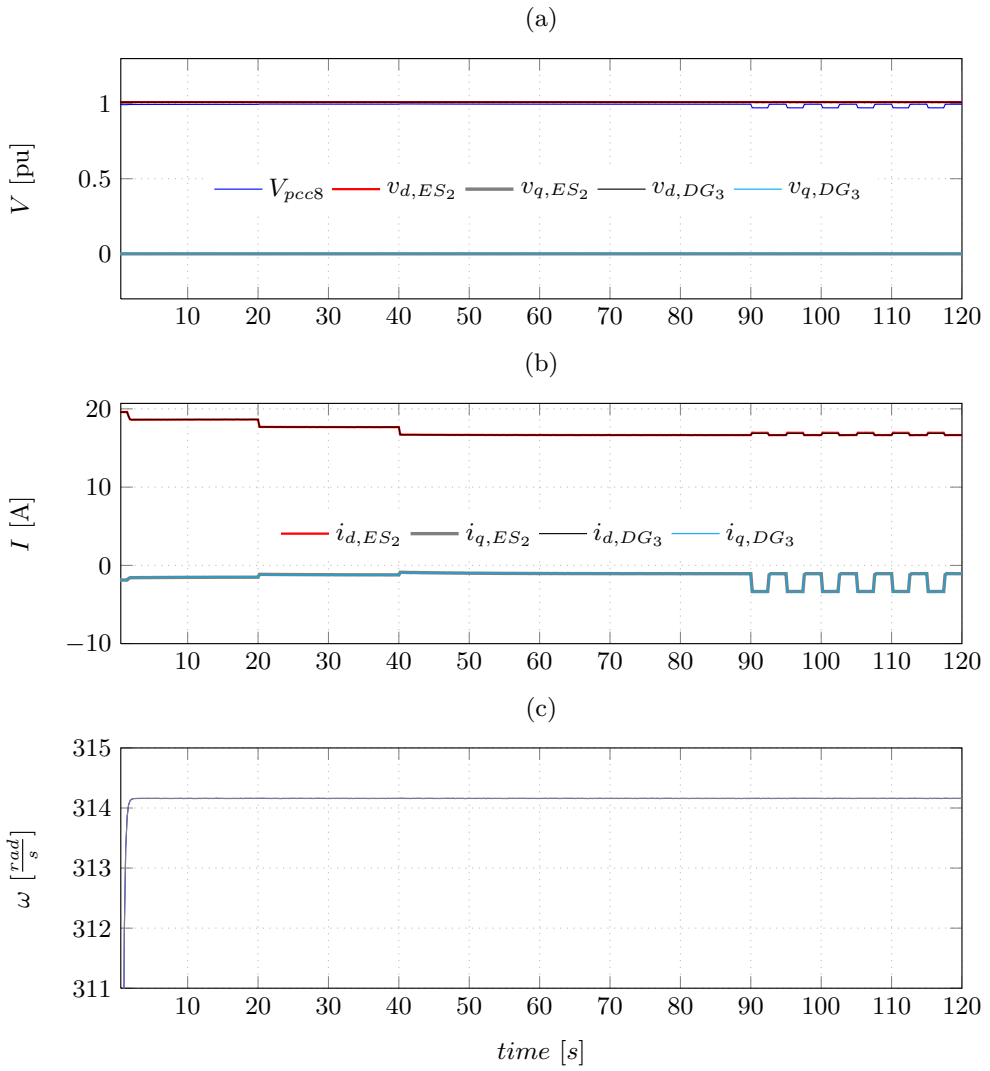

Figure 3.17: Power sharing for the DGs at the AC side. Voltages (a), currents (b) and frequency (c).

Chapter 4

Small signal stability for short term studies

The aim of this chapter is to present the linear technique used to study the stability of the system at the power exchange point, using the frequency response as a mathematical tool.

Linear stability studies of dynamic systems can be performed in the time or frequency domain [10, 54, 60]. The frequency domain approach is applied to the microgrid presented in Fig. 4.1. The objective of the impedance-based stability criterion is to partition the system under test into a source and load subsystem. The technique is based on the use of a Thevenin or Norton circuit equivalent of the source system. The voltage or current source and impedance of this equivalent are in the frequency domain. Therefore, the load also requires an impedance model in frequency domain. Once the models have been obtained, the stability test is performed with Nyquist criteria.

This chapter presents a brief overview of the impedance representation and its application to the Nyquist stability test, which is an analytical model of the DC side of the converter used as a power exchanger. The admittance representation at the AC side of the exchanger device, the AC microgrid equivalent and the stability test for this type of system are also described.

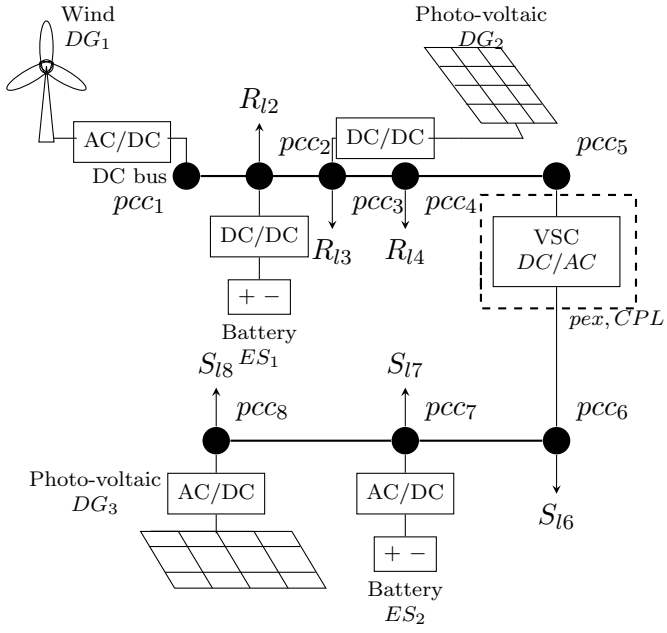

Figure 4.1: Structure of the DC-AC micro-grid used for the AC admittance representation.

4.1 Impedance representation for use Nyquist stability test

The impedance is determined by applying a perturbation in the form of an ideal sinusoidal source with a frequency component. This source is a sinusoidal current or voltage (i_p or v_p respectively). The magnitude has to be small relative to the nominal operation value of the system. The frequency is chosen as f_p varying in range. The input voltage and current are injected and measured at the DC or AC side of the grid or the VSC. Perturbation of the AC side has been performed in unbalanced conditions as shown in Fig. 4.2 (*e.g.* the system can be represented by positive and negative sequence variables from the three phase system). The Fourier transform is computed. The values of the perturbation frequency determines both the input impedance of the inverter for small signal stability analysis and the output impedance of the grid [10,26,32]. The current or voltage injection required to obtain the impedance for the VSC are presented in Fig. 4.2. If the impedance is at the DC side, the AC perturbation is not connected and vice versa for impedance at the AC side.

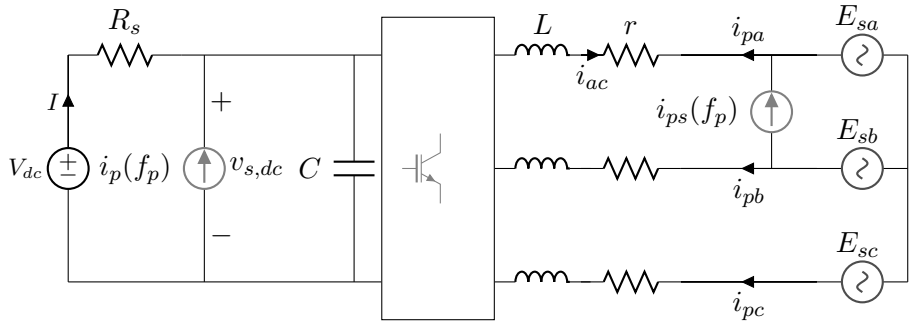

Figure 4.2: Perturbation source for the measurement of impedance.

The stability is analyzed with the Nyquist criteria used in [30, 35]. The full system is partitioned into a source and a load subsystem, which is described by a Thevenin equivalent system when the the source is considered a voltage type (Fig. 4.3a [1]), and a Norton equivalent system when the source is considered a current type (Fig. 4.3b). For the voltage source type, the analysis has to be performed in

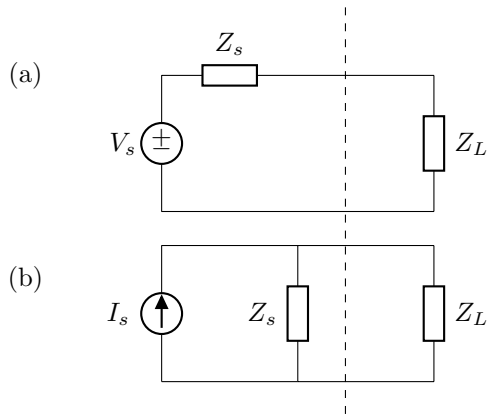

Figure 4.3: Equivalent circuit representation of stability, (a) Thevenin, and (b) Norton.

the Thevenin circuit, and the voltage applied to the load subsystem is calculated in (4.1), where $\mathbf{V}_L$ is the voltage in the load, $\mathbf{Z}_s$ is the output impedance of the source, and $\mathbf{Z}_L$ is the input impedance of the load.

[1] The capital letter denotes a variable function of the frequency ω, *e.g.* $\mathbf{Z}_s(j\omega) \triangleq \mathbf{Z}_s$

$$\mathbf{V}_L = \frac{1}{1 + \frac{\mathbf{Z}_s}{\mathbf{Z}_L}} \mathbf{V}_s \tag{4.1}$$

The relation $\mathbf{Z}_s/\mathbf{Z}_L$ is used to perform the stability analysis. If the Nyquist plot encircles the point $(-1, 0)$ counterclockwise, then the system is unstable. If the Norton equivalent circuit is used, then the current in the load $\mathbf{I}_L$ is (4.2), where $\mathbf{I}_s$ is the source current.

$$\mathbf{I}_L = \frac{1}{1 + \frac{\mathbf{Z}_L}{\mathbf{Z}_s}} \mathbf{I}_s \tag{4.2}$$

The Norton equivalent can be defined by the admittance of the system. The source admittance is $\mathbf{Y}_s = \mathbf{Z}_s^{-1}$ and the load admittance is $\mathbf{Y}_L = \mathbf{Z}_L^{-1}$; therefore, the load current is found by (4.3).

$$\mathbf{I}_L = \frac{1}{1 + \mathbf{Y}_L^{-1}\mathbf{Y}_s} \mathbf{I}_s \tag{4.3}$$

4.1.1 Margin for safe operation at the DC side

The margin stated in [26, 29] describes a forbidden region in DC systems. If the Nyquist plot of the minor loop is outside this region, the system is stable in the small signal response (Fig. 4.4). This criterion guarantees the stability of the relation $\mathbf{Z}_s/\mathbf{Z}_L$ (*i.e.* the minor loop in (4.1)) for a Thevenin equivalent or $\mathbf{Z}_L/\mathbf{Z}_s$ for the Norton equivalent (*i.e.* the minor loop in (4.2)). The minor loop trajectory is plotted in the real-imaginary axes (*e.g.* the frequency response in Fig. 4.4). The region of the margin describes the area for a 30 degree phase margin and -6 dB gain margin [26]. If the trajectory avoids this forbidden region a certain degree of stability is achieved.

4.1.2 Equivalent selection

Several basic steps are required to select an equivalent circuit to perform the stability test. The choice of equivalent circuit strongly influences the stability test. Indeed, this test could show an unstable trajectory if the wrong system is used.

First, the selection is based on the mode of operation of the converter [31]. If the converter injects power into a system ("system A" in Fig. 4.5.a) through an inner current controller, then the Norton equivalent is used. System A consumes this power and is chosen as the load ($\mathbf{Z}_L$). Therefore, the source equivalent is obtained for the converter in this case [70].

Alternatively, the converter may consume power from a system that maintains constant the voltage at the connection point (Fig. 4.5.b). In this case, the

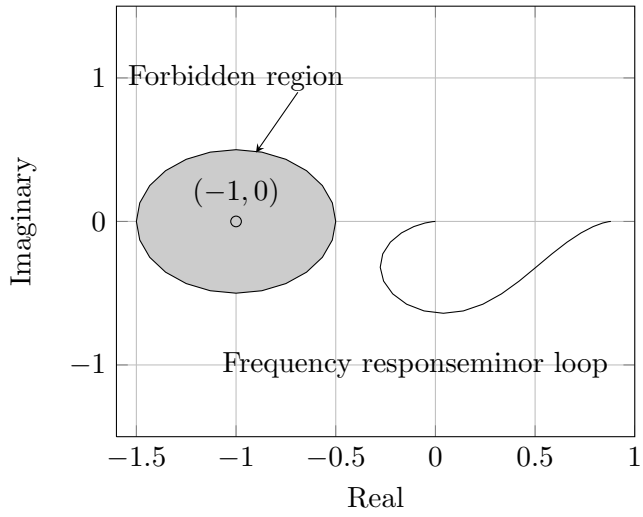

Figure 4.4: Stable margin criteria, forbidden region to guarantee stable behavior. A generic response of a stable system.

Thevenin equivalent is chosen. The converter is represented as the load and $\mathbf{Z}_L$ is calculated. The source is selected as the system A.

4.2 Impedance representation of the Pex at the DC side

DC impedance is described here by three methods. The first involves the linearization of the representation of the state space variables of the differential equations of the converter [52]. The second involves the multi-loop transfer function coupling described in [53,71], and the third method involves a mathematical tool called harmonic linearization [9]. Maple 14 software was used to obtain the models in this section.

4.2.1 State space linearization

The nonlinear function (4.4) can be linearized around an operation point and the resulting system can be described by (4.5)-(4.6). The frequency impedance of the converter is obtained by the method described in [30]: the input of the system is the current of the source (or DC grid at the node), and the states are the AC currents, and the voltage in the DC capacitor, which is also chosen as the output

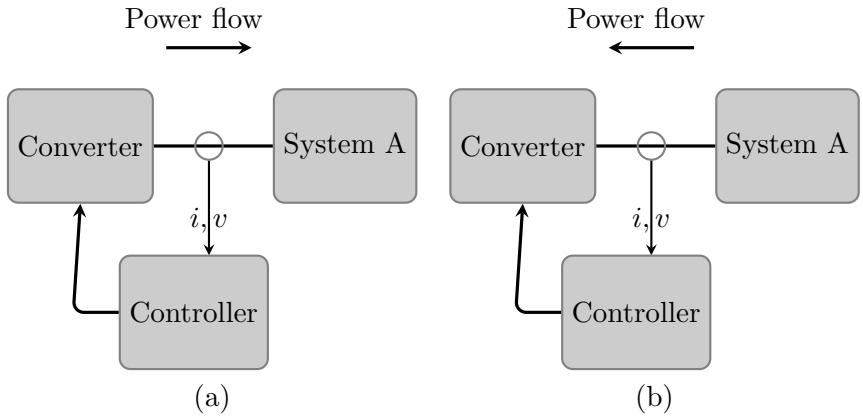

Figure 4.5: Schematic representation of a converter-System connection. (a) Converter injecting power into the system A. (b) Converter consuming power from the system A.

of the system. The complete model is combined with the differential equations for the inverter from (3.23) to (3.27) and the set of equations from (3.28) to (3.31).

$$\dot{x} = f(x, u) \tag{4.4}$$

$$\Delta\dot{x} = A\Delta x + B\Delta u \tag{4.5}$$

$$y = C_m \Delta x \tag{4.6}$$

In this method, the input is equal to the grid current $u = i_{grid}$ and the states are $x = (i_d, i_q, v_{dc}, \gamma_d, \gamma_q)^T$. The impedance in the frequency domain is calculated with (4.7).

$$Z_{dc}(s) = C_m(sI - A)^{-1}B \tag{4.7}$$

The impedance obtained by this method is:

$$Z_{dc}(s) = \frac{(s+\alpha)\,{v_{dc}}^2}{s^2 C {v_{dc}}^2 + sC{v_{dc}}^2\alpha - i_d k_i \gamma_d (s+\alpha) + i_d \alpha\, E_{sd}} \tag{4.8}$$

where C is the DC capacitor of the Pex, α is the parameter of the first-order low-pass feedforward filter used to smooth the measured AC voltage E_{sd} and E_{sq}, γ_d is the state variable of the controller at the d axis, and i_d is the AC current at the d axis.

4.2.2 Relationship between linearization and transfer functions

To obtain the frequency domain impedance representation, the steps used in [53, 71], can be applied to the model of the set (3.23)-(3.31). Maple software

was used for symbolic computation. Algorithm 1 describes the implementation of the method with Maple. First, the models are obtained in the time domain (*i.e.* (3.23)-(3.31)). In the second step, transfer functions are obtained by applying the Laplace transform to the states. Linearization around the operation is required in this step. The model uses power balance between input and output of the converter, with DC power equal to AC power. This balance results in a non-linear system; therefore linearization is applied to the power balance.

The transfer function that represents the impedance is obtained from the relationship between the variables v_{dc} and i_{dc} in the Laplace domain, and the impedance of the full converter is obtained from the parallel equivalent between DC capacitance and the impedance of the converter. The obtained impedance for this system is presented in (4.9)-(4.10), and the final model is shown in (4.11).

Algorithm 1 Calculation of impedance by transfer function approximation.

1: Use Laplace tranform of the dq currents (3.23)-(3.24).
2: Use Laplace tranform of the controller(3.28)-(3.31).
3: Solve (3.27) in (3.26) and linearize.
4: Step 3 produces the linearized power balance P.
5: Solve for $\mathbf{Z}_{vsc}$.
6: Compute the parallel $Z_{dc} = (Z_C| \; |\mathbf{Z}_{vsc})$.

$$Z_{vsc}(s) = \left(-\frac{v_{dc}}{i_{dc}} \frac{v_{dc}(r+sL)^2(s+\alpha)^2}{a_4 s^4 + a_3 s^3 + a_2 s^2 + a_1 s + a_0} \right) \tag{4.9}$$

$$a_k = f_k(K_{ptrans}, G_a, x_0); \quad k \in \{0, ...4\} \tag{4.10}$$

$$Z_{dc}(s) = \frac{Z_C(s) Z_{vsc}(s)}{Z_C(s) + Z_{vsc}(s)} \tag{4.11}$$

where K_{ptrans} is the gain of the power from the abc to the dq reference frame, $G_a = 1/V_{dc}$ at the nominal value, $Z_C(s)$ is the impedance of the DC capacitor in the Laplace domain, and α is the parameter of the first-order low-pass feedforward filter used to smooth the measure of E_{sd} and E_{sq}. The parameter a_k is presented below and the function $G_{is} = k_p + k_i/s$ describes the controller in the Laplace domain.

$$a_4 = i_{dc} L^2 \tag{4.12}$$

$$\begin{aligned} a_3 = {} & K_{trans} {G_a}^2 {G_{is}}^2 {i_{refd}}^2 L v_{dc} \\ & + K_{trans} G_a \alpha \, {i_{refd}}^2 G_{is} L^2 \\ & - 2\, K_{trans} {G_a}^2 E_{sd} G_{is} i_{refd} L v_{dc} \\ & + 2\, i_{dc} L^2 \alpha - K_{trans} G_a \alpha \, i_{refd} E_{sd} L^2 \\ & + 2\, i_{dc} r L + K_{trans} {G_a}^2 {E_{sd}}^2 L v_{dc} \end{aligned} \tag{4.13}$$

$$\begin{aligned} a_2 = {} & -2\, K_{trans} {G_a}^2 E_{sd} G_{is} \alpha \, i_{refd} L v_{dc} \\ & + i_{dc} L^2 \alpha^2 + 4\, i_{dc} r L \alpha \\ & + i_{dc} r^2 - 2\, K_{trans} {G_a}^2 E_{sd} G_{is} i_{refd} r v_{dc} \\ & - K_{trans} G_a \alpha^2 i_{refd} E_{sd} L^2 \\ & + K_{trans} {G_a}^2 {E_{sd}}^2 r v_{dc} \\ & + 2\, K_{trans} G_a \alpha \, {i_{refd}}^2 G_{is} r L \\ & + K_{trans} {G_a}^2 {G_{is}}^2 {i_{refd}}^2 r v_{dc} \\ & - 2\, K_{trans} G_a \alpha \, i_{refd} E_{sd} r L \\ & + 2\, K_{trans} {G_a}^2 {E_{sd}}^2 L v_{dc} \alpha \end{aligned} \tag{4.14}$$

$$\begin{aligned} a_1 = {} & K_{trans} G_a \alpha \, {i_{refd}}^2 G_{is} r^2 \\ & + 2\, i_{dc} r^2 \alpha - 2\, K_{trans} {G_a}^2 E_{sd} G_{is} \alpha \, i_{refd} r v_{dc} \\ & - 2\, K_{trans} G_a \alpha^2 i_{refd} E_{sd} r L \\ & - {v_{dc}}^2 K_{trans} {G_a}^3 G_{is} {i_{refd}}^2 w^2 L^2 \alpha \\ & + {v_{dc}}^2 K_{trans} {G_a}^3 E_{sd} w^2 L^2 \alpha \, i_{refd} \\ & + 2\, i_{dc} r L \alpha^2 + K_{trans} {G_a}^2 {E_{sd}}^2 L v_{dc} \alpha^2 \\ & + 2\, K_{trans} {G_a}^2 {E_{sd}}^2 r v_{dc} \alpha \\ & - K_{trans} G_a \alpha \, i_{refd} E_{sd} r^2 \end{aligned} \tag{4.15}$$

$$\begin{aligned} a_0 = {} & K_{trans} G_a^2 E_{sd}^2 r v_{dc} \alpha^2 \\ & + v_{dc}^2 K_{trans} G_a^3 E_{sd} (wL)^2 \alpha^2 i_{refd} \\ & + i_{dc} r^2 \alpha^2 \\ & - K_{trans} G_a \alpha^2 i_{refd} E_{sd} r^2 v_{dc} \end{aligned} \tag{4.16}$$

4.2.3 Harmonic balance principle

Harmonic balance [52, 72] can be used to obtain the impedance by injecting a sinusoidal perturbation with variable frequency f_p into the converter at the DC side and measuring its effect at the AC side. The approximation is obtained by the assumption described in [73] and [74] and shown in (4.17), which states that no energy is stored in the filters of the DC and AC side.

$$v_{dc}(t)i_{dc}(t) = v_a(t)i_a(t) + v_b(t)i_b(t) + v_c(t)i_c(t) \tag{4.17}$$

where $v_{a,b,c}(t)$, and $i_{a,b,c}(t)$ are the voltage and current for the AC side, respectively. The variable $v_{dc}(t)$ is presented as a time variable signal as in (4.18), to enable the inclusion a sinusoidal perturbation voltage applied at the DC side, which in turn results in the small signal impedance. Thus, the current $i_{dc}(t)$ at the DC side is also expected to be a time variable.

$$v_{dc}(t) = V_d + V_p cos(\omega_p t) \tag{4.18}$$

where V_d and V_p are the constant component, and the perturbation maximal value, respectively and ω_p is the angular frequency of the perturbation signal.

To evaluate the left hand side of (4.17), the time variable DC current is assumed as in (4.19) with a constant component I_d, a perturbation value I_p, and a lagged angle ϕ_p.

$$i_{dc}(t) = I_d + I_p cos(\omega_p t - \phi_p) \tag{4.19}$$

The evaluation of (4.18), and (4.19) in the left hand side of (4.17) is presented in (4.20).

$$\begin{aligned} p_{dc}(t) =& I_d V_d + \frac{1}{2} I_p V_p cos(\phi_p) + I_d V_p cos(\omega_p t) + \\ & I_p V_d cos(\omega_p t - \phi_d) + \frac{1}{2} I_p V_p cos(2\omega_p t - \phi_d) \end{aligned} \tag{4.20}$$

The PWM signals are obtained by comparing a triangular waveform $v_{tri}(t)$ with the peak value V_{tri} and the control voltages $v_{Ck}(t) = V_C cos(\omega_e t - \gamma_k)$ in which $k = \{a, b, c\}$ and $\gamma_k = \{0, 120, 240\}$ degrees in each respective phase. The duty ratios in the average representation can be written as in (4.21) [74].

$$d_k(t) = 0.5 + 0.5 \frac{V_C}{V_{tri}} cos(\omega_e t - \gamma_k) \tag{4.21}$$

The duty ratios of (4.21) and the time variable DC voltage are used to obtain the phase to neutral voltages, which in turn gives (4.22) and (4.23).

$$v_{kN}(t) = d_k(t)v_{dc}(t) \tag{4.22}$$

$$\begin{aligned} v_{kN}(t) =& \frac{V_d}{2} + \frac{V_d V_C}{2V_{tri}} cos(\omega_e t - \gamma_k) + \frac{V_p}{2} cos(\omega_p t) + \\ & \frac{V_p V_C}{8V_{tri}} \left[2cos\left((w_e + w_p)t - \gamma_k\right) + \right. \\ & \left. 2cos\left((w_e - w_p)t - \gamma_k\right)\right] \end{aligned} \tag{4.23}$$

The terms $0.5V_d$, and $0.5V_p cos(\omega_p t)$ in (4.23) are offset voltages. In each phase, they are considered zero-sequence voltages, as was the case in [74] for the term $0.5V_d$; therefore, they do not produce current flow in the balanced three phase load. As a result, the average phase-to-neutral voltages for the balanced star load with neutral n are described by (4.24).

$$\begin{aligned} v_{kn}(t) =& \frac{V_d V_C}{2V_{tri}} cos(\omega_e t - \gamma_k) + \\ & \frac{V_p V_C}{4V_{tri}} \left[cos\left((w_e + w_p)t - \gamma_k\right) + \right. \\ & \left. cos\left((w_e - w_p)t - \gamma_k\right)\right] \end{aligned} \tag{4.24}$$

In (4.24), there are three frequency components and each signal has its respective maximum value. To facilitate the use of (4.24), it has been written as (4.25), where $V_1 \neq V_2$, and $V_2 = V_3$.

$$\begin{aligned} v_{kn}(t) =& V_1 cos(\omega_e t - \gamma_k) + \\ & V_2 cos\left((w_e + w_p)t - \gamma_k\right) + \\ & V_3 cos\left((w_e - w_p)t - \gamma_k\right) \end{aligned} \tag{4.25}$$

Assuming that the system has a linear part the currents in each phase are expected to have the same frequency components as the voltages, and their respective lagged load angle. Furthermore, the magnitude of the current in its respective frequency is assumed to be proportional to the magnitude of the impedance at the same frequency. Hence, the current in each phase is (4.26).

$$\begin{aligned} i_{kn}(t) =& I_1 cos(\omega_e t - \gamma_k - \phi_1) + \\ & I_2 cos\left((w_e + w_p)t - \gamma_k - \phi_2\right) + \\ & I_3 cos\left((w_e - w_p)t - \gamma_k - \phi_3\right) \end{aligned} \tag{4.26}$$

The magnitudes I_1, I_2, and I_3 in (4.26) are functions of the three phase balanced equivalent AC impedance, which is in turn frequency-dependent, and notated as $Z_1(\omega_e)$, $Z_2(\omega_e+\omega_p)$, and $Z_3(\omega_e-\omega_p)$. Therefore, the angles of the load are $\phi_1(\omega_e)$, $\phi_2(\omega_e+\omega_p)$, and $\phi_3(\omega_e-\omega_p)$.

The controller can be added assuming that there is a PI regulator in the converter and the reference current can be modeled by $i_{refk} = I_{ref} cos(\omega t - \phi_1 - \gamma_k)$. The integrated reference current is $\int i_{refk} = (I_{ref}/\omega) sin(\omega t - \phi_1 - \gamma_k)$. The controller is applied to the variable V_C for each phase as follows:

$$V_{Ck} = k_p \left(i_{refk} - i_{kn}\right) + k_i \int \left(i_{refk} - i_{kn}\right) dt \tag{4.27}$$

Equations (4.25), (4.26) and (4.27) are used in the right hand side of (4.17) to obtain the AC power (4.28) at the injected perturbation frequency and to build the model that describes the impedance.

$$p_{ac}(w_p t) = K_{pac} \left(k_p f_{1power}(\omega_p t) + k_i f_{2power}(\omega_p t)\right) \tag{4.28}$$

where K_{pac} is the gain of the power obtained. The functions $f_{lpower}(\omega_p)$ with $l \in \{1, 2\}$ describes the power functions obtained for the proportional and integral controller, respectively. The equation (4.28) is compared with the fourth term of (4.20) to obtain an expression for the perturbation current i_p. A complex notation, (4.29)-(4.35), is then used to find the value of I_p as a function of the AC impedance in frequency.

$$\boldsymbol{I}_{p,kp} = k_p(\boldsymbol{I}_3(w_e w_p^2 - w_e^3) + \boldsymbol{I}_2(w_e w_p^2 - w_e^3)) \\ I_1 e^{-j\phi_1} \tag{4.29}$$

$$\boldsymbol{I}_{p,ki} = k_i(\boldsymbol{I}_{3b}(-w_e w_p - w_e^2) + \boldsymbol{I}_{2b}(w_e w_p - w_e^2)) \\ I_1 e^{-j(\phi_1+\pi/2)} \tag{4.30}$$

$$\boldsymbol{I}_2 = I_2 e^{-j\phi_2} \tag{4.31}$$

$$\boldsymbol{I}_{2b} = \boldsymbol{I}_2 e^{-j(\phi_2+\pi/2)} \tag{4.32}$$

$$\boldsymbol{I}_3 = I_3 e^{-j\phi_3} \tag{4.33}$$

$$\boldsymbol{I}_{3b} = \boldsymbol{I}_3 e^{-j(\phi_3+\pi/2)} \tag{4.34}$$

$$\boldsymbol{I}_p = \frac{(\boldsymbol{I}_{p,kp} + \boldsymbol{I}_{p,ki})}{V_{tri}(w_e^3 - w_e w_p^2)} \tag{4.35}$$

The next step is to compute the impedance from the equation presented in (4.36). $\mathbf{V}_p(\omega)$ is the known perturbation voltage in complex form. Finally, the complete converter impedance is found by the parallel of the capacitor and (4.36).

$$\boldsymbol{Z}_{dc}(\omega) = \frac{\boldsymbol{V}_p(\omega)}{\boldsymbol{I}_p(\omega)} \tag{4.36}$$

4.2.4 Impedance results for the Pex and microgrid equivalent at the DC side

Simulation results

The DC side microgrid is shown in Fig. 4.7. Table 4.1 shows the coordination and the operation point of the devices in the DC microgrid. The DC voltage is controlled at 400 V. The impedances of the Pex at the DC side and microgrid are presented in Fig. 4.8 and Fig. 4.9. A database was created by real time simulation with Simulink-Matlab software and an OPAL-RT device to validate and to compare the models obtained by the impedance representation. A Hardware-in-the loop methodology was used in the test (Fig. 4.6). Here, the microgrid is simulated in real time using the OPAL-RT platform. The perturbation is injected and measured with a network analyzer Agilent E5061B at node pcc_5 in the microgrid. Parallel current perturbation was applied to the microgrid through the analog input of the OPAL-RT with the network analyzer output. This perturbation contains a frequency sweep from 10 to 5 kHz. This impedance has been computed from the relationship between the input signals, *i.e.* voltage and current, of the network analyzer. Maple software was used for symbolic computation

of the equations. The impedances of the VSC were thus obtained, and the DC microgrid was calculated by the injection of a DC perturbation current at node pcc_5 in Fig. 4.7. The node will be used to interconnect the systems. Fig. 4.8 and Fig. 4.9 show the impedance behavior of each system. Table A.3 shows two cases for the DC inductor (L_{fvsc}). L_{fvsc} is used to filter the switching effect in the Pex. This inductor has been assumed as part of the microgrid equivalent. The first case involves a low inductor (case A), whereas the second case involves a high inductive parameter (case B).

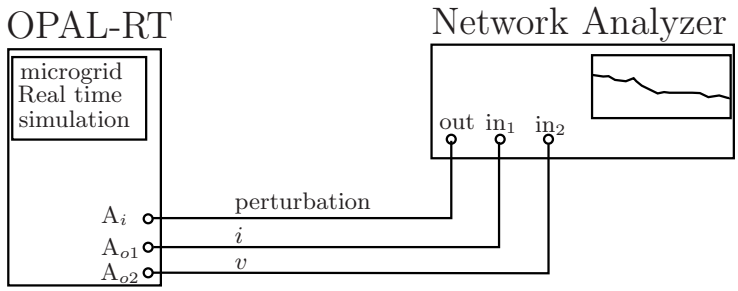

Figure 4.6: Hardware in a loop scheme to measure the impedance of the DC microgrid.

Table 4.1: Operation point of elements of the DC microgrid.

Control type	Device	Power
Voltage	DG_1	3.8 kW
Current	DG_2	3.525 kW
Current	ES_1	1.9 kW
Current	Pex	0.6 kW
-	R_{l2}	2.5 kW
-	R_{l3}	5 kW
-	R_{l4}	1.125 kW

Analysis of the behavior of the microgrid (Fig. 4.9) reveals the presence of an inductive response at low frequency around 10 Hz. In case A, the low frequency response shows a positive gain and phase, which are characteristics of series resistance-inductor impedance. At frequencies above 100 Hz, the system shows a similar response.

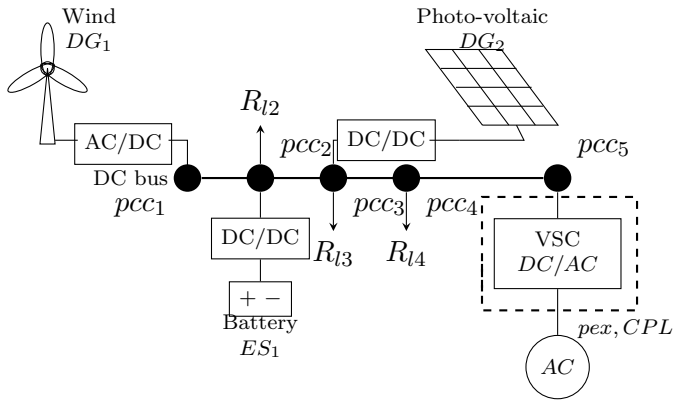

Figure 4.7: Topology of the DC microgrid used for the DC impedance representation.

Nyquist test. The stability of the system was subsequently tested with the Nyquist criteria and a Thevenin equivalent system. Figure 4.10 shows the results for case A. $\mathbf{Z}_{\mu grid}$ is the impedance of the microgrid equivalent and $\mathbf{Z}_{pexDC}$ is the Pex impedance at the DC side. The connection is stable, with a phase margin to provide the stability. The response does not reach this margin and does not encricle the point (-1+j0). Figure 4.11 shows the response crossing through the stability margin. However, the response of the systems is stable as in case A: it does not encircle the point (-1+j0), but the margin has been violated. Therefore, a large inductive microgrid impedance equivalent at the operation point is required for the Nyquist response to resemble closely the stability margin established in [26].

4.3 Admittance representation for the Pex and microgrid equivalent at the AC side

This section presents the methodologies developed in [30,75] and [10] with respect to AC perturbations. In the first test an admittance matrix is obtained in the synchronous reference frame. The second method involves the representation of the admittance in the positive and negative sequence.

The microgrid configuration used is presented in Fig. 4.12. Table 4.2 shows the coordination and the operation point of the devices in the AC and DC microgrid.

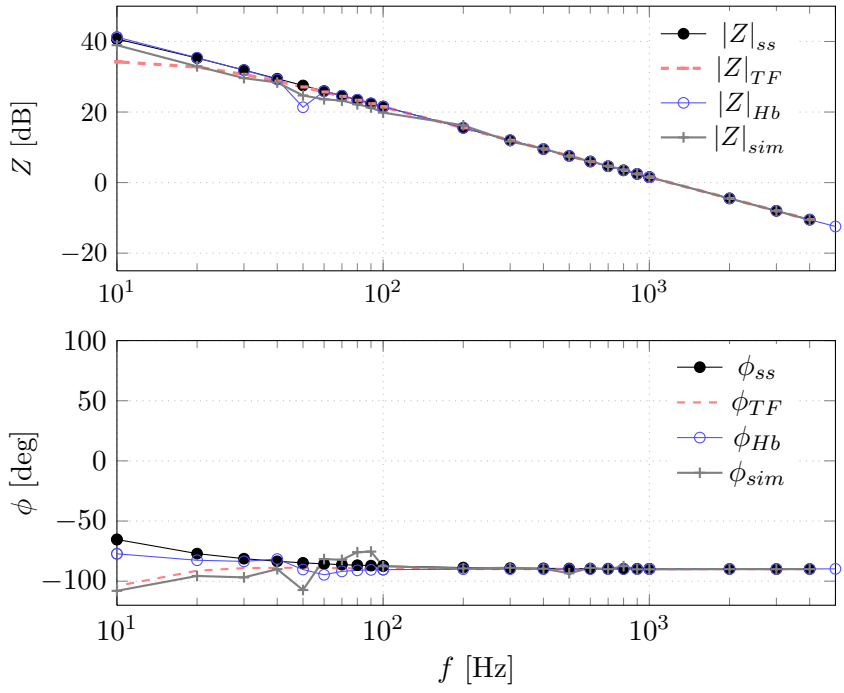

Figure 4.8: Impedance for the VSC system operating at $5\%P_n$, (ss) state space, (TF) transfer function approximations, (Hb) harmonic balance, and (sim) simulation.

The DC voltage is controlled at 400 V, and the peak AC voltage is 200 V. The AC distributed generators operate with secondary control; they regulate the voltage (V) and frequency (ω).
The node used to inject the AC perturbation is pcc_6. A line to line perturbation has been used to obtain the admittances of the converter and the AC side of the microgrid. This perturbation has been added as shown in Fig. 4.2.

4.3.1 Admittance test in the synchronous reference frame

The method applied to obtain the admittances uses line-to-line current perturbation (see Fig. 4.2) [75]. The system does not have zero-sequence current. Two independent sets of data were created to develop the system in the dq reference frame. Each data set is used with the perturbation at a defined frequency in the test. The admittance matrix and elements are presented in (4.37).

$$\mathbf{Y} = \begin{bmatrix} Y_{dd}\angle\phi_{dd} & Y_{dq}\angle\phi_{dq} \\ Y_{qq}\angle\phi_{qq} & Y_{qd}\angle\phi_{qd} \end{bmatrix} \tag{4.37}$$

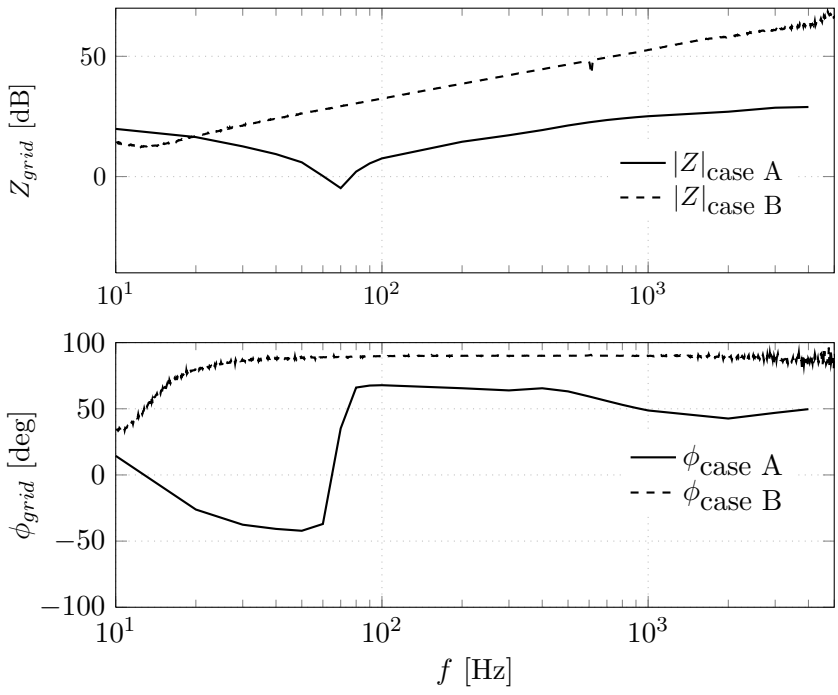

Figure 4.9: Microgrid impedance, magnitude and phase frequency responses. Parallel current perturbation cases: $Z\angle\phi_{\text{case A}}$ and $Z\angle\phi_{\text{case B}}$.

The admittance matrix is composed of four unknown complex elements showun in (4.37): Y_{dd}, Y_{dq}, Y_{qd}, and Y_{qq}. Therefore, two sets of measurements are needed to solve the linear system of equations in (4.38). The subscripts 1 and 2 of the dq quantities indicate the data set in which they take part.

$$\begin{bmatrix} \mathbf{I}_{d1} & \mathbf{I}_{d2} \\ \mathbf{I}_{q1} & \mathbf{I}_{q2} \end{bmatrix} = \begin{bmatrix} Y_{dd}\angle\phi_{dd} & Y_{dq}\angle\phi_{dq} \\ Y_{qq}\angle\phi_{qq} & Y_{qd}\angle\phi_{qd} \end{bmatrix} \begin{bmatrix} \mathbf{V}_{d1} & \mathbf{V}_{d2} \\ \mathbf{V}_{q1} & \mathbf{V}_{q2} \end{bmatrix} \tag{4.38}$$

The set of independent currents used is presented in (4.39) for the abc frame. From the reference used in Fig. 4.2, the peak value of the measured current is I_m. In this injection positive (f_e) and negative ($-f_e$) fundamental frequencies are added to the frequency of interest f_p. The subscripts 1 and 2 of the abc quantities

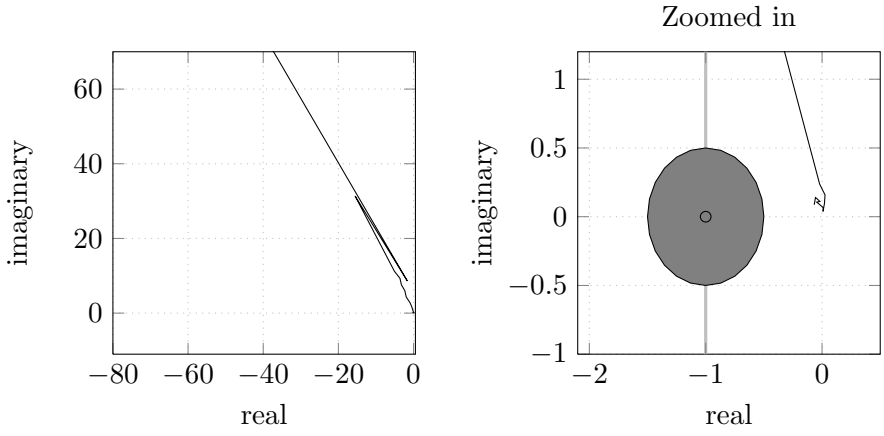

Figure 4.10: Nyquist criteria for $\mathbf{Z}_{\mu grid}/\mathbf{Z}_{pexDC}$ in case A.

indicate the data set in which they take part.

$$\begin{aligned} i_{pa1} &= I_m cos(2\pi(f_p + f_e)t) \\ i_{pb1} &= -I_m cos(2\pi(f_p + f_e)t) \\ i_{pc1} &= 0 \\ i_{pa2} &= I_m cos(2\pi(f_p - f_e)t) \\ i_{pb2} &= -I_m cos(2\pi(f_p - f_e)t) \\ i_{pc2} &= 0 \end{aligned} \tag{4.39}$$

When transformed to the synchronous reference frame, the set of perturbations take the form shown in (4.40). The terms at $|f_p \pm 2f_e|$ can be neglected to balance the harmonics. This gives rise to a couple of linearly independent vectors, which can be used to obtain the admittance. Algorithm 2 presents the method followed to calculate the complete admittance matrix in dq.

$$\begin{aligned} i_{pd1} &= \frac{1}{\sqrt{3}} I_m sin(2\pi f_p t) + ... \\ i_{pq1} &= \frac{1}{\sqrt{3}} I_m cos(2\pi f_p t) + ... \\ i_{pd2} &= -\frac{1}{\sqrt{3}} I_m sin(2\pi f_p t) + ... \\ i_{pq2} &= \frac{1}{\sqrt{3}} I_m cos(2\pi (f_p) t) + ... \end{aligned} \tag{4.40}$$

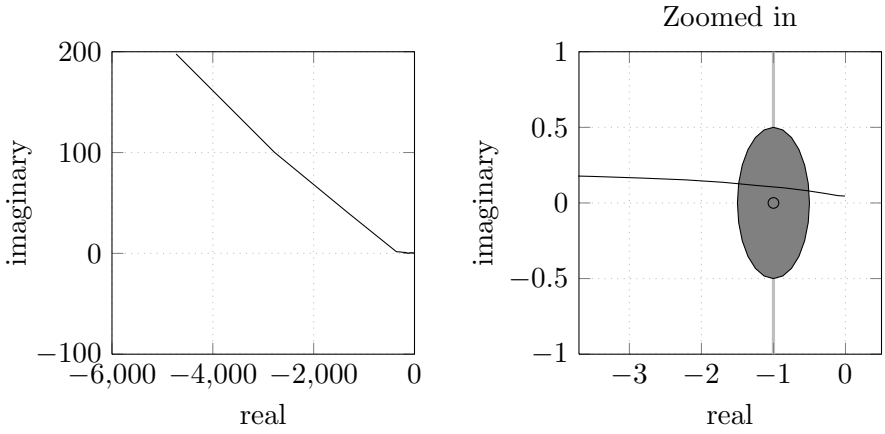

Figure 4.11: Nyquist criteria for $\mathbf{Z}_{\mu grid}/\mathbf{Z}_{pexDC}$ in case B.

Algorithm 2 Calculation of admittance in the synchronous reference frame.

1: **for** $f_p = f_{p,min}$ **to** $f_{sw}/2$ **do**
2: Inject current at $|f_p + f_e|$.
3: Capture time domain data i_{abc} and v_{abc}.
4: Transform from abc to dq quantities.
5: Use the Fourier transform, extract $\mathbf{I}_{pd1}$, $\mathbf{I}_{pq1}$, $\mathbf{V}_{pd1}$ and $\mathbf{V}_{pq1}$.
6: Inject current at $|f_p - f_e|$.
7: Capture time domain data i_{abc} and v_{abc}.
8: Transform from abc to dq quantities.
9: Use the Fourier transform, extract $\mathbf{I}_{pd2}$, $\mathbf{I}_{pq2}$, $\mathbf{V}_{pd2}$ and $\mathbf{V}_{pq2}$.
10: Solve for $\mathbf{Y}$ in (4.38).
11: **end for**

Figure 4.13 shows the results of simulations in which the perturbation is applied at the pcc_6. This perturbation has been injected for the positive and negative sequence. Voltage and current signals in the three-phase abc representation have been stored and post-processed to obtain the synchronous reference frame. Fourier transform can be obtained with the system in dq and the samples of the frequency spectra at f_p are used.

Nyquist test. The stability test is applied in matrix form as in [30]. Hence, the generalized Nyquist criterion is applied to this type of representation. Algorithm 3 shows the steps to obtain the generalized Nyquist criterion for a Norton equivalent system, *i.e.* $[Y_{AC\mu grid}]^{-1}[Y_{pexAC}]$. The microgrid admittance, $Y_{AC\mu grid}$, is

Table 4.2: Operation point of elements of the microgrid elements.

Control type	Device	Power
Voltage	DG_1	3.8 kW
Current	DG_2	3.525 kW
Current	ES_1	1.9 kW
Current	Pex	0.6 kW
V,ω, secondary	DG_3	5.6 kW, 1 kVAR
V, ω, secondary	ES_2	5.6 kW, 1 kVAR
-	R_{l2}	2.5 kW
-	R_{l3}	5 kW
-	R_{l4}	1.125 kW
-	S_{l6}	0 W
-	S_{l7}	5.9 kW
-	S_{l8}	5.9 kW

considered the load for the Norton circuit, and the converter admittance, Y_{pexAC}, is used as the source. It can be seen from the test in Fig. 4.14 that the generalized Nyquist criterion does not encircle the point (-1,j0) in the real-imaginary plane. The parameters λ_1 and λ_2 are the eigenvalues of the complex matrix $[Y_{AC\mu grid}]^{-1}[Y_{pexAC}]$.

Algorithm 3 Generalized Nyquist criterion algorithm.

1: **for** $f_p = f_{p,min}$ **to** $f_{sw}/2$ **do**
2: Obtain the matrix $GN(f_p) = [Y_{AC\mu grid}(f_p)]^{-1}[Y_{pexAC}(f_p)]$.
3: Calculate the eigenvalues λ of $GN(f_p)$.
4: **end for**
5: Plot the eigenvalues λ in the real-imaginary axes.
6: Veryfy that λ do not encircle the point (-1,j0).

4.3.2 Admittance test in the positive and negative sequence

This section describes the application of the positive (p) and negative (n) sequence test developed in [76]. A line-to-line current perturbation is injected into the test developed in this section, *i.e.* the set of currents described in (4.41), and the data is post-processed at each frequency. A Fourier spectrum is obtained for three-phase voltages and currents at each frequency perturbation, with the data set for the complete range of the perturbation. A symmetrical component transformation has also been applied to extract the positive and negative sequence components at each point, and the admittance is computed from this new data set. The

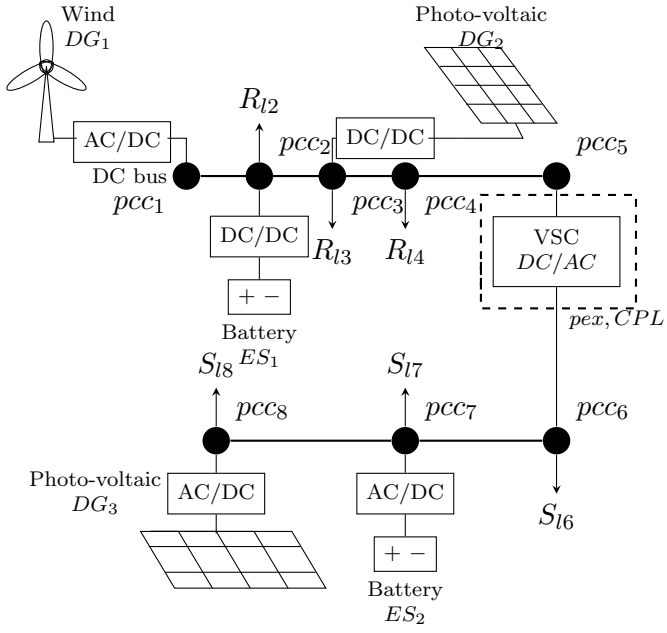

Figure 4.12: Structure of the DC-AC micro-grid used for the AC admittance representation.

admittances are defined in (4.42) for the positive and negative sequence. Two separate systems are obtained with this formula. Hence, positive and negative admittances can be computed from (4.43). Algorithm 4 describes the procedure used to obtain the admittances. The AC microgrid equivalent and P_{ex} admittances are shown in Fig. 4.15.

$$\begin{aligned} i_{pa} &= I_m cos(2\pi f_p t) \\ i_{pb} &= -I_m cos(2\pi f_p t) \\ i_{pc} &= 0 \end{aligned} \tag{4.41}$$

$$\mathbf{Y} = \begin{bmatrix} Y_p \angle \phi_p \\ Y_n \angle \phi_n \end{bmatrix} \tag{4.42}$$

$$\mathbf{I}_p = (Y_p \angle \phi_p)\mathbf{V}_p \tag{4.43}$$

$$\mathbf{I}_n = (Y_n \angle \phi_n)\mathbf{V}_n \tag{4.44}$$

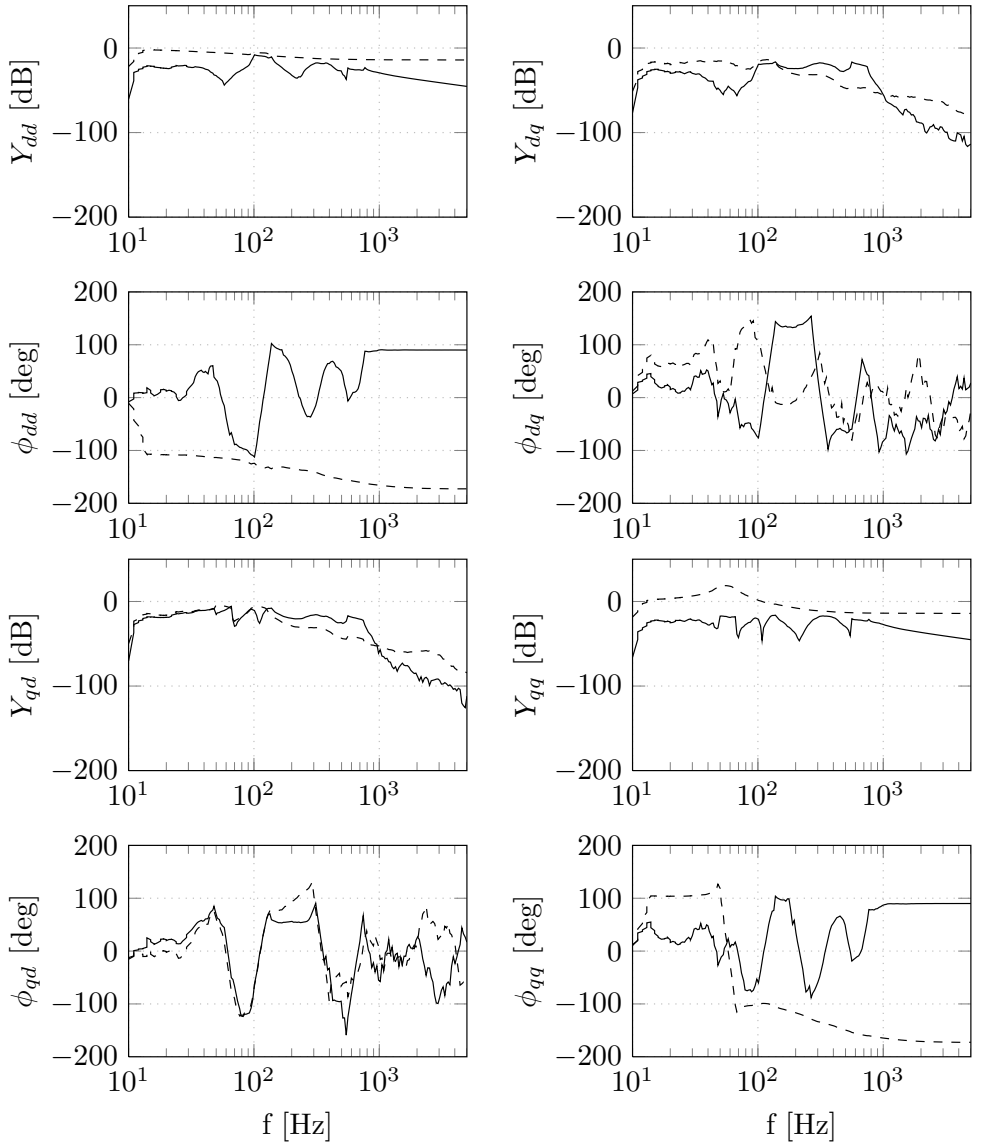

Figure 4.13: Admittance representation for the AC microgrid (dashed) and the P_{ex} (solid). Synchronous reference frame.

The Nyquist test for this representation is shown in Fig. 4.16. Two tests were carried out separately, one for the positive and other for the negative sequence. The Nyquist plots do not encircle the point (-1,j0) in the real-imaginary plane.

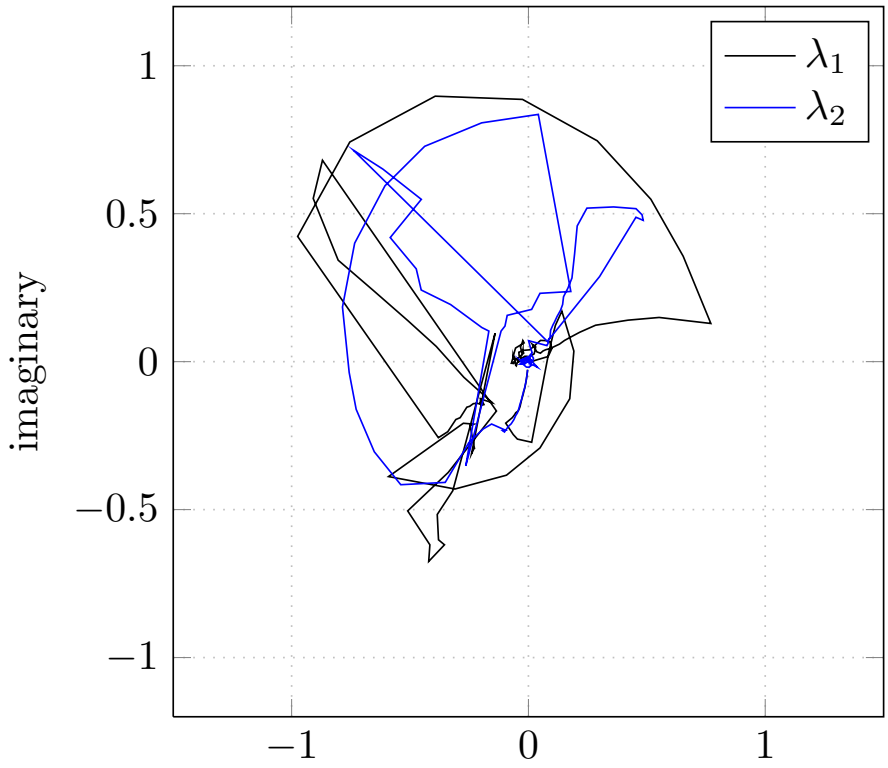

Figure 4.14: Generalized Nyquist criterion for matrix $[Y_{AC\mu grid}]^{-1}[Y_{pexAC}]$.

4.4 Time domain simulation

In this section, the time behavior of the microgrid described in Fig. 3.1 is presented. The full switched model of the devices was used for the tests. Cases A and B are presented for the DC microgrid connection. The responses are located at the operation point, and a small disturbance has been added to each test. The AC response is presented for the case A in this section. The response at the AC side for case B was very similar; therefore, the tests are presented in Appendix C.

4.4.1 DC power sharing for cases A and B

The time domain test is shown in Fig. 4.17 for the DC side of the microgrid in case A. This figure shows the transient behavior for a small disturbance added at the Pex. Fig. 4.17b shows a high ripple in the current $i_{dc,pex}$, due to the low value of the DC filter inductor. The power consumed by the Pex shows a step change

Algorithm 4 Calculation of admittance in the positive and negative sequence.

1: **for** $f_p = f_{p,min}$ **to** $f_{sw}/2$ **do**
2: Inject current at f_p.
3: Capture time domain data i_{abc} and v_{abc}.
4: Use the Fourier transform, extract $\mathbf{I}_{pa}$, $\mathbf{I}_{pb}$, $\mathbf{I}_{pc}$, $\mathbf{V}_{pa}$, $\mathbf{V}_{pb}$ and $\mathbf{V}_{pc}$.
5: Transform from abc to pn quantities.
6: Solve for $\mathbf{Y}$ in (4.43).
7: **end for**

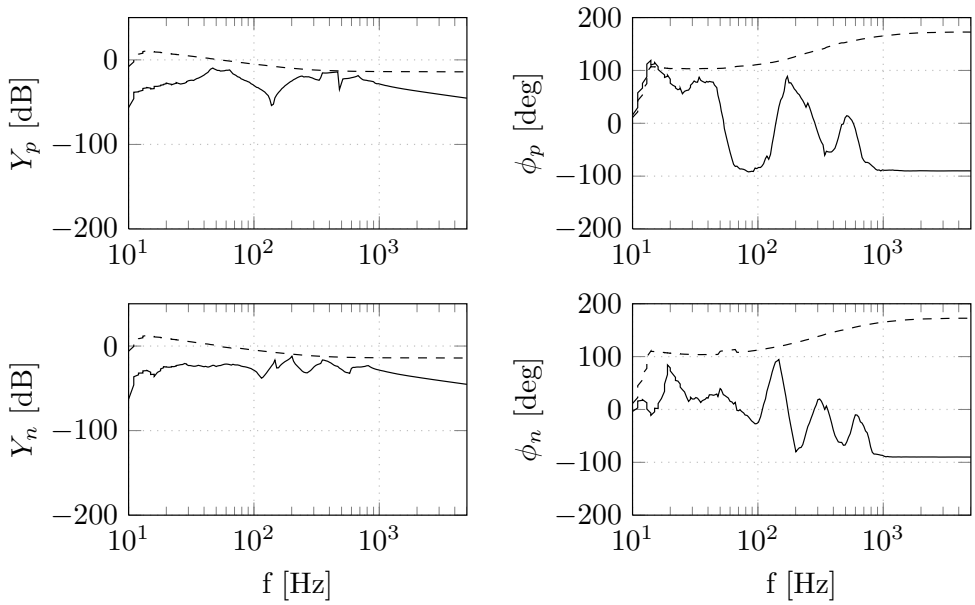

Figure 4.15: Positive and negative sequence admittance representation for the AC grid (dashed) and the P_{ex} (solid).

increase of 80 W. The step change is not very clear in this test due to the low value of the input filter of the Pex, which leads to high ripple behavior. The step occurs at 5.0s and the system maintains stability by producing a compensation of power from DG_1. The double loop controller of DG_1 maintains the operation voltage around the nominal value. The power shared is shown in Fig. 4.17. The input power to DGs must be constant during the time interval studied.

The time result for case B is presented in Fig. 4.18. The signals are smoothed by the large filter inductor at the DC side of the Pex. Figure 4.18 shows that

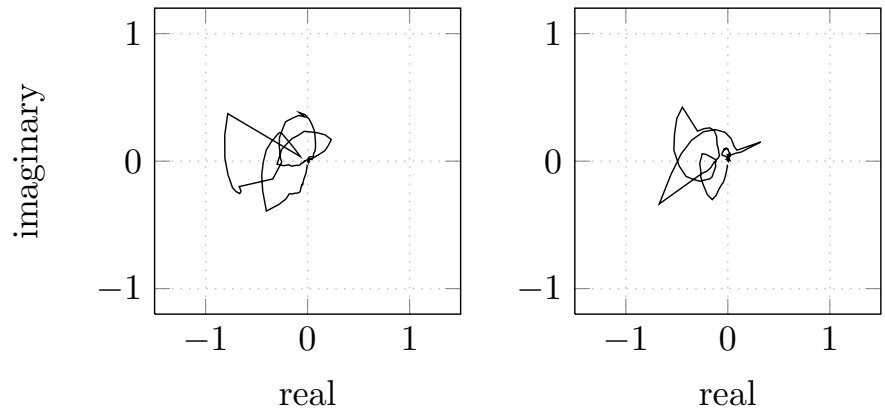

Figure 4.16: Positive and negative sequence Nyquist criteria at the pcc_6 node.

the operation point is stable and that the power shared at steady state is the same as in case A. However, the step change of 80 W power occurs at 5.0 s, and compensatory power is produced by DG_1. It is important to remark that this system violates the margin criteria. Indeed, the curve of the Nyquist response is close to the point -1+j0 in the real-imaginary plane, explaining how this system remains stable during small perturbations.

4.4.2 AC power sharing for case A

Figure 4.19 shows the active power and reactive power shared by DG_3 and ES_2 at the AC side. Each device produces 5.6 kW of active power and the reactive power is 1 kVAR. The system remains stable as can be seen from the voltage at the node pcc_8 Fig. 4.20, which is around 1 pu. The electrical frequency speed is also stable with a value of $2\pi 50$ rad/s.

4.5 Proof of concept

The system used to obtain the experimental impedance is described in Fig. 4.21 and the test bench picture is shown in the Fig. 4.22. The method used to compute the impedance in the frequency domain is presented in algorithm 5. The source v_{gen} is the perturbation signal with variable frequency produced by a signal generator (1). This is isolated by a small power transformer and connected to a linear amplifier (2), hence the perturbation is applied to the DC grid by the secondary of the transformer (v_p). The V_{dc} is a programmable DC source (3), and the impedance is obtained from the value of the voltage v_m and the current i_m (4). The capacitor of the voltage source converter (5) is coupled to the

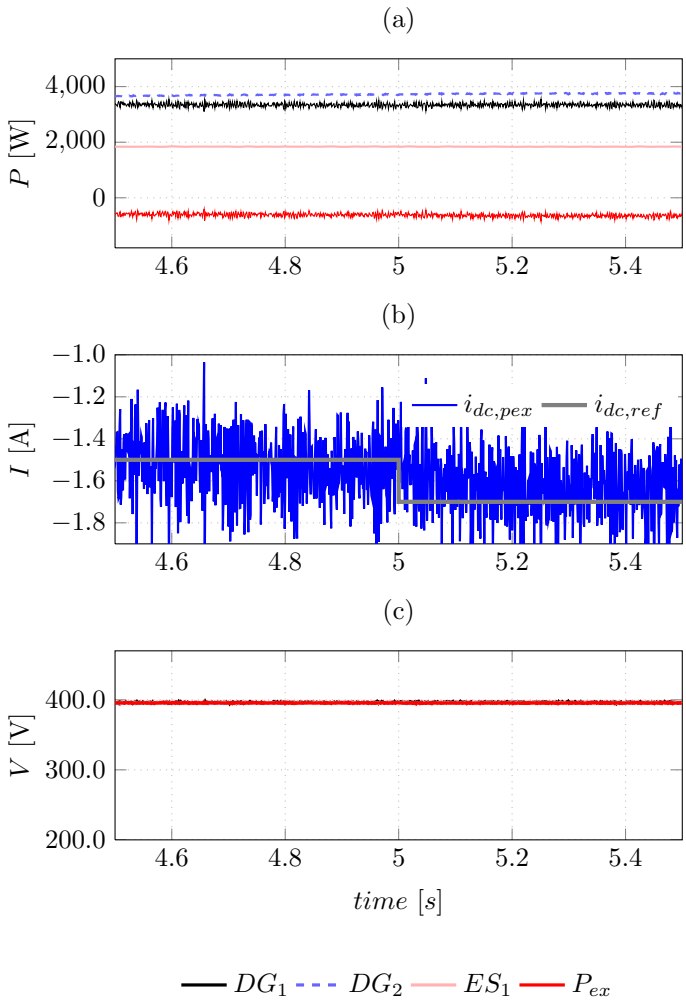

Figure 4.17: Power sharing between the DGs and the Pex at the DC side, case A.

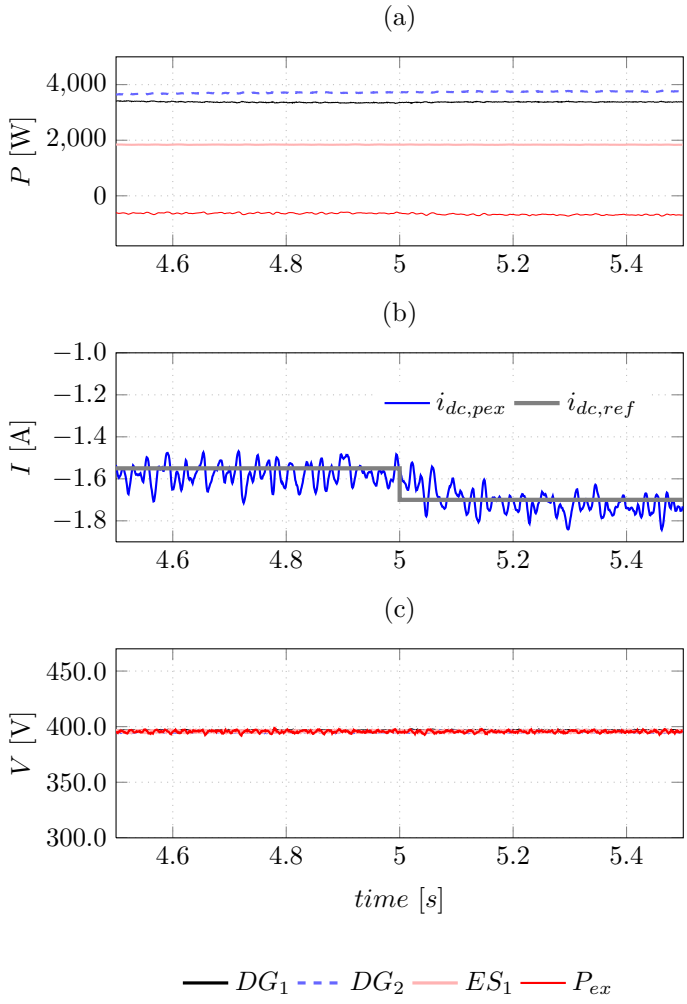

Figure 4.18: Power sharing between the DGs and the Pex at the DC side, case B.

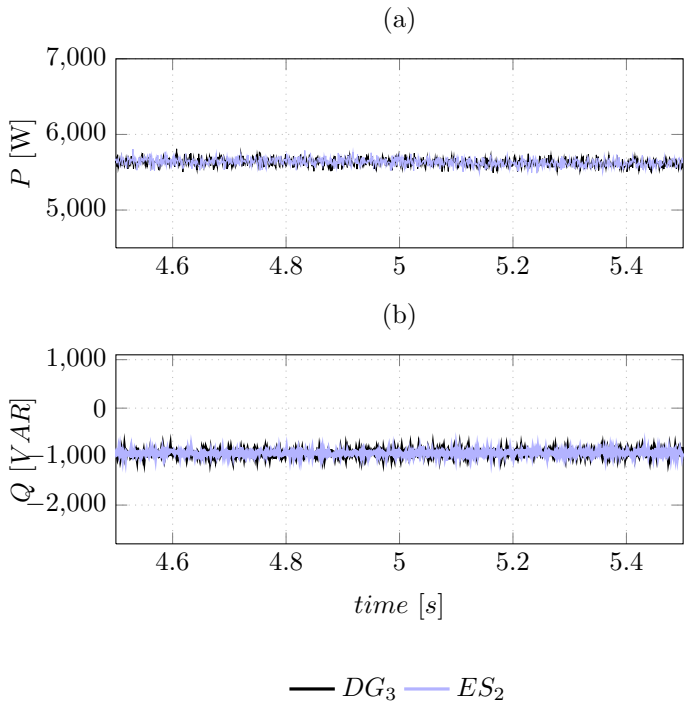

Figure 4.19: Power sharing between DGs at the AC side of the microgrid, case A.

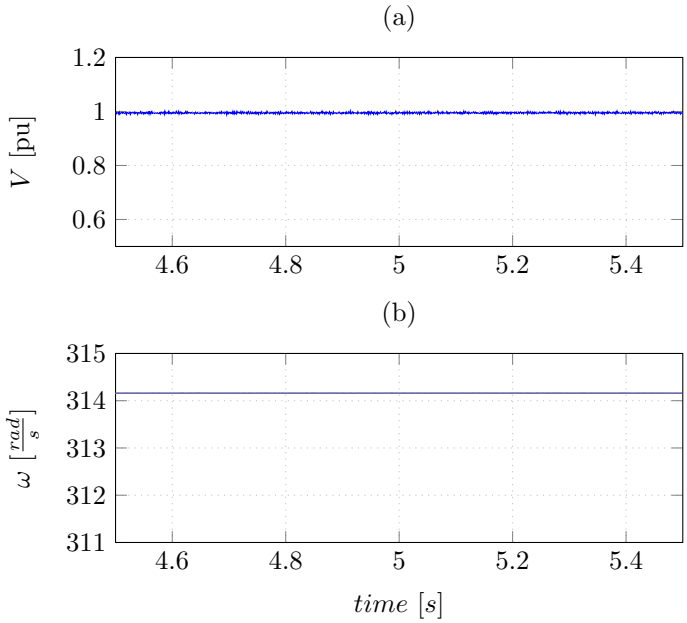

Figure 4.20: Voltage at pcc_8 and frequency speed at the terminals of DG_3 and ES_2.

DC bar and can not be removed. it is composed of a filter inductance with its respective resistance (6), E_s is the AC source connected (7). The linear amplifier limits the frequency range: in this case, the lowest frequency injected is 10 Hz.

Algorithm 5 Practical impedance algorithm.

1: **for** $f_p = f_{p,min}$ **to** $f_{sw}/2$ **do**
2: Inject the perturbation voltage v_p at f_p.
3: Capture time domain data i_m and v_m.
4: Use the Fourier transform, extract $\mathbf{I}_p, \mathbf{V}_p$.
5: Solve for $\mathbf{Z}_{dc} = \mathbf{V}_p/\mathbf{I}_p$.
6: **end for**

The magnitude of the experimental impedance and angle is shown in Fig. 4.23, where the shape of the magnitude is correlated with that predicted by the analytical methods. However, the angle obtained with the physical system does not match the analytical angle for low frequency values ($f < 20$Hz), and the change of the sign around 400Hz. This issue may be related to some noise problems of the measures at the low operation point used. Nonetheless, the experimental response and the analytical methods show the main behavior of the angle involves negative values, which is consistent with the theory used to obtain the impedance.

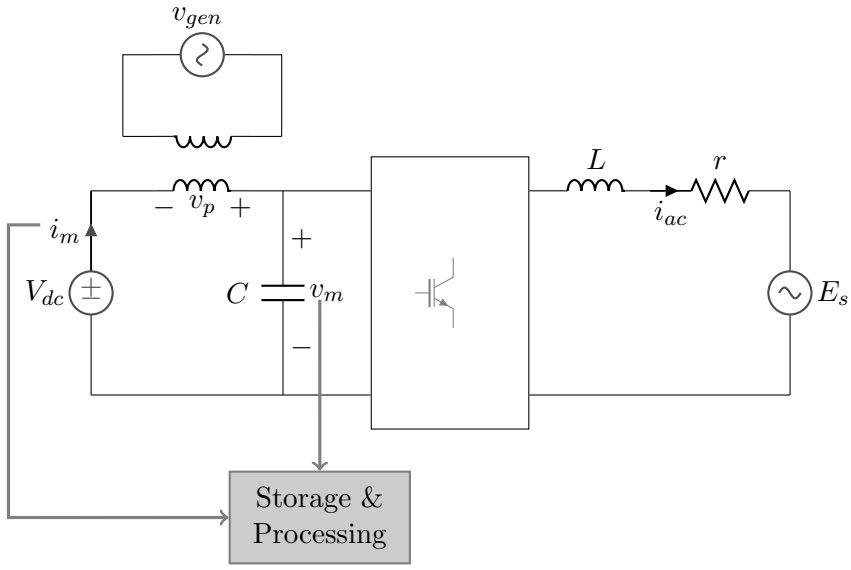

Figure 4.21: System configuration to obtain the impedance of the VSC.

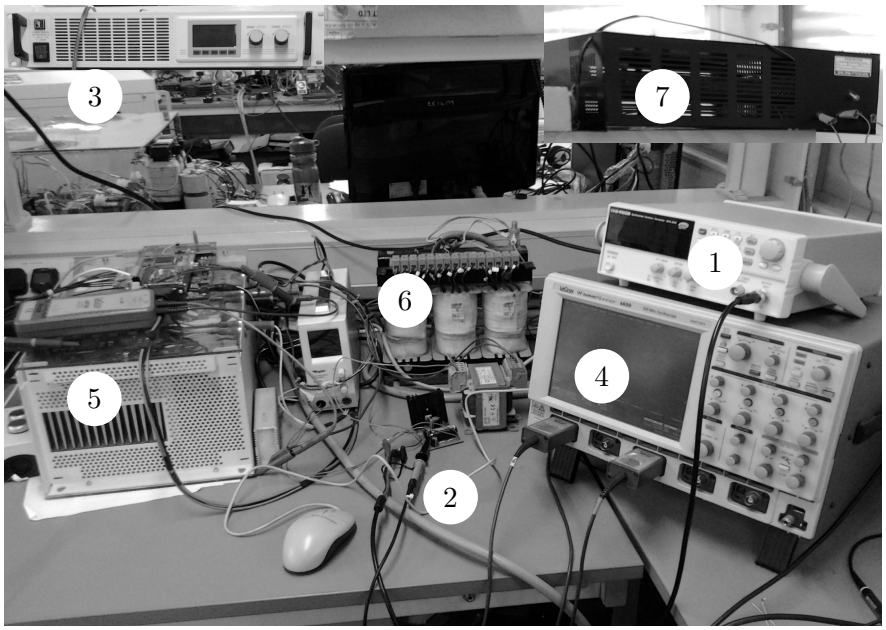

Figure 4.22: Experimental equipment used to obtain the impedance of the VSC system.

4.6 Final considerations about the stability test

In this section, the stability of the future interconnection of a DC microgrid and an AC system was assessed. The analysis was performed using Nyquist criteria with Thevenin and Norton equivalents. These equivalents were selected according to the behavior, and control strategies used by the converters at the distribution level of the microgrid.

As seen in Fig. 4.10 and Fig. 4.11 with margin criteria, this analysis predicts that the system is stabe when the AC system is coupled with the DC grid. Small disturbances were also considered.

The impedance representation methods applied and the stability study can be used with the passive filter design to improve the quality of the microgrid.

An advantage of this method is its practical application: it can be used as a black-box model for converters and microgrids, because manufacturers are unlikely to provide all information about the parameters of the devices. It is important to remark that the impedance of the microgrid depends on the operation point, its

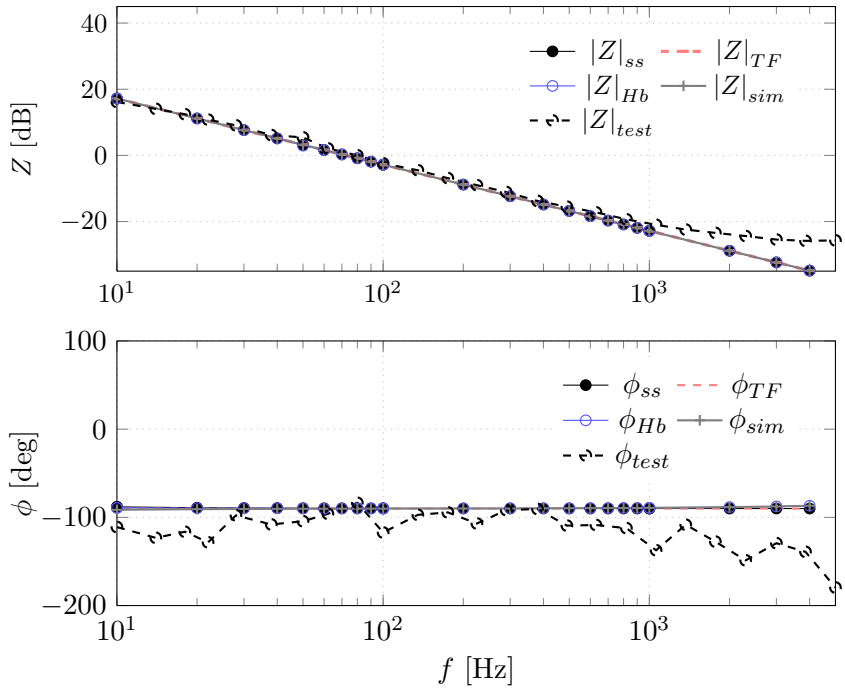

Figure 4.23: Impedance for the VSC system operating at $5\%P_n$, (ss) state space, (TF) TF approximations, (Hb) harmonic balance, (sim) simulation and ($test$) physical converter.

topology, and the coordination or settings at the moment of computation. With this method, it is not straightforward to identify the variable that affects the most the instability of the system. Indeed, this must be done at one node at a time.

Several questions still remains about the application of the AC impedance model with the positive and negative sequence or the synchronous reference frame. Indeed, if an impedance in abc is a time variable, then the results of these methods are inconsistent and PN does not provide accurate calculations.

The response of PN models of the AC microgrid is characterized by RL behavior. From the DC equivalent impedance of the microgrid, it can be concluded that an RL equivalent can be studied for slow frequencies (long term models). This issue is discussed in the next chapter.

Chapter 5

Long term model representation of the Pex and DC microgrid equivalent

This chapter describes a technique to obtain the microgrid Thevenin equivalent for long term modeling. This method uses estimation with semi-recursive algorithms based on the Kalman filter and recursive least squares. The stability of the system equivalent connected to the power exchanger was also determined.

In the previous chapter, it was shown that a problem arises when information about the parameters used in the full system is missing. The tools used to study the stability of this class of microgrid systems require an estimation of the grid equivalent impedance. The grid impedance estimation around an operation point can be used to define a space variable-parameter which in turn provides a qualitative or quantitative measure from the operation to the unstable boundary. This chapter describes an alternative approach to estimate grid impedance, which is based on the Kalman filter and the recursive least squares method. With these techniques, grid impedance is estimated using two neighbor operation points. Finally, the estimated values of the impedance of the DC microgrid (see Fig. 3.2) are used to study the long-term stability of a DC constant power load.

The stability of systems with CPLs was studied in [13, 14, 45, 77], using a Thevenin equivalent of the system (e.g. a microgrid) and the CPL model. These studies defined stable regions within the parameter space. However, an estimation of grid impedance is required to obtain this equivalent. Methods for estimating grid impedance are classified as intrusive or nonintrusive [78]. Impedance representation in the frequency domain was used in [10, 79]. This method has one

important disadvantage: it requires measurement of the frequency spectrum over a period of time such that voltage and current values can be obtained at steady state, for each value of the perturbation frequency within a test range. However, an on-line procedure is performed at each instant of time using samples of the measurable variables of the microgrid system. AC grid impedance has been estimated with the on-line method using the DG unit in [80–82]. A technique for harmonic impedance is proposed in [83]. In [78,84], impedance was estimated with an AC method involving two points of operation, without recursive algorithms, whereas a recursive technique was used in [85], which included the estimation of the source. However, this latter method uses complex variables that have to be precomputed by a fast Fourier transform or phasor notation. AC systems differ from the DC (the steady state in AC systems is a point in $\mathbb{R}^n$).
Recursive estimation techniques such as orthogonal projection, recursive least squares, and Kalman filtering [86, 87] can be used to estimate grid impedance. The advantage of this method is its discrete time model, Which is easy to implement in a digital signal processor. The aim is to obtain the impedance of the microgrid equivalent by a simple tool and to use this information to estimate regions of the stability in DC microgrids with CPLs.

5.1 Stability of the DC microgrid equivalent at the pcc of the constant power load model

An equivalent circuit of the DC microgrid has been obtained in this section and is presented in Fig. 5.1. The power exchanger device is assumed to be a constant power load (CPL). In the Thevenin equivalent shown in Fig. 5.2, the Pex is used instead of the current source [20,88], the current flowing into the CPL is called i_p, and the current i in this model is assumed to flow in the opposite direction. This equivalent can be used to find the stable operation region and the Hopf bifurcation points that can produce oscillations in the system [89, 90]. The non-linear model for the equivalent circuit is:

$$i_p = \frac{P}{v} \tag{5.1}$$

$$L\frac{d}{dt}i = -ri - v + V_s \tag{5.2}$$

$$C\frac{d}{dt}v = i - i_p \tag{5.3}$$

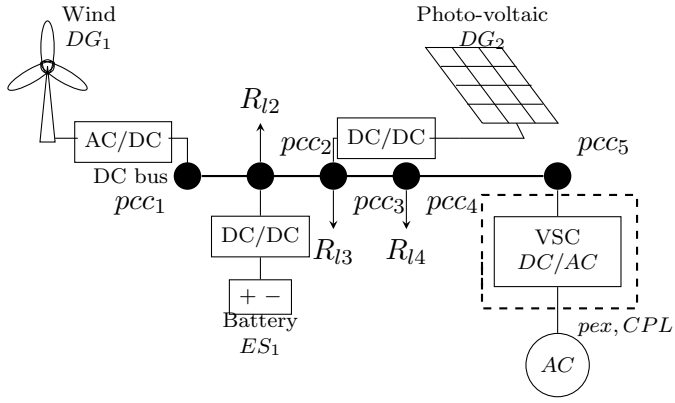

Figure 5.1: The DC microgrid used for the recursive equivalent estimation method.

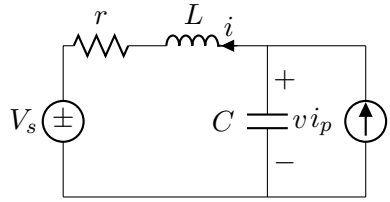

Figure 5.2: RLC equivalent grid circuit used for estimation.

The CPL can be represented by the small signal equation, where the incremental variables are defined as $\Delta v = -\Delta i \frac{v^2}{P}$, and the term of negative resistance is $r_n = -\frac{v^2}{P}$. The set of equations for the system is presented in a state space form in (5.4)-(5.5).

$$\frac{d}{dt}\Delta v = \frac{P}{Cv^2}\Delta v + \frac{\Delta i}{C} \tag{5.4}$$

$$\frac{d}{dt}\Delta i = -\frac{1}{L}\Delta v - \frac{r}{L}\Delta i + \frac{1}{L}\Delta V_s \tag{5.5}$$

5.1.1 Indirect method to analyze the boundary of stable regions

Boundary curves are first plotted from the eigenvalues of the state matrix A (5.6) [89, 91].

$$A = \begin{pmatrix} \frac{P}{Cv^2} & \frac{1}{C} \\ -\frac{1}{L} & -\frac{r}{L} \end{pmatrix} \tag{5.6}$$

The characteristic equation is described in (5.7).

$$\lambda^2 + \lambda\left(\frac{r}{L} - \frac{P}{Cv^2}\right) - \frac{Pr}{Cv^2L} + \frac{1}{LC} = 0 \tag{5.7}$$

According (5.7), the following criteria are required to identify the operation [13, 77], where (5.8) and (5.9) are the conditions and restrictions that give rise to eigenvalues of A with a real part equal to zero.

$$\frac{r}{L} - \frac{P}{Cv^2} = 0 \tag{5.8}$$

$$\frac{Pr}{Cv^2L} - \frac{1}{LC} < 0 \tag{5.9}$$

The curves for the critical values of r as a function of P and the restriction are obtained from (5.8) and (5.9) and described by (5.10) and (5.11), respectively.

$$r = L\frac{P}{Cv^2} \tag{5.10}$$

$$r < \frac{v^2}{P} \tag{5.11}$$

When the analyzed parameter is inductance, the resistance is assumed constant at a nominal value. The stability boundary for the variation of the inductance as function of the power is described by (5.12), and is obtained from (5.8). The criterion required to obtain imaginary poles in the system is (5.13), and is referred to as the restriction ($rest$). Thus, the system can reach the boundary if the relation in (5.13) is satisfied.

$$L = \frac{rCv^2}{P} \tag{5.12}$$

$$1 > \frac{Pr}{v^2} \tag{5.13}$$

The obtained stable and unstable regions with unity values are shown in Fig.5.3, where the combination of parameters $r-P$ and $L-P$ is presented. The shadowed areas describe the stable combinations of operations in the parameter space.

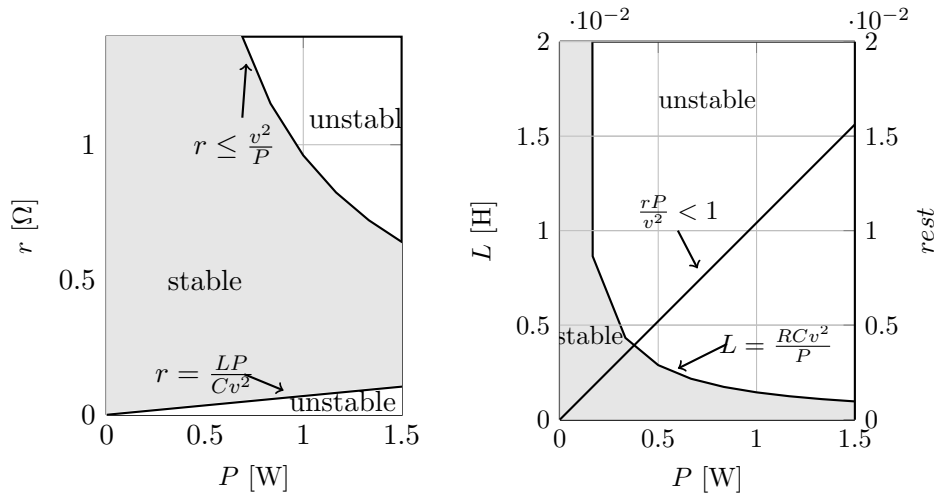

Figure 5.3: Stable regions of operation for the CPLs in a DC micro-grid.

5.2 Computation of grid impedance by current perturbation and recursive parameter estimation

Two recursive methods exist for estimating grid impedance. The first method involves two points of operation in the system that are used to eliminate the action of the voltage source, which can be seen as unknown and unmeasurable from the node that is under consideration. However, if a representative ideal source is required, then the action of the source is included in the estimation procedure (i.e. the source becomes an estimated variable). When the source is estimated, only one operation point is necessary in a recursive approach. For this work, the time domain representation of the system in Fig. 5.2 is described as:

$$v(t) = L(t)\frac{di(t)}{dt} + r(t)i(t) + v_s(t) \tag{5.14}$$

where L(t) and r(t) are assumed to be time dependent parameters of the equivalent grid impedance, and are constant around an operation point for a time interval. The current that flows from the converter to the system or from the system to the converter is $i(t)$, the voltage at the coupling point is $v(t)$ and the source voltage is $v_s(t)$. The capacitor C is the capacitor at the terminals of the PED, and the current controlled to study the dynamics is i_p.

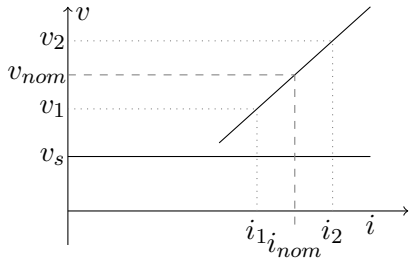

Figure 5.4: Operation points of the system.

5.2.1 Estimation method

Estimation of grid impedance without using the source

The technique used to avoid the computation of the source is based on the method of two operation points presented by [84], where the system used was an AC circuit. The two states of operation are defined by the variation of one of the states of the system. This variation can be called a disturbance around the nominal point. In this work, a semi-recursive estimation method involving the Kalman filter and recursive least squares is used, and the time domain is studied for the two states of operation. This technique requires some preparatory steps. First, for a short time at the beginning, a small window of data is stored in the memory, and following initialization, the recursive algorithm starts to estimate the impedance. Initialization may occur following the acquisition of a defined number of samples after the start of data storage. Then, a window of updated samples is kept during the application of the algorithm, to enable both its use on-line and its operation with a PED.

The method works as follows. Starting with (5.14), the parameters $r(t)$ and $L(t)$ are estimated. However, the source voltage must be eliminated. Assuming linearity around the nominal operation point, it is possible to obtain the equations for the points under test (5.15)-(5.16). The states of operation are close to the operation point. This is represented in Fig. 5.4, where v_{nom} and i_{nom} are the operation voltage and current, respectively.

$$v_1(t) = L(t)\frac{di_1(t)}{dt} + r(t)i_1(t) + v_s(t) \tag{5.15}$$

$$v_2(t) = L(t)\frac{di_2(t)}{dt} + r(t)i_2(t) + v_s(t) \tag{5.16}$$

Assuming that there is no change in the parameters, the system is reduced to:

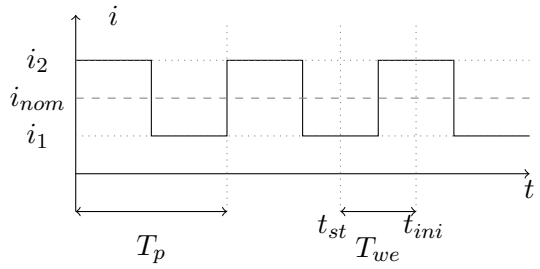

Figure 5.5: Reference current to estimate grid impedance.

$$\Delta v(t) = L(t)\frac{d}{dt}\Delta i(t) + r(t)\Delta i(t) \tag{5.17}$$

where $\Delta v(t) = v_2(t) - v_1(t)$, and $\Delta i(t) = i_2(t) - i_1(t)$. The system has now been reduced to two measurable variables $v(t)$ and $i(t)$, and two estimable parameters $L(t) = L$ and $r(t) = r$. Although these parameters can vary with time, they are assumed to stay constant around a period τ. This period is used to obtain an accurate estimation of the parameters. The recursive method will include the new value of the parameters, despite their potential variation. The characteristic of the signal used as a reference of the current injected is presented in Fig. 5.5. The square wave has a period T_p, and a small maximum gain to keep the operation around the working value. The maximum value reaches the desired current i_2, and when the current reaches its minimum value i_1, the method starts to store data at the instant called t_{st} (required for semi-recursive estimation). The estimator uses a window with a fixed time interval defined as $T_{we} = \frac{T_p}{2}$, where the differences of the voltage and the current can be obtained. The estimator starts its operation at the time t_{ini}.

Then, first a discretization of the model (5.17) is obtained. The equation is reorganized in (5.18)-(5.19).

$$\frac{d}{dt}\Delta i = -\frac{r}{L}\Delta i + \frac{1}{L}\Delta v \tag{5.18}$$

$$y = \Delta i \tag{5.19}$$

Using the discrete form of a state space representation the system is:

$$\Delta i_k = \phi\Delta i_{k-1} + \gamma\Delta v_{k-1} \tag{5.20}$$

$$y_k = \Delta i_k \tag{5.21}$$

where ϕ is the discrete state matrix, and γ is the input gain matrix for discrete systems, in this case the dimension is 1×1.
The final values of these parameters are:

$$\phi = 1 - \frac{r}{L}h \tag{5.22}$$

$$\gamma = \frac{h}{L} \tag{5.23}$$

The parameter h is the sample time used to discretize the system. Now the parameters can be obtained by the recursive technique. Finally, to find the real parameters it is necessary to solve the equations (5.22) and (5.23) for r and L.

5.3 The Kalman filter

The Kalman filter is used to estimate the state x_k in a stochastic model of finite dimension. The system is defined by (5.24), (5.25) and (5.26), where A is the system matrix, B is the control matrix, and C is the output matrix. The noises in the system are v_{1k} and v_{2k}, with zero mean. If the noise is not used, the model describes a deterministic system [86, 92].
The estimation of the process can be considered as feedback control, where the filter estimates the state and feedback is subsequently obtained from the measures (plus the noise). The equations describing the Kalman filter can be divided into two groups, one that updates with time and another that updates over the measure [93].
The signal v_{1k} is the process noise and v_{2k} is the noise of the measure. These signals are white noise with zero mean and are not correlated.

$$x_{k+1} = Ax_k + Bu_k + v_{1k} \tag{5.24}$$

$$y_k = Cx_k + v_{2k}; \qquad k \geq k_0 \tag{5.25}$$

where x_{k0} is a random variable with mean $\bar{x}_0$ and variance Σ_0. For the noise the second expectation is:

$$E\left\{ \begin{bmatrix} v_{1k} \\ v_{2k} \end{bmatrix} \begin{bmatrix} v_{1k}^T & v_{2k}^T \end{bmatrix} \right\} = \begin{pmatrix} Q & S \\ S^T & R \end{pmatrix} \tag{5.26}$$

where E is the statistical expectation. The variance matrices Q and R can be assumed constant and the matrix of covariance S can be zero. The filter is based on the following interpretations: 1) if the noise is Gaussian, the filter presents the state estimation by minimum variance; and 2) if the first assumption is removed,

the filter obtains the state estimation by linear minimum variance.

The Kalman filter is based on an equation that estimates the following state $\hat{x}_{k+1}$ from a lineal combination with the preceding state $\hat{x}_k$, a weight of the difference between the actual value y_k, the prediction of the output $C\hat{x}_k$, and the relation with the input Bu_k. The system is described in (5.27) and (5.28).

$$\begin{aligned} \hat{x}_{k+1} &= A\hat{x}_k + K_k[y_k - C\hat{x}_k] + Bu_k & (5.27) \\ \hat{x}_{k0} &= \bar{x}_0 & (5.28) \end{aligned}$$

where K_k is the Kalman's gain obtained in (5.29) at the instant k.

$$K_k = [A\Sigma_k C^T + S][C\Sigma_k C^T + R]^{-1} \quad (5.29)$$

The error of the state estimation can be obtained from (5.30).

$$e = \hat{x}_k - x_k \quad (5.30)$$

Σ is the state error covariance given the observations y_k, and is defined in (5.31).

$$\Sigma_k \triangleq E\{[\hat{x}_k - x_k][\hat{x}_k - x_k]^T | y_{k-1}, ..., y_{k0}\} \quad (5.31)$$

Σ_k satisfies Riccati's equations (5.31) and (5.32).

$$\begin{aligned} \Sigma_k &= A\Sigma_k A^T + Q - K_k[C\Sigma_k C^T + R]K_k^T & (5.32) \\ \Sigma_{k0} &= \Sigma_0 & (5.33) \end{aligned}$$

5.4 Parameter estimation for the application of a recursive method

The process model for parameter estimation is described as:

$$\theta_k = \theta_{k-1} + \eta_{1k} \quad (5.34)$$

$$y_k = \Phi^T \theta_k + \eta_{2k} \quad (5.35)$$

where θ_k is the vector of the variables to be estimated at the instant k, Φ is the matrix containing the measured samples, y_k is the output, and η_1 and η_2 are the process noise and the measure noise, respectively. In this case, application of the Kalman filter requires an the ARX model representation (5.36), in which the vector of input and output samples is Φ, the vector of parameters is θ and

the output of the system is y. The values a_j for j=1,...,m are the parameters of the characteristic polynomial in differences or Z domain for deterministic systems. The values b_j form the numerator of the transfer function in the Z domain. Finally e_k is the noise of the measure and the process.

$$y_k + a_1 y_{k-1} + ... + a_m y_{k-m} = b_0 u_k + b_1 u_{k-1} + ... + b_m u_{k-m} + e_k \tag{5.36}$$

The equivalent grid has a system with order one for the differences equation (5.36) compared with (5.20). The parameter b_0 is equal to zero. The model is then reduced to:

$$y_k + a_1 y_{k-1} = b_1 u_{k-1} + e_k \tag{5.37}$$

The vectors Φ and θ for the case of square wave injection are:

$$\Phi = \begin{bmatrix} y_{k-1} \\ u_{k-1} \end{bmatrix} = \begin{bmatrix} \Delta i_{k-1} \\ \Delta v_{k-1} \end{bmatrix} \tag{5.38}$$

$$\theta = \begin{bmatrix} a_1 \\ b_1 \end{bmatrix} = \begin{bmatrix} \phi \\ \gamma \end{bmatrix} \tag{5.39}$$

5.4.1 Structure of the Kalman filter

In this case, the filter takes the following values in some of its matrices: $A = I$, where I is the identity matrix, $B = 0$, $C = \Phi_k$, $Q \geq 0$ and $R > 0$, and the parameter vector is defined as $\theta_k \triangleq x_k$ [92]. Assuming that the initial state is not correlated with errors and has finite variance, the two sets of equations that define the filter are listed in (5.40) to (5.45), with (5.40) and (5.41) describing the the time updating component and (5.42) to (5.45) describing the measure updating component.

$$\hat{\theta}_{k|k-1} = \hat{\theta}_{k-1} \tag{5.40}$$

$$\Sigma_{k|k-1} = \Sigma_{k-1} + Q_{k-1} \tag{5.41}$$

$$K_k = \Sigma_{k|k-1}\Phi\left[\Phi^T\Sigma_{k|k-1}\Phi + R_k\right]^{-1} \tag{5.42}$$

$$\Sigma_k = (I - K_k\Phi^T)\Sigma_{k|k-1} \tag{5.43}$$

$$\xi_k = y_k - \Phi^T\hat{\theta}_{k|k-1} \tag{5.44}$$

$$\hat{\theta}_k = \hat{\theta}_{k|k-1} + K_k\xi_k \tag{5.45}$$

The value $\hat{\theta}_{k\|k-1}$ is the mean estimation of θ_k given the observations $y_1, ..., y_{k-1}$, and ξ is the output error. Finally, K_k is the Kalman‘s gain matrix.

5.5 Recursive least squares estimation

Here, recursive least squares estimation (RLSE) is described as a special case of the Kalman filter, where several considerations are taken into account to describe it.
From the equations of the Kalman filter (5.24) and (5.25) it is assumed that $A = I$, $B = 0$, $Q = 0$, $R = 1$, $v_{1k} = 0$, $C = \Phi^T$. This defines $\theta_k \triangleq x_k$, the special case in which the Kalman filter is obtained. The RLSE algorithm is thus described by (5.46) and (5.47).

$$\theta_{k+1} = \theta_k \tag{5.46}$$

$$y_k = \Phi^T \theta_k + v_{2k} \tag{5.47}$$

The following equations (5.48)-(5.50) describe the RLSE method, where $\hat{\theta}$ represents the estimated state.

$$K_{k|k-1} = \Sigma_k \Phi [1 + \Phi^T \Sigma_{k-1} \Phi]^{-1} \tag{5.48}$$

$$\Sigma_{k|k-1} = \left[I - K_k \Phi^T \right] \Sigma_k \tag{5.49}$$

$$\hat{\theta}_{k|k-1} = \hat{\theta}_{k-1} + K_k \left[y_k - \Phi^T \hat{\theta}_{k-1} \right] \tag{5.50}$$

The initialization is $\hat{\theta}_0 = 0$ and $\Sigma_0 = \alpha I$, where α is a large scalar and greater than zero.

Algorithm 6 summarizes the application of the methodology described in this approach. In order to apply the technique some stages have been defined. First, at the start instant, for a short time, a small window of data is stored in the memory and after an initialization condition, the recursive algorithm starts the equivalent microgrid impedance estimation. The initialization flag can be a defined number of samples after the data start to be stored. Then a window of updated samples is kept during the algorithm application in order to extend its use on-line and to operate with a PED. For the equivalent impedance estimation (5.35) is a homologous equation to (5.20) without noise. Therefore, the Kalman filter or the RLSE can be applied as described in their subsections.

5.6 Results for the estimation of the Thevenin equivalent

The two methods for estimating impedance were tested in the two different conditions routlined above; the DC microgrid (case 1) and a proof of concept (case

Algorithm 6 Algorithm for recursive equivalent microgrid impedance.

1: Select a method between Kalman filter or RLSE.
2: At the node of the CPL generate the perturbation.
3: **for** $t = 0$ **to** $\frac{T_p}{2}$ **do**
4: Inject the perturbation current, At each sampling instant store i and v.
5: **end for**
6: Start the computation of Δi_k and Δv_k with the samples stored. Continue storing the new samples for i and v.
7: Set the system samples as in (5.38) and (5.39). They can form (5.35).
8: Call the method {Kalman/RLSE}.
9: Calculate equivalent microgrid parameters solving for r and L in (5.22), and (5.23).
10: **if** stop criteria reached **then**
11: Compute the equivalent impedance.
12: Obtain the large signal parameters space r-P and L-P. Locate the operation point.
13: Analyze the stability.
14: **end if**

2). The tests are based on the circuit described in Fig. 5.2. The first system is the microgrid with the Pex as the device under test (Fig. 3.2).

To obtain the two operation points a square wave current was added to the average current consumed by the converter coupled to the microgrid in cases A (low inductor value) and B (large inductor value). The main structure of the equivalent system is shown in Fig. 5.2. The current source is replaced with a programmable load in the proof of concept case. The periods used for the estimation procedure in both cases are shown in Table 5.1, where f_s is the sampled frequency and $T_s = 1/f_s$ is the sample period. In this case, a complete switched model has been used for the power electronic converters.

During the application of the RLSE method the estimation error of the output is reduced by correct initialization of the matrix Σ_0. The initialization of the state error covariance matrix is $\Sigma_0 = \alpha I$, where I is the identity matrix and $\alpha = 10^4$. It was periodically reinitialized to ensure the quick determination of and operation around the true parameters.

Matrix Q in the model is related to the states. In this case, the parameters to be estimated are ϕ and γ, and they are elements of θ. Therefore, according to the order one discrete system (5.20), the system is stable if the parameter ϕ

Table 5.1: Periods for the estimation procedure.

Case	f_s	T_p	T_{we}
case 1.A and 1.B	1kHz	$100T_s$	$50T_s$
case 2	1kHz	$100T_s$	$50T_s$

remains inside the unitary circle. Hence, a standard deviation for the parameters $\sigma_{\eta_1} \approx 1 \times 10^{-3}$ has been used. Using σ_{η_1} the matrix $Q = \sigma_{\eta_1}^2 I$ is obtained. Matrix R is related to the measured variable Δi, which is derived from a previously sampled current (i) as defined in Fig. 3. This variable has been filtered with a moving average filter with order 16, to obtain i_f. The resulting current is subsequently computed as $i_r = i - i_f$. Finally, the standard deviation of i_r (σ_{η_2}) has been obtained using $R = \sigma_{\eta_2}^2$. The value for both the microgrid (case 1) and the proof of concept (case 2) is $\sigma_{\eta_2} = 5 \times 10^{-2}$ A.

The execution time of the Kalman filter is 48.637 μs and the RLSE is 47.504 μs at each iteration. Execution time was measured in a matlab script with an intel core i5 2.4 GHz processor.

5.6.1 Equivalent DC-microgrid

The DC side of the microgrid is shown in Fig. 5.1. Table 5.2 shows the coordination and the operation point of the devices in the DC microgrid. The DC voltage is controlled at 400 V.

Table 5.2: Operation point of DC microgrid elements.

Control type	Device	Power
Voltage	DG_1	3.8 kW
Current	DG_2	3.525 kW
Current	ES_1	1.9 kW
Current	Pex	0.6 kW
-	R_{l2}	2.5 kW
-	R_{l3}	5 kW
-	R_{l4}	1.125 kW

The estimation of the equivalent circuit of the microgrid, described in section 3.2, is presented in Fig. 5.6 and Fig. 5.7, where KF is the results for the Kalman filter and RLSE is the estimation obtained by the recursive least squares method. This equivalent is obtained at the pcc_5 node, where the P_{ex} device is characterized

by long-term CPL behavior, and the power extracted from the DC microgrid is 600W. The reference of the consumed current is a square wave with $\Delta i_{max} = 1$ A. The estimation periods used for the test are shown in Table 5.1. The test uses only a small amount of the data stored to estimate the parameters of the Thevenin equivalent. The estimation window is $T_{we} = 50T_s$.

Fig. 5.6 shows the results of the test for the case 1.A in which the low inductor L_{fvsc} is coupled to the Pex. The resistance and inductor estimated with the KF and RLSE method can be seen. The average strength of the resistor, r, is 6.6 Ω, and the inductor is around 0.034 H. The settling time of the KF method is faster than that of the RLSE (Fig. 5.6.b and Fig. 5.6.c). Indeed, in Fig. 5.6.b, the RLSE takes around 60 samples to reach the mean value of the estimated r, whereas in Fig. 5.6.c the RLSE takes around 100 samples to reach mean value of the estimated L.

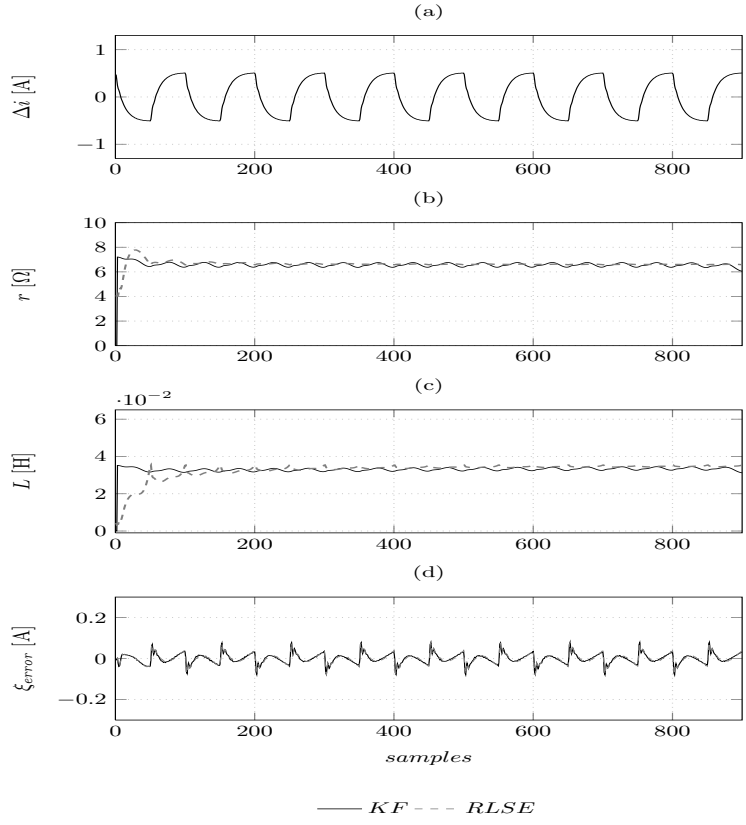

Figure 5.6: Case 1.A estimation for the DC microgrid with the Kalman filter (KF) and recursive least squares (RLSE). Current difference (a), estimated resistance (b), estimated inductor (c), estimation error (d).

Figure 5.7 shows the results of the test for case 1.B, in which the larger inductor L_{fvsc} is coupled to the Pex. This case shows ripples varying around 6 Ω, which were produced for the ripple in Δi. The estimated inductor is around 60 mH, which is an expected result because P_{ex} is connected to the DC grid through this filter inductor in Fig. 5.7. The settling time of the KF method is faster than that of the RLSE (Fig. 5.7.b and Fig. 5.7.c), as was shown for case 1.A. Indeed, in Fig. 5.7.b the RLSE takes around 100 samples to reach the mean value of the resistance. Again in Fig. 5.7.c the RLSE takes around 100 samples to reach mean value of the inductor.

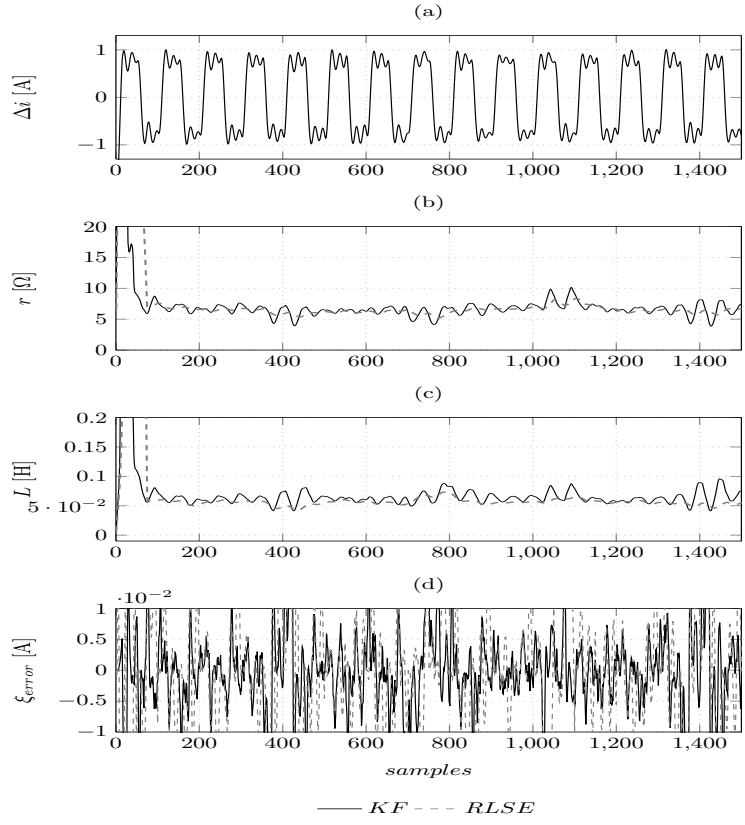

Figure 5.7: Case 1.B estimation for the DC microgrid with the Kalman filter (KF) and recursive least squares (RLSE). Current difference (a), estimated resistance (b), estimated inductor (c), estimation error (d).

Comparison of the estimation procedure

The impedance obtained by the Kalman filter and the recursive least squares method is validated by current injection perturbation [10] (frequency scanning procedure). The frequency response of the recursive estimated impedance and that of the network analyzer impedance are compared in Fig. 5.8.

For case 1.A, the magnitude and phase determined by the scanning method ($Z\angle\phi_{freqscA}$) and the recursive method ($Z\angle\phi_{KFA}$) are equal at low frequencies (10 Hz). This observation validates the expected behavior defined in this chapter. It is important to remark that the condition studied involves a low inductive parameter coupled to the Pex.

Similarly, in case 1.B (Fig. 5.8) the magnitude and angle of the recursive method ($Z\angle\phi_{KFB}$) and the scanning procedure ($Z\angle\phi_{freqscB}$) are equal at low frequencies (10 Hz). In this case, similar results are also obtained at high frequencies *i.e.* above 100 Hz.

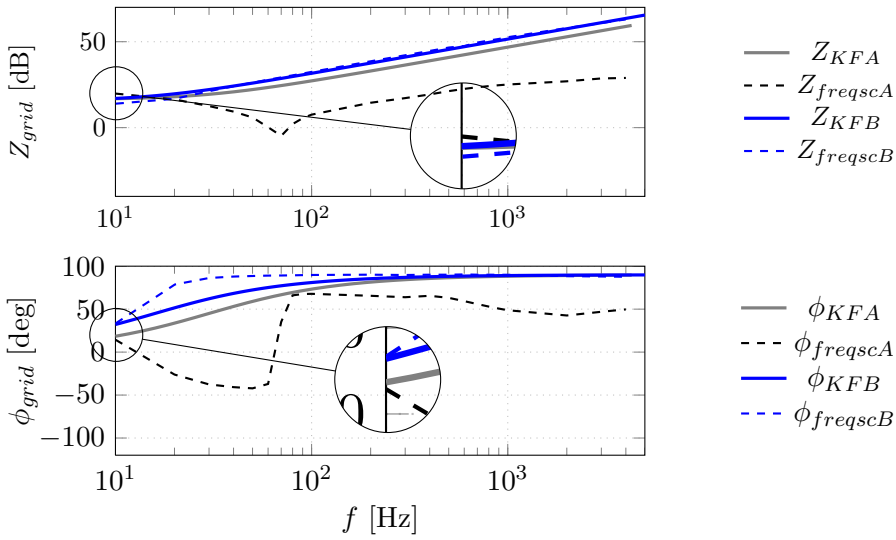

Figure 5.8: Comparison of microgrid impedance, magnitude and phase frequency responses. $Z\angle\phi_{KFi}$ is the recursive impedance, and $Z\angle\phi_{freqsci}$ is the parallel current perturbation impedance, where $i \in \{A, B\}$.

5.6.2 Proof of concept

An experimental circuit was used to validate the findings of case B in the laboratory (*i.e.* proof of the concept). A physical system such as that shown in Fig. 5.2 was constructed to verify the estimation of impedance in a real system. The system is composed of a DC source connected to the resistance, an inductor, a capacitor, and a commercially available electronic load EA-EL9080-200, which has a maximum voltage of 80 V and a maximum current of 200 A. The parameters used in the circuit are as follows: a resistance $r = 0.3\ \Omega$, an inductor $L = 1.5$ mH, a voltage source $V_s = 15$ V, the current is set as I_{nom} and consumes -1.5 A, the capacitor $C = 3.3$ mF, and the perturbation current is i_{square} with an amplitude of 0.2 A. The results of this estimation test are shown in Fig. 5.9. The Δi takes values within the range of $\pm$ 0.4 A. From the estimation, the ripple of the resistance and the inductor can be seen at every zero crossing of

Δi. Furthermore, the estimated resistance is close to 0.3 Ω, and differs slightly from the expected real parameter estimated with the RLSE. Figure 5.9 shows that the estimated inductor stays inside a boundary neighborhood of the true value in both methods. Additionally, the maximum error of the estimation (ξ) is 10 mA. Satisfactory results were thus obtained with this test, because the estimation error in percentage with respect to the perturbation signal is less than 2.5%.

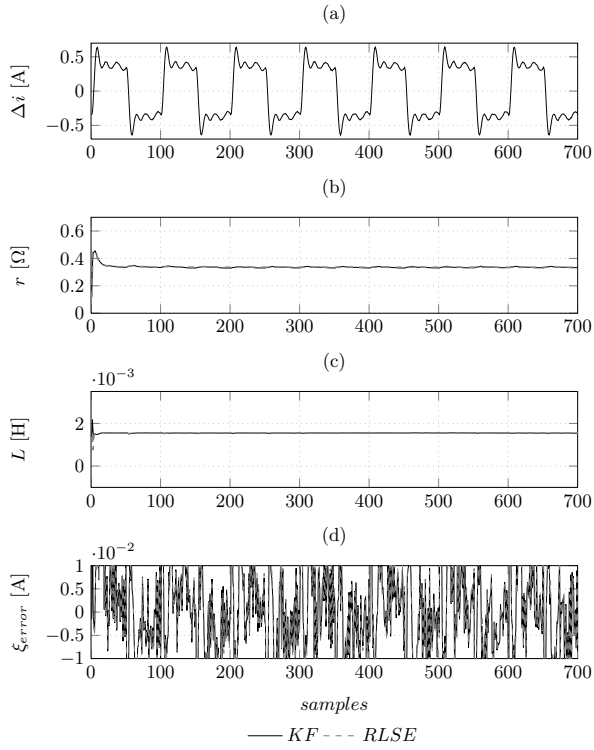

Figure 5.9: Experimental results with the Kalman filter (KF) and rescursive least squares (RLSE). Current difference (a), estimated resistance (b), estimated inductor (c), estimation error (d).

5.6.3 Stability regions of the estimated equivalents

Regions of the DC microgrid

The stable regions of the DC microgrid equivalent for cases 1.A and 1.B and the P_{ex} converter are shown in Fig. 5.10 and Fig. 5.11, respectively. A zoom of

the data obtained for each figure is shown to the right. This amplified view is presented by a dashed rectangle. The spaces $r - P$ and $L - P$ are used to analyze the stability of the generated system. The point of operation with the error ripple presented in the estimation, as well as the unstable area are shown. The system operates outside the unstable region in both cases. For case 1.A $r = 6.6\ \Omega$ and $L = 34$ mH were chosen to represent the equivalent impedance. The equivalent impedance for case 1.B is represented by $r = 6.0\ \Omega$ and $L = 60$ mH.

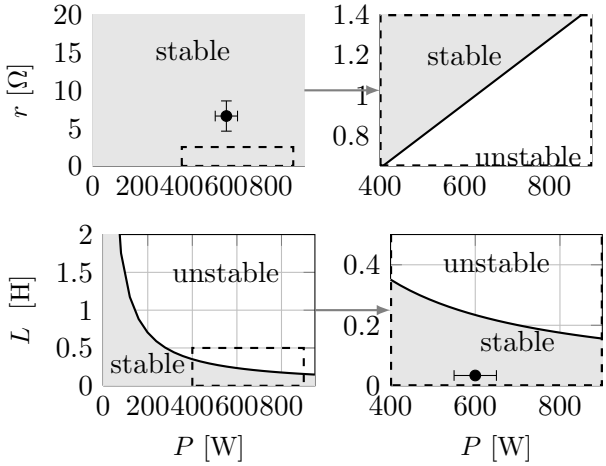

Figure 5.10: Stable regions of the DC microgrid in case 1.A.

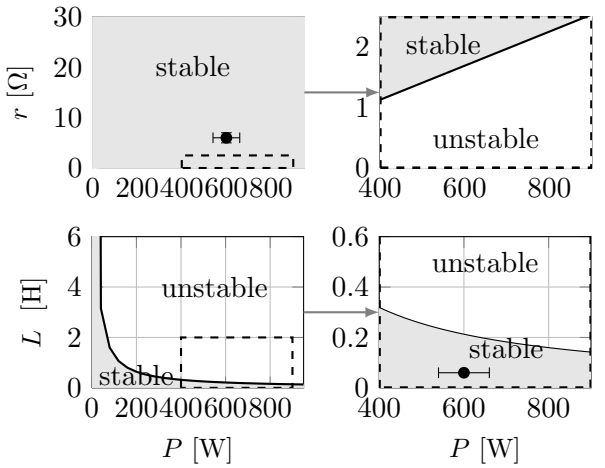

Figure 5.11: Stable regions of the DC microgrid in case 1.B.

Regions of the experimental system

The experimental system is shown in Fig. 5.12, where it can be seen that the operation point is located far from the unstable region in the parameter space.

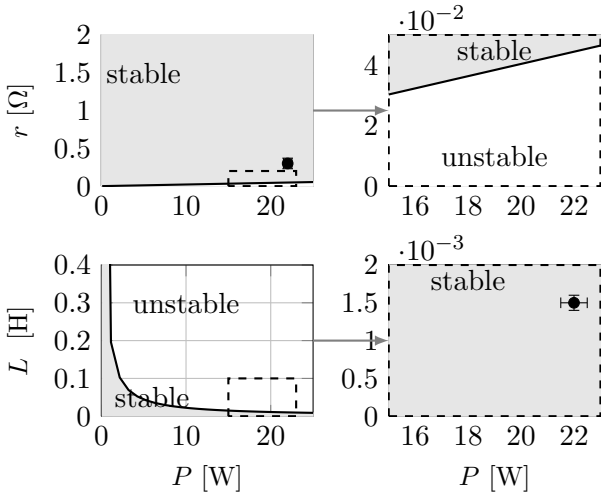

Figure 5.12: Stable regions of the experimental system.

5.6.4 Estimation of the $r-L$ equivalent of the DC microgrid under different operation points

The objective of this section is to describe how the behavior of the estimation method changes with alterations in the power shared in the microgrid. Changes to the operation point are involve the power steps consumed by the Pex and steps in ES. ES changes its operation from power source (discharging) to charging behavior, at which stage ES is considered a load in the DC microgrid. Finally, one special test has been carried out to determine the estimation of the equivalent under a trip of the energy storage system of the microgrid.

The coordination of the DGs involves a master/slave technique [25,43]. Under the chosen configuration of the microgrid. DG_1 is the master and maintains the voltage of the DC microgrid, whereas DG_2, ES_1 and Pex are the slaves and inject or consume power according to the reference of a centralized power management. The power sharing measurements are shown in Fig. 5.13a, and the voltage at the terminals of each device is shown in Fig. 5.13b. The first part of the estimation is characterized by three step changes in the power consumed by the Pex, at $t =\in \{5, 20, 40\}$ s. At $t = 60$ s ES_1 changes its operation from source to load,

emulating a state of charge, and a step change in the power consumed by ES_1 then occurs at 80 s. At 100 s, ES_1 disconnect from the DC microgrid.

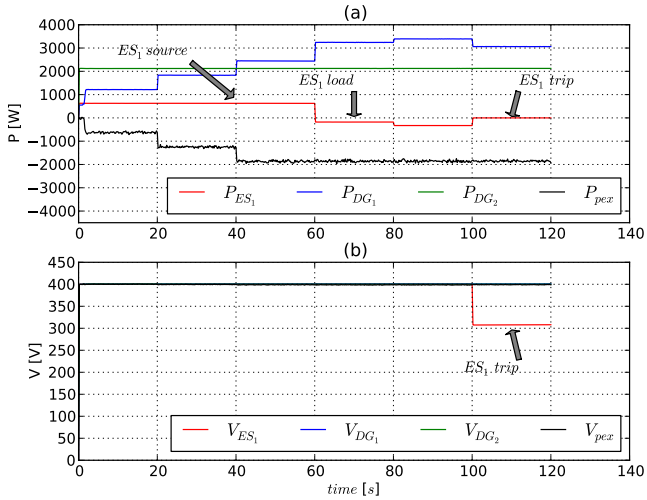

Figure 5.13: Power sharing of the *DGs* with a trip of ES at 100 s (a). Voltage measured at the terminals of each *DG* (b).

The estimated equivalent impedance is shown in Fig. 5.14. Figure 5.14a shows the estimated r, and reveals the presence of some spikes during the step changes in the power shared by the DGs. The average value of r increases following the disconnection of ES_1 from the grid. Figure 5.14b shows the estimated L, and reveals the mean value of changes of this parameter after each step. In the KF method, the value of the inductor increases around two times its previous value after the disconnection of ES_1. The inductor filter at the DC side of the Pex is $L_{fvsc} = 1.4$ mH and is twice the value of the inductor of case A. The Pex voltage and current in per unit are shown in Fig. 5.14c.

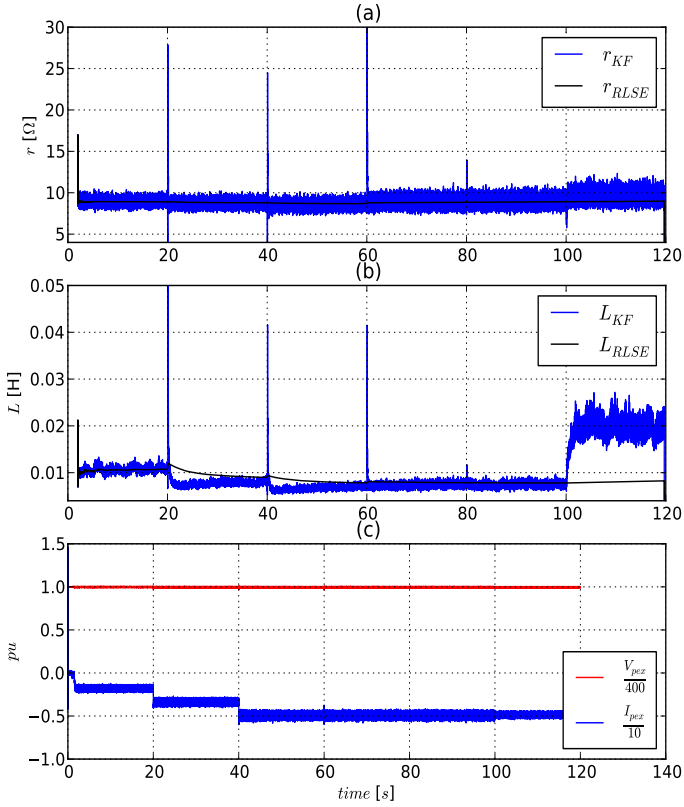

Figure 5.14: $r - L$ estimation. Estimation of the resistance (a), estimation of the equivalent inductor (b), Voltage and current at node pcc_5 (c).

The average values of the equivalent resistance and inductor in the KF and RLSE methods are presented as a function of the power changes in the DC microgrid (Fig. 5.15). $P_{changes} = 1$ represents the first 20 s, $P_{changes} = k$ with $k \in 1, 2, ..., 6$ is the average for the range of time [20(k-1)-20(k)] s. The KF estimation method is more sensitive than the RLSE method to power changes in the microgrid (Fig. 5.15).

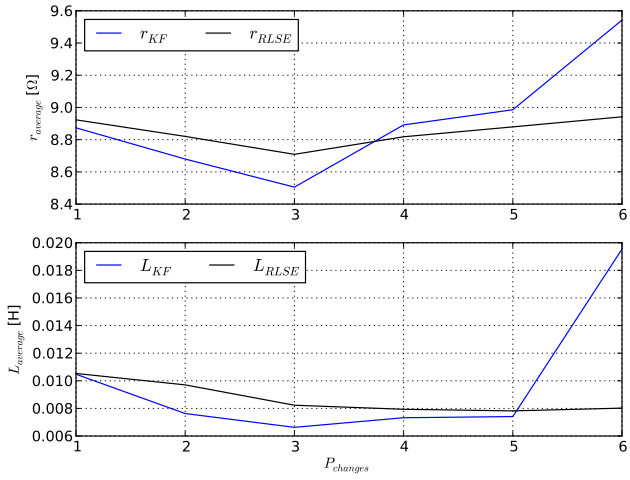

Figure 5.15: $r - L$ average estimation values as a function of the power changes in the DC microgrid. Average equivalent resistance (a), average equivalent inductor (b).

Figure 5.16a shows the estimation error for the output of the system with the KF method and Fig. 5.16b shows the measured Δi and the estimated signal $\Delta\hat{i}$. Three zoomed-in sections of the estimated signal are shown in Fig. 5.17. The regions shown correspond to (a) the initial part before the first power step of Pex (Fig. 5.17a); Fig. 5.17b shows the estimation at the change of operation of ES (*i.e.* from source to load in the DC microgrid); and Fig. 5.17c shows the time interval after the disconnection of ES_1. The estimated signal, $\Delta\hat{i}$, resembles closely the dynamic of the current Δi.

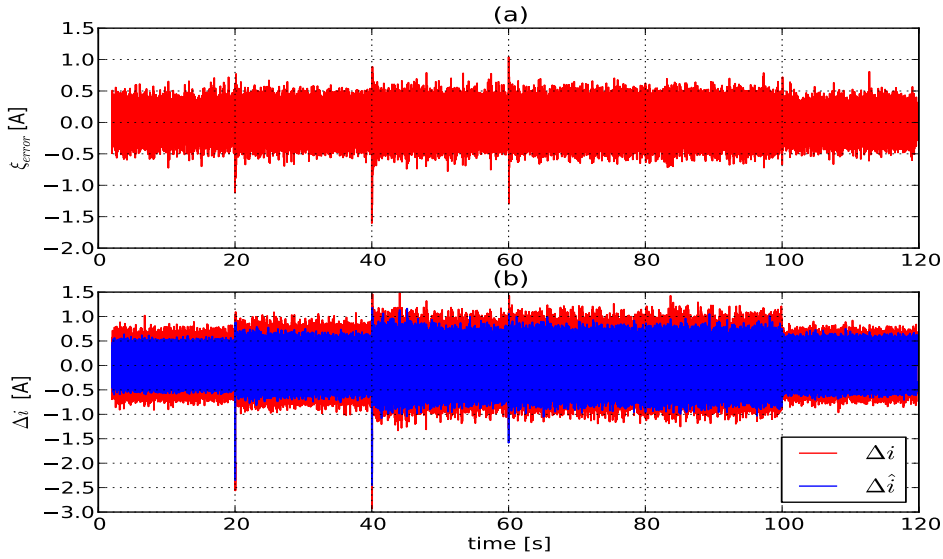

Figure 5.16: Estimation signals with the KF method. Error of the estimated Δi (a). Measured Δi and estimated $\Delta \hat{i}$ (b).

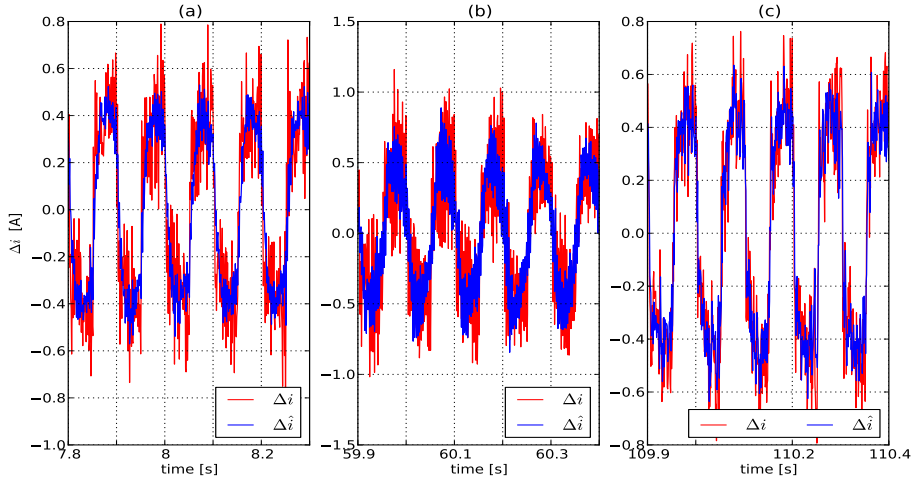

Figure 5.17: Zoom of the KF estimation of Δi. Time segment $7.8 < t < 8.3$ s (a). Time segment $59.9 < t < 60.4$ s (b). Time segment $109.9 < t < 110.4$ s (c).

Figure 5.18a shows the estimation error for the output of the system with the KF method and Fig. 5.18b, shows the measured Δi and the estimated signal $\Delta\hat{i}$. Three zoomed-in sections of the estimated signal are shown in Fig. 5.19.

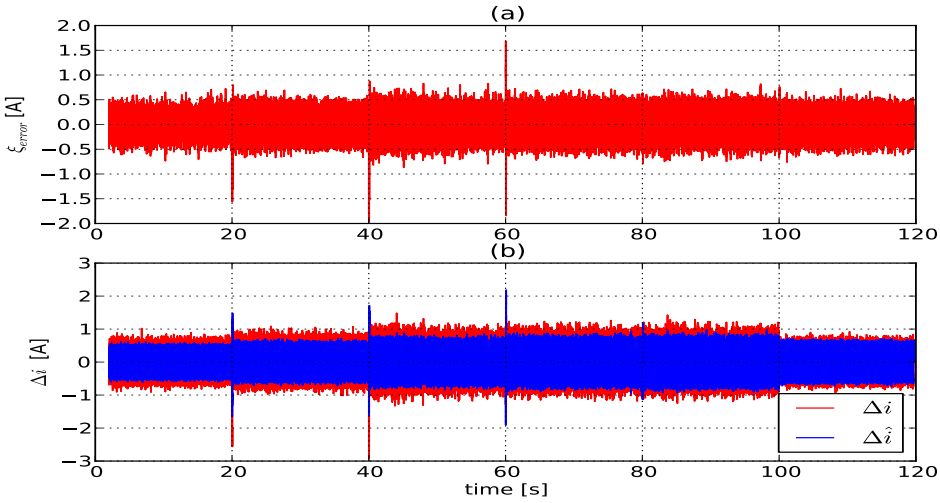

Figure 5.18: Estimation signals with the RLSE method. Error of the estimated Δi (a). Measured Δi and estimated $\Delta\hat{i}$ (b).

Estimation of the $r-L$ equivalent of the DC microgrid under ramp power change at the Pex

The power sharing measurements are shown in Fig. 5.20a and the voltages at the terminals of each device are shown in Fig. 5.20b. The system is the master/slave coordinated: DG_1 maintains the voltage of the DC microgrid, ES_1 and DG_2 inject constant power according to a reference value from a centralized power management system and Pex exchanges the power to the AC system according to this reference. Three step changes in the power consumed by the Pex occur during the initial phase of the estimation, at $t \in \{5, 20\}$ s. A ramp power reference has been added to the Pex, to start the ramp after 35 s. This reference ramp stops when the power generation limit has been reached.

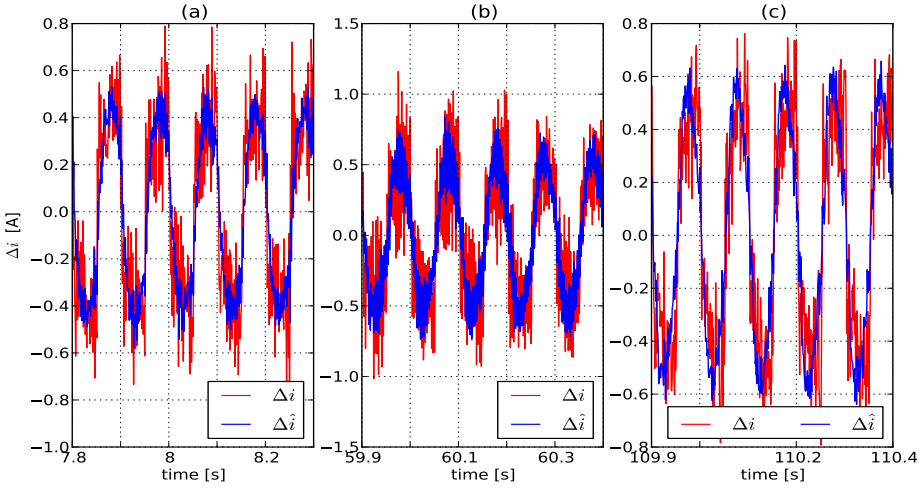

Figure 5.19: Zoom of the RLSE estimation of Δi. Time segment $7.8 < t < 8.3$ s (a). Time segment $59.9 < t < 60.4$ s (b). Time segment $109.9 < t < 110.4$ s (c).

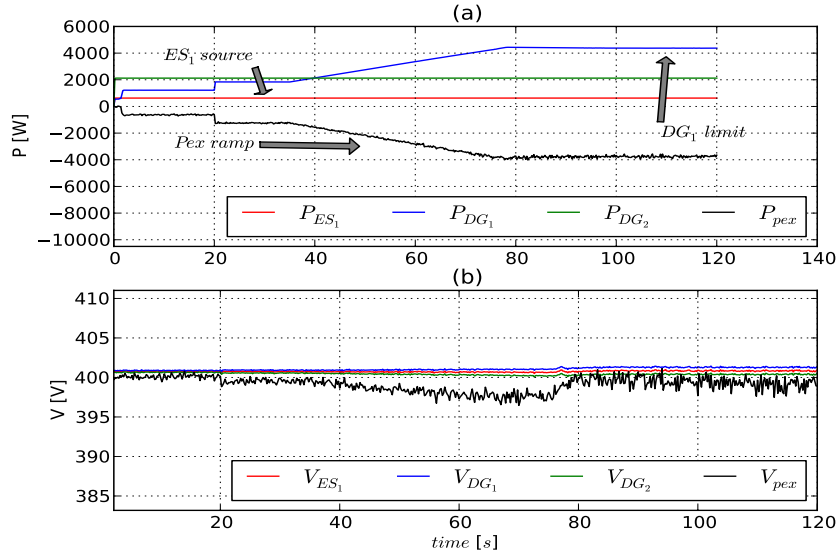

Figure 5.20: Power sharing of the *DGs* with a trip of ES at 100 s (a). Voltage measured at terminals of each *DG* and *Pex* (b).

The estimated equivalent impedance is shown in Fig. 5.21. Figure 5.21a presents the estimated r. The KF and RLSE algorithms have been applied to estimate r and L. The values of the parameters change as a function of the current. The values of r and L decrease while the current consumed by the Pex is changing. The power limit is reached before 80 s and the power consumed by Pex is kept constant. After 80 s, the estimated values of r and L initially increase but are subsequently kept constant.

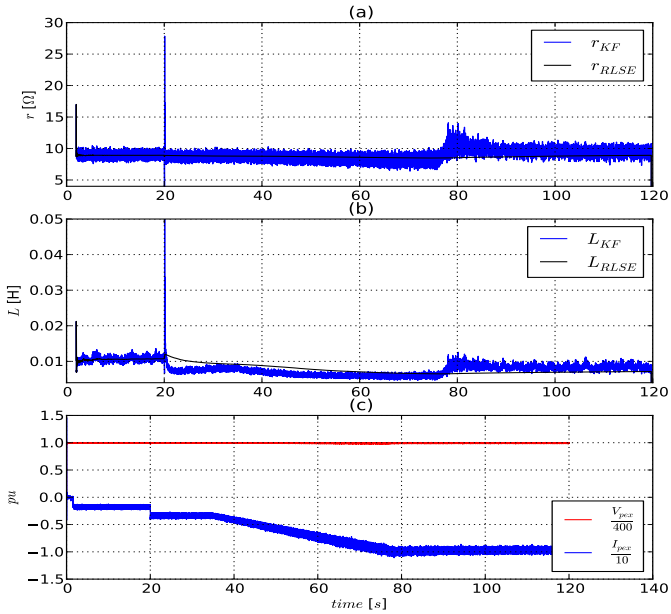

Figure 5.21: $r - L$ estimation. Estimation of the resistance (a), estimation of the equivalent inductor (b), Voltage and current at node pcc_5 (c).

The estimated resistance (r), and inductor (L) obtained by the KF method and the Pex power have been filtered with a moving average filter with 2^8 samples to describe the behavior of the estimation as a function of power. The KF estimator and average values for r, L and power are shown in Fig. 5.22. The change of the estimated values as a function of power at the Pex is shown in Fig. 5.23. The average r and L decreases while the power increases.

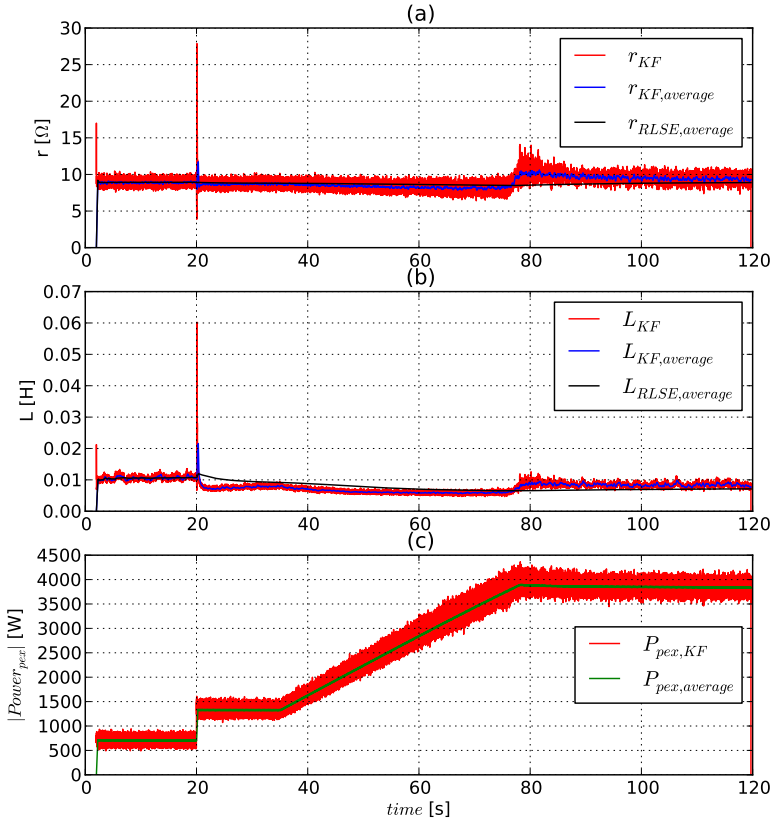

Figure 5.22: Filtered signals of $r - L$ estimation. Resistance (a), inductor (b), absolute value of the Pex power (c).

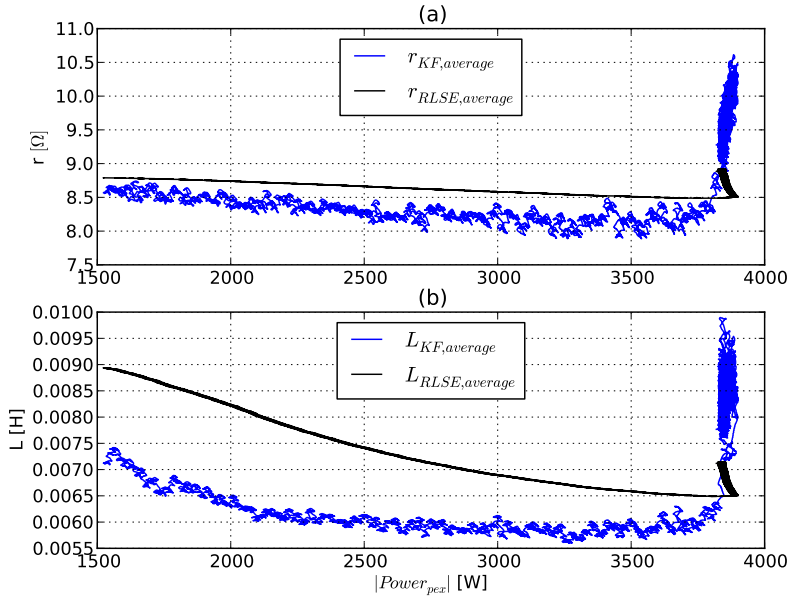

Figure 5.23: Change of $r-L$ as a function of the power change at Pex. Resistance (a), inductor (b).

5.7 Estimated impedance of a Renewable Energy System Laboratory DC-grid

The estimation procedure was applied to the power electronics DC network described in Fig. 5.24. The network is in the Renewable Energy System Laboratory [94]. The rated power of the voltage source converters is 60 kVA. They use a two-level configuration based on insulated gate bipolar transistors (IGBTs) which switch at 5 kHz. The voltage of the system is controlled by the converter b. Converter a consumes power from the DC grid and operates as a current controlled load. Converter b consumes power from the DC network. The perturbation signal has been added to its reference current to estimate the impedance equivalent.

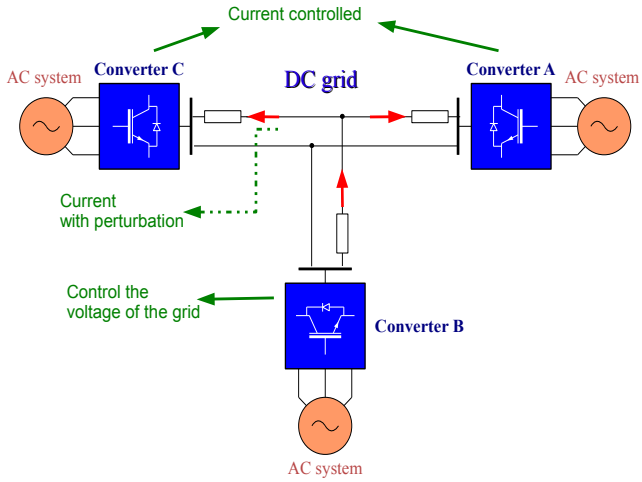

Figure 5.24: DC power electronics network at the Renewable Energy System and Smart Grid Laboratory (NTNU/SINTEF).

The voltage at the converter c is shown in Fig. 5.25. It has been divided by 600. The currents at the terminals of the converters a and c are shown in Fig. 5.25. They have been scaled by a factor of 30. The sampling period is $T_s = 1$ ms. The current of the converter I_c is used as the perturbation signal, and has a frequency sweep from 1 to 100Hz. The DC perturbation current is produced by controlling the direct axis current.

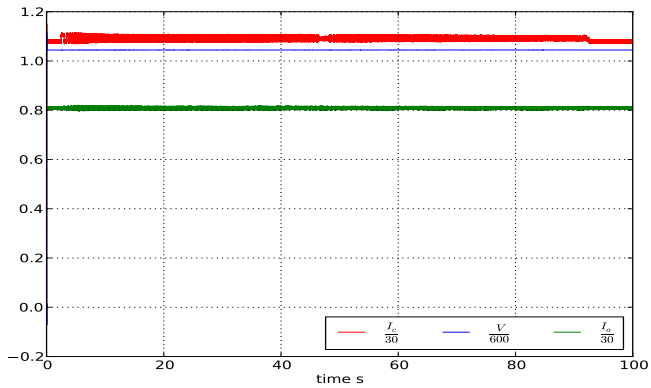

Figure 5.25: Voltages and currents of the DC power electronics network.

5.7.1 Estimation results of the equivalent impedance

The equivalent resistance and inductor impedance estimated with the Kalman filter (KF) and recursive least squares (RLSE) is presented in Fig. 5.26.

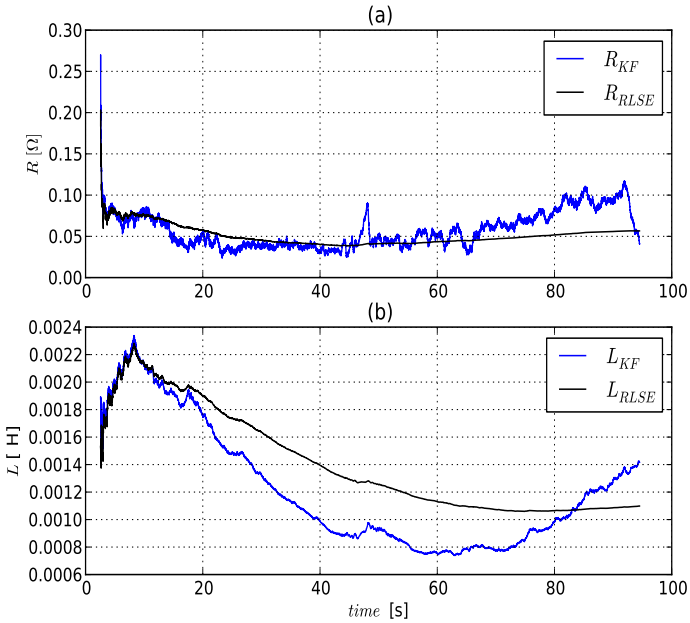

Figure 5.26: R-L estimated for the Renewable Energy System and Smart Grid Laboratory (NTNU/SINTEF) DC-network.

The current perturbation applied to the system has been analyzed with the spectrogram shown in Fig. 5.27. The DC average component of the current was removed to obtain the spectrogram. It can be seen from the spectrogram that the perturbation frequency ranges between 1 and 100 Hz. However a 50 Hz component is shown in Fig. 5.27.

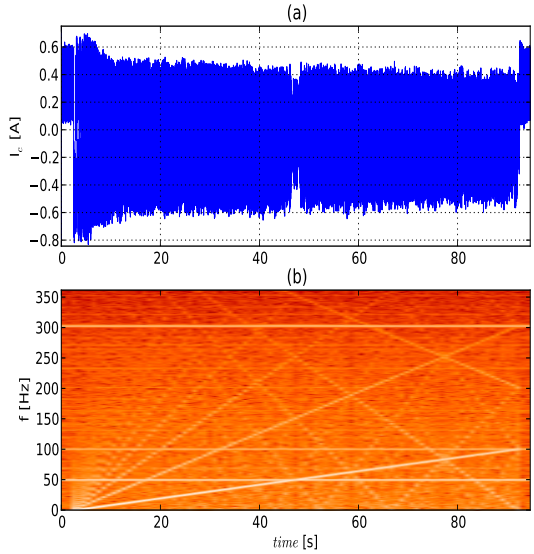

Figure 5.27: Current perturbation at converter c.

The spectrogram of the voltage V_c at the terminals of the converter c is shown in Fig. 5.28. The average DC voltage has been removed. A component at 50 Hz is observed in the spectrogram, and the second, third and fifth harmonic are also presented. The frequency components are inside the range of [1-50] Hz (Fig. 5.28b). However, the components ranging from [1-40] Hz are significant. Therefore, a Fourier analysis was used for the voltage and the current at converter c for the frequencies in the range of [1-40] Hz. The impedance can then be computed in the frequency domain with the frequency scanning procedure.

The analysis of the measurements used with the recursive estimation methods (*i.e.* Δi and Δv) is shown in Fig. 5.29 and Fig. 5.30, respectively. This analysis identifies the same frequency components for the differences in current and voltage signals. The components for Δi are inside the range [1-100] Hz and the significant frequency components for Δv are inside [1-40] Hz.

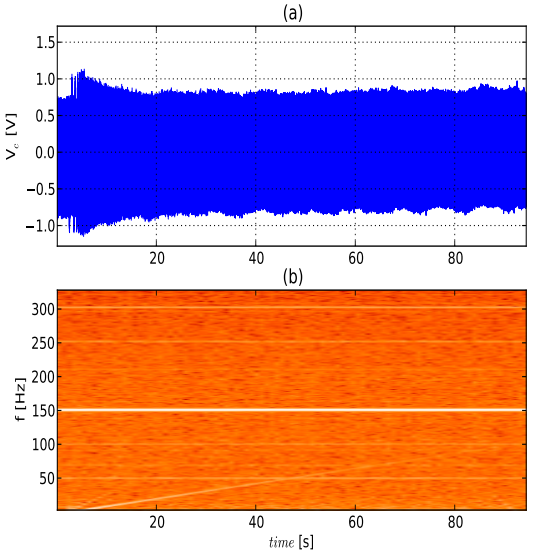

Figure 5.28: Voltage behavior under the current perturbation at converter c.

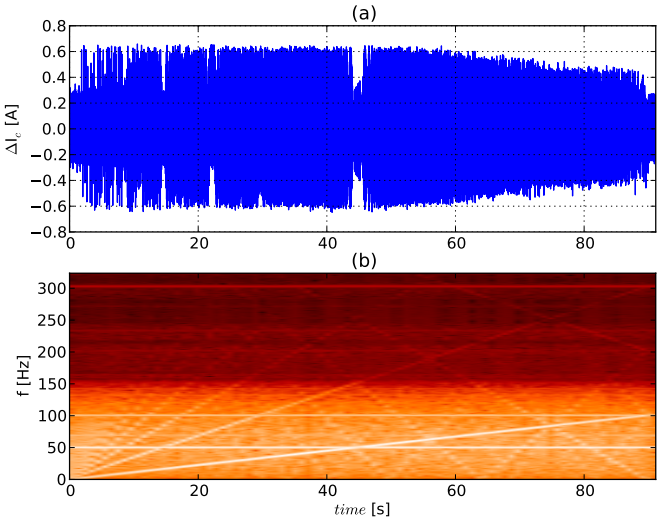

Figure 5.29: Current perturbation Δi at converter c with the KF and RLSE methods.

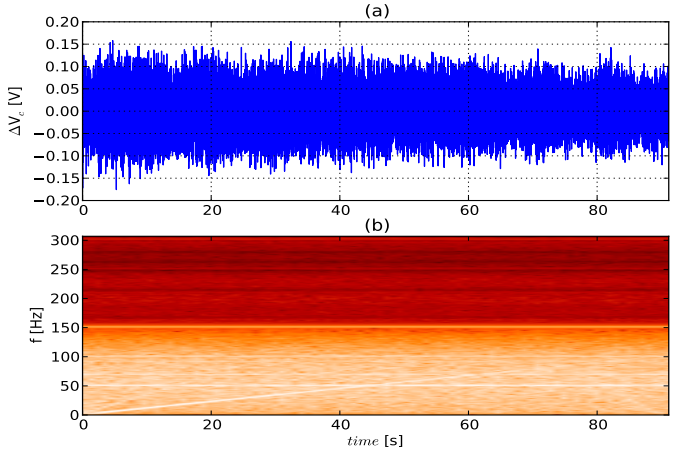

Figure 5.30: Voltage Δv under the current perturbation at converter c with the KF and RLSE methods.

The impedance obtained by frequency scanning is shown in Fig. 5.31. The equivalent impedance estimated with the KF and RLSE methods is also presented in the frequency domain in this figure. The average equivalent resistance and inductor estimated with the KF method were used to obtain the impedance magnitude $Z_{KF,av}$ and the phase $\phi_{KF,av}$. The frequency scanning impedance computed with the signals Δi and Δv is represented as $Z_{\Delta.freqsc}$ for the magnitude and $\phi_{\Delta.freqsc}$. The value of the impedances Z_{freqsc}, Z_{KF} and Z_{RLSE} are similar at low frequencies (1 Hz). The behavior of the R-L equivalents is different from that of the equivalent obtained by frequency scanning. A similar performance was obtained when the network link of the converter that is used to estimate the equivalent impedance has low inductive coupling.

5.8 Final considerations on long term model and stability

In this chapter, an equivalent representation of the DC microgrid was developed. The recursive approach is used to compute the parameters of a system operating around one point. Hence, the microgrid equivalent can be estimated inside a region, taking into account changes in the operation point, and with several frequency trajectories, in contrast with classical off-line techniques which only involve one. In addition, in this chapter, it was demonstrated that the method of two operation points inside a small region gives satisfactory results. The long-

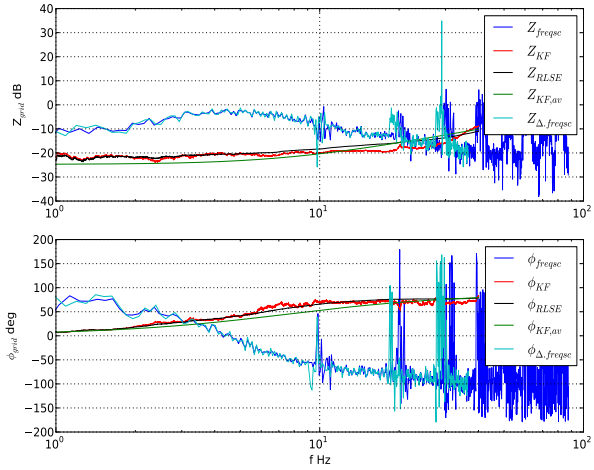

Figure 5.31: Impedance of the DC network in the Renewable Energy System and Smart Grid Laboratory (NTNU/SINTEF).

term stability of the signal was then tested with this technique, which showed that the microgrid operator can manage the power exchanged or change the control strategy used in its device to avoid unstable boundaries. Alternatively, the system could be designed to ensure its operation in a secure region. The equivalent microgrid impedance obtained could then be applied to a small signal stability test. However, errors at frequencies above 10 Hz will be observed for light inductive DC microgrids.

Equivalent systems have been extensively used in the literature to represent the dynamic of the remaining part of the grid. From the work presented here, the following conclusions can be made: the estimated equivalent and the model of the Pex should be used for low frequency tests and not for fast transient stability. The recursive estimation takes into account the RL parameters in a straight form. This method is based on the voltage and current time samples at the terminals of the exchanger device.

Figure 5.17 and Fig. 5.19 reveal an error associated with the estimation of the perturbation current Δi. This estimation error is caused by the first order model of the system (5.20)-(5.21). However, the use of the first order model offers and advantage: it is related to the physical parameters r and L of an equivalent impedance with resistive-inductive behavior. Some rippling can be seen in the

Table 5.3: Root mean square error of estimated Δi with different model orders.

Order	RMSE [A]
1	0.20304
2	0.15227
3	0.14156
4	0.13422
5	0.13169
6	0.12737

measurements of the current and Δi. Therefore, the discrete time system can be represented with a higher order model as in (5.51). The output is $y_k = \Delta i_k$.

$$\Delta i_k = \begin{bmatrix} \phi_1 & ... & \phi_m \end{bmatrix} \begin{bmatrix} \Delta i_{k-1} \\ \vdots \\ \Delta i_{k-m} \end{bmatrix} + \begin{bmatrix} \gamma_1 & ... & \gamma_m \end{bmatrix} \begin{bmatrix} \Delta v_{k-1} \\ \vdots \\ \Delta v_{k-m} \end{bmatrix} \tag{5.51}$$

where m is the order of the model.

Figure 5.32 shows the estimation parameters ϕ and γ with the KF method for a 6th-order model. The spikes observed during the estimation of the $r - L$ model (*i.e.* first order model) is not presented when a higher order model is used. Figure 5.33 shows the error of the estimation current, the estimated perturbation current and the current perturbation. The root mean square error (RMSE) of this model is η= 0.12737 A, whereas the first order model has an RMSE $\eta = 0.20304$ A. Table 5.3 shows the RMSE for different orders of the model. The RMSE decreases as the order of the model increases. The estimation parameters for different orders of the model are shown in Appendix D.

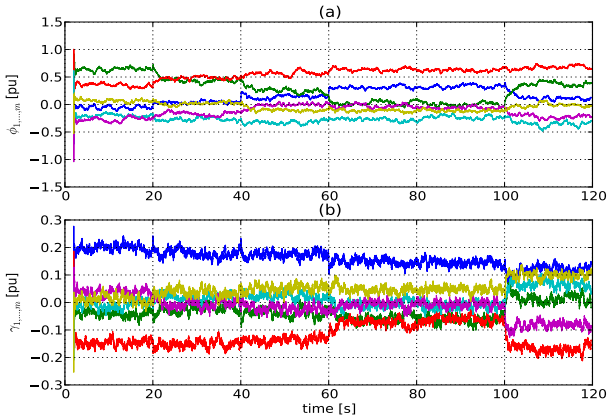

Figure 5.32: Estimation parameters for the 6th-order model. Parameters ϕ_k (a), parameters γ_k (b), $k \in \{1, ..., 6\}$.

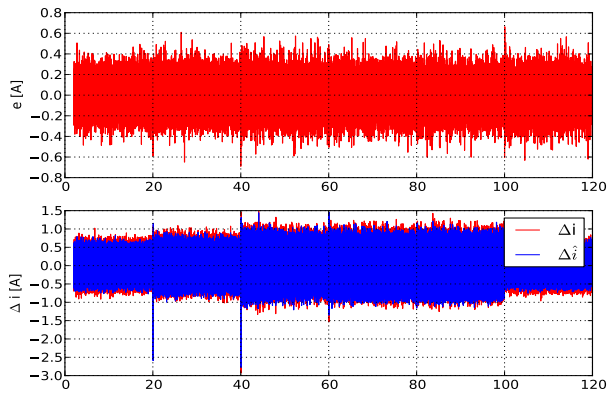

Figure 5.33: Current estimation for the 6th-order model. Error (a), Current perturbation Δi and estimated current perturbation $\Delta \hat{i}$ (b).

5.8.1 Comparison of the frequency scanning technique and the n-th order KF estimation

The power sharing of the benchmark DC network is shown in Fig. 5.34. The operation point at 10 s is shown in Fig. 5.34, and is used to analyze the frequency response of the n-th order discrete model estimated with the semi-recursive method.

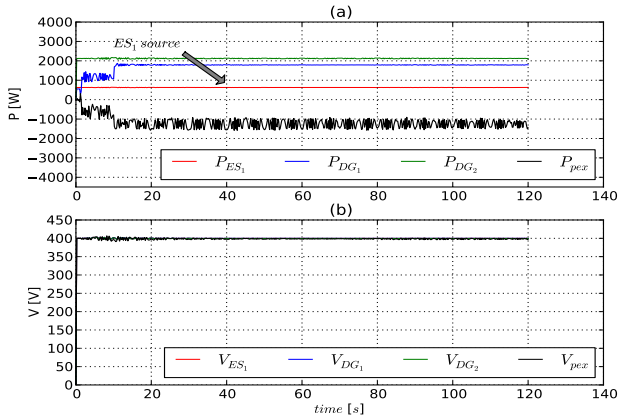

Figure 5.34: Power of the devices in the grid (a), voltage (b).

The current perturbation shown in Fig. 5.35 has been applied at the terminals of the *Pex* to enable the frequency response of the frequency scanning technique and that of the n-th order KF estimator to be compared. A frequency perturbation from 20 Hz up to 90 Hz is shown. The voltage at the DC side of the *Pex* has been analyzed to obtain the available frequency range that provides a good estimation of the equivalent impedance (Fig. 5.36).

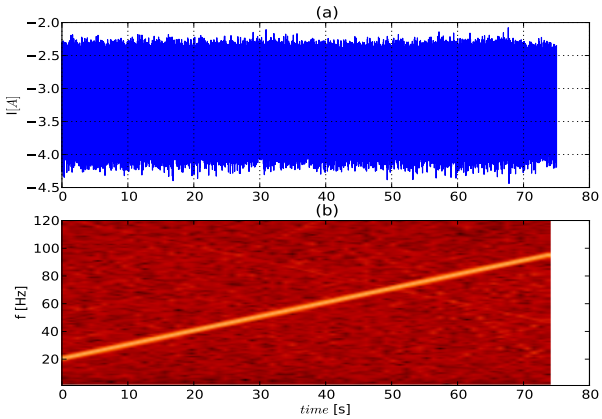

Figure 5.35: Current spectrum at the *Pex*. Time domain behavior (a), Frequency-time spectrum (b).

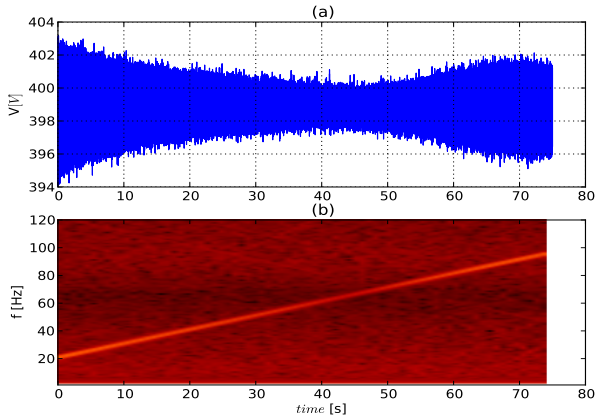

Figure 5.36: Voltage spectrum at the Pex. Time domain behavior (a), Frequency-time spectrum (b).

Figure 5.37 shows the estimation parameters ϕ and γ with the KF method for a 5th-order model. The KF estimation method uses a window with a frequency of 100 Hz and the sampling frequency of the signal is 1 kHz.

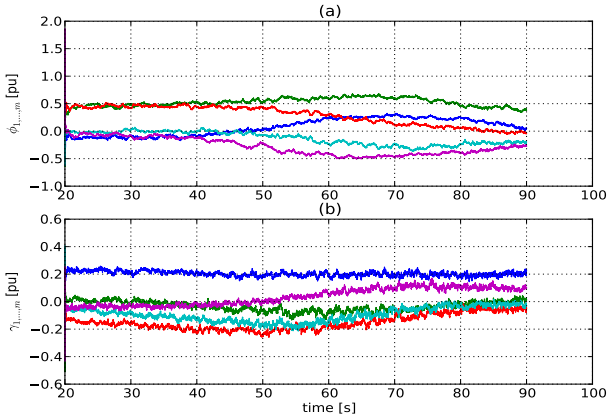

Figure 5.37: Parameters of a 5-th order estimation. Parameters —ϕ_1, —ϕ_2, —ϕ_3, —ϕ_4, —ϕ_5 (a), parameters —γ_1, —γ_2, —γ_3, —γ_4, —γ_5 (b).

The frequency response of the model estimated with the KF method and the frequency scanning technique are shown in Fig. 5.38. It can be seen from this comparison that the 5-th order KF estimated model has the same frequency response as the impedance obtained with the frequency scanning technique. The

use of a higher order model provides better behavior than the r-L impedance equivalent, and there is no loss of the dynamic present in the system.

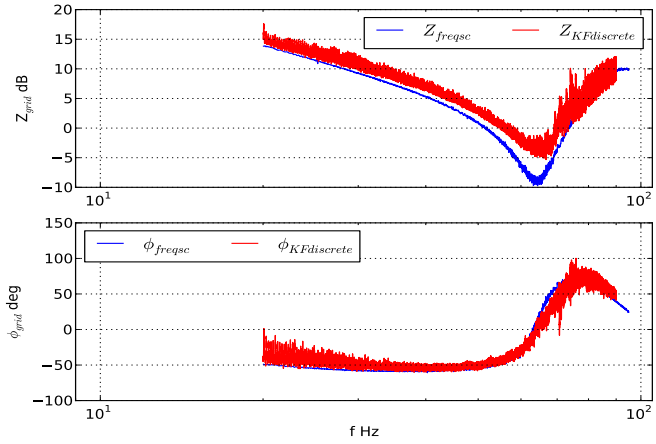

Figure 5.38: Frequency response of the KF model and the frequency scanning technique of the microgrid simulation benchmark. Magnitude (a), phase (b).

Proof of concept with the renewable energy system and smart grid laboratory DC grid

The frequency response of the model estimated with the KF method and the frequency scanning technique are shown in Fig. 5.39. The frequency response for the 15th and 25th KF models consistent between 4 Hz and 30 Hz. However, the upper limit of the range of the 15th order model is 20 Hz. Below 4 Hz, there is an error of the estimated model with respect to the frequency scanning response. The response of the model estimated with KF is better for higher order than lower order models. However, higher order models require a long the computational time.

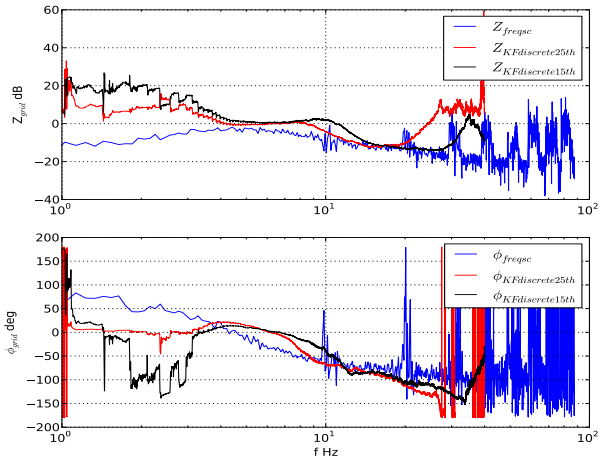

Figure 5.39: Frequency response of the KF model and the frequency scanning technique for the laboratory DC grid. Magnitude (a), phase (b).

5.8.2 Improvement of the stability

The five possible solutions discussed in [14] can be used to stabilize the system. These solutions are discussed with respect to the system described by (5.4)-(5.5). The first solution involves an increase in r. However, this is not possible because r is a function of the operation point and coordination of the microgrid. Similarly, the second solution, which proposes a decrease in L, is also not feasible in this case because L is a function of the operation point. The third solution involves an increase in the capacitor C of the Pex, which is possible by the application of a switched capacitor bank. The fourth solution , which is to increase the voltage v, is not feasible because the voltage is a function of the nominal value set for the operation of the grid. Finally, the fifth solution, which involves controlling CPL dynamics, adds a dynamic to the reference power P.

The analysis of stability in this chapter is based on the long-term equivalent of the system. However, one question relevant to this project remains unsolved. The question concerns the stability of a system under a defined coordination: to what extent do the states or parameters influence the stability of a DC microgrid? This issue will be discussed in the next chapter.

Chapter 6

Degree of influence of the parameters and states on the stability of the system

The chapter presents a methodology that takes into account the structure of a DC microgrid system and evaluates its stability. In the stability analysis, computational continuation is used to obtain the conclusions.

In this chapter, the stability is studied with a continuation algorithm. One of the advantages of this analysis is the use of nonlinear dynamics. This mathematical analysis has been widely used to study so-called large stability in classical power systems (*i.e. voltage stability*). Loadability and controllability tests are used during the analysis presented in this chapter. It is assumed that the parameters and the dynamic model of the devices are known.

The structure of the DC microgrid used in this chapter is shown in Fig. 6.1. DG_1 controls the voltage of the grid, DG_2 and ES_1 inject constant current into the network and Pex exports power from the DC microgrid to an AC system. This coordination is the master/slave control technique of parallel converters [43].

6.1 Numerical continuation of fixed points

A bifurcation study was carried out with the Davidenko-Newton Raphson method, to obtain a branch of the states produced when a parameter changes in the system [90]. This method works as a predictor-corrector. The continuation parameter is defined as α, the equilibrium of $\dot{x}(t) = F(x(t), \alpha)$ is obtained as $\alpha \in \mathcal{R}^1$,

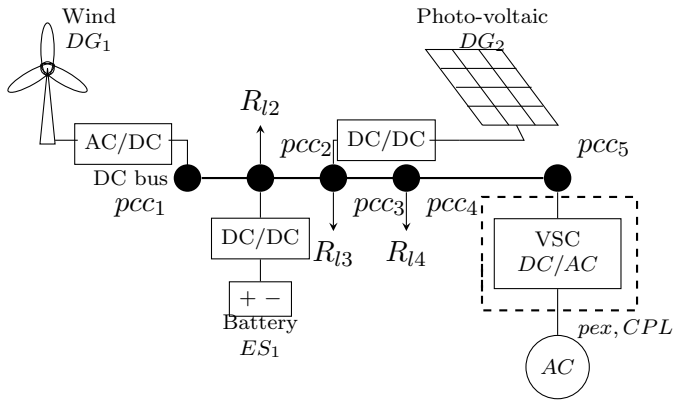

Figure 6.1: DC microgrid configuration

which varies while the remaining parameters are kept constant[1]. The state vector is $x \in \mathcal{R}^n$, and the nonlinear function F maps $\mathcal{R}^n \times \mathcal{R}^m$ into $\mathcal{R}^n$. This method has been widely used in stability tests for transmission systems [95]. The continuation method is convenient to use because it converges quickly with the Newton-Raphson algorithm during the corrector step. When a convergence problem is encountered, the continuation parameter changes to a component of the state variables, where α is fixed [3,96]. Therefore, the Davidenko-Newton Raphson method uses the differentiation of:

$$0 = F(x, u, \alpha), \tag{6.1}$$

with respect to α.

$$F_x(x, \alpha)\frac{dx}{d\alpha} = -F_\alpha(x, \alpha), \tag{6.2}$$

where F_x is the Jacobian with respect to the states, and F_α is the Jacobian with respect to the continuation parameter. Finally, after solving (6.2) for $dx/d\alpha$, the method finds the equilibria [3,95]. The branch of solutions in the state-parameter space is shown to illustrate the behavior of the states. Additionally, the eigenvalues of each point in the defined space provide information about the stability following variation of the parameter and states.

Essentially, the complete system is formed when the network equations, the converter dynamics and controllers are coupled. The full model is presented in the next section of this chapter.

[1]In the interest of brevity, the argument t is omitted from the time functions when its value is clear from the context.

6.1.1 Local properties of the operation point

The method applied to evaluate the properties of the operation point is the participation factor of the system. It describes the influence of a state variable over the eigenvalues. The Jacobian (F_x) is evaluated at a selected operation point, followed by computation of the eigenvalues and eigenvector. The participation factor can then be used to correlate oscillatory or exponential behavior of the system [60].

6.2 Dynamic model of the complete DC microgrid

The full system is modeled as a combination of the dynamics of each distributed generator, the DC network dynamics presented in chapter 3 and the model of the Pex.

6.2.1 DC network model

The dynamic model of the DC network shown in Fig. 6.2 was developed in section 3.2. Here, the final set of differential equations are shown. This set will be coupled with the dynamics of energy storage, the distributed generators and the power exchanger.

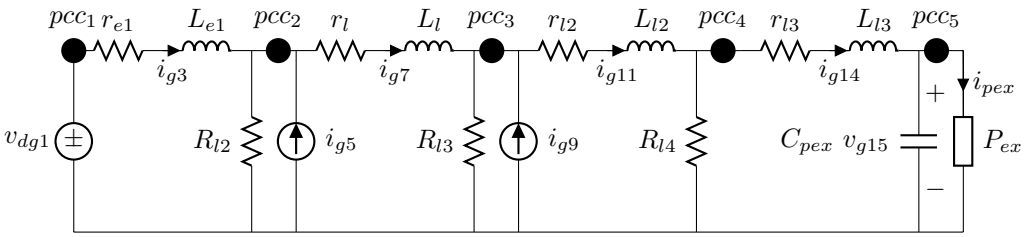

Figure 6.2: DC network model for the continuation method.

$$\frac{d}{dt}i_{g3} = \frac{R_{l2}(i_{g7} - i_{g5}) - (R_{l2} + r_{e1})i_{g3} + v_{dg1}}{L_{e1}} \tag{6.3}$$

$$\frac{d}{dt}i_{g7} = \frac{R_{l3}(i_{g11} - i_{g9}) - (R_{l3} + r_l + R_{l2})i_{g7} + R_{l2}(i_{g3} + i_{g5})}{L_l} \tag{6.4}$$

$$\frac{d}{dt}i_{g11} = \frac{R_{l4}i_{g14} - (r_{l2} + R_{l4} + R_{l3})i_{g11} + R_{l3}(i_{g7} + i_{g9})}{L_{l2}} \tag{6.5}$$

$$\frac{d}{dt}i_{g14} = \frac{R_{l4}i_{g11} - v_{g15} - (r_{l3} + R_{l4})i_{g14}}{L_{l3}} \tag{6.6}$$

$$\frac{d}{dt}v_{g15} = \frac{i_{g14} - i_{pex}}{C_{pex}} \tag{6.7}$$

where the states are i_{g3}, i_{g7}, i_{g11}, i_{g14} and v_{g15}, the constant impedance loads are R_{l2}, R_{l3}, R_{l4}, and the power exchanger capacitor is C_{pex}. The remaining part of the exchanger device is represented as a load function of the current i_{pex}. The current source i_{g5} represents ES_1 and the current source i_{g9} represents DG_2. The line dynamics are characterized by a resistive and an inductive part as follows: r_{e1}, L_{e1} is the line between $pcc_1 - pcc_2$, r_l, L_l is the line between $pcc_2 - pcc_3$, r_{l2}, L_{l2} is the line between $pcc_3 - pcc_4$ and r_{l3}, and L_{l3} is the line between $pcc_4 - pcc_5$.

6.2.2 The DG_1 model

The DG_1 system uses a boost converter to control the voltage at the node pcc_1. The circuit of the converter is shown in Fig. 6.3.

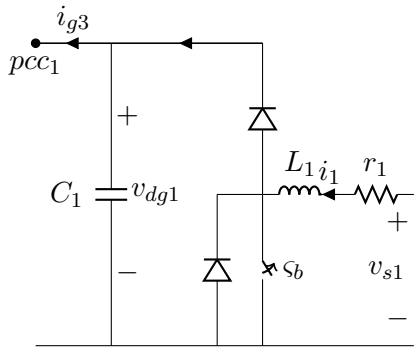

Figure 6.3: Boost converter used in DG_1.

The dynamics of the converter are described in (6.8) to (6.9). Of note, s_1 has been used instead of $(1 - \varsigma_b)$ to represent the switching dynamics (*i.e.* from the

model in chapter 3.5.4). The parameters of the system are the capacitor C_1, the inductor L_1 and the resistance r_1. The state variables of the DG_1 are the inductor current, i_1, and the capacitor voltage, v_{dg1}. The current that links the converter to the DC network is i_{g3}. Finally, the voltage at the input terminals is v_{s1}.

$$\frac{di_1}{dt} = -\frac{r_1}{L_1} i_1 + \frac{v_{s1}}{L_1} - \frac{s_1 v_{dg1}}{L_1} \tag{6.8}$$

$$\frac{dv_{dg1}}{dt} = \frac{s_1 i_1 - i_{g3}}{C_1} \tag{6.9}$$

The current controller is described in (6.10) and (6.11). The controller adds the state γ_1 to the dynamics of the system. The reference current is i_{ref1}, the parameters of the PI current controller are k_{p1} and k_{i1} and the reference voltage of the network is v_{dg1ref}.

$$\frac{d\gamma_1}{dt} = i_{ref1} - i_1 \tag{6.10}$$

$$s_1 = -\frac{\left(k_{p1}\left(i_{ref1} - i_1\right) + k_{i1}\gamma_1\right)}{v_{dg1ref}} \tag{6.11}$$

The voltage controller is presented in (6.12) and (6.13). The state of the controller is γ_{v1}, the proportional gain is k_{pv1} and the integral gain is k_{iv1}.

$$\frac{d\gamma_{v1}}{dt} = v_{dg1ref} - v_{dg1} \tag{6.12}$$

$$i_{ref1} = k_{pv1}\left(v_{dg1ref} - v_{dg1}\right) + k_{iv1}\gamma_{v1} \tag{6.13}$$

6.2.3 *Pex* model

This subsection describes the model of the device (Fig. 6.4) used to export power in the DC microgrid. The dynamic model is described by the set of equations from (6.14) to (6.17). The passive elements of the converter are the inductor L, the resistive part of the inductor r, and the DC capacitor C_{pex}. The state variables of the system are the synchronous reference frame currents, i_{dvsc} and i_{qvsc} and the DC voltage v_{g15}. The current i_{pex} is a function of the state currents and the control voltages v_d and v_q. The angular speed is ω and the grid current is i_{g14}.

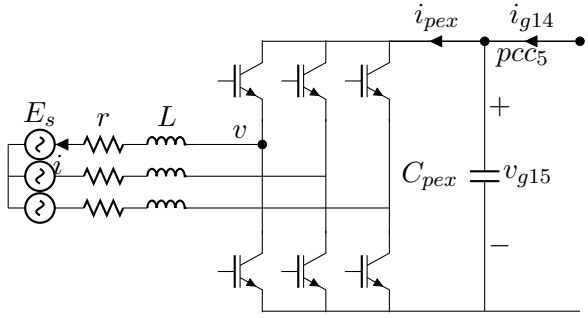

Figure 6.4: VSC converter used in Pex.

$$\frac{di_{dvsc}}{dt} = \frac{v_d - E_{sd} + \omega L i_{qvsc} - r i_{dvsc}}{L} \tag{6.14}$$

$$\frac{di_{qvsc}}{dt} = \frac{v_q - E_{sq} - \omega L i_{dvsc} - r i_{qvsc}}{L} \tag{6.15}$$

$$\frac{dv_{g15}}{dt} = \frac{i_{g14} - i_{pex}}{C_{pex}} \tag{6.16}$$

$$i_{pex} = \frac{3}{2}\frac{(v_d i_{dvsc} + v_q i_{qvsc})}{v_{g15}} \tag{6.17}$$

It can be seen that (6.16) is equal to (6.7), which links the Pex with the network at the node pcc_5. The controller applied is described in (6.18) to (6.22).

$$v_d = \gamma_{dvsc} k_{ivsc} + k_{pvsc}\left(i_{dref} - i_{dvsc}\right) + E_{sd} - \omega L i_{qvsc} \tag{6.18}$$

$$v_q = \gamma_{qvsc} k_{ivsc} + k_{pvsc}\left(i_{qref} - i_{qvsc}\right) + E_{sq} + \omega L i_{dvsc} \tag{6.19}$$

$$\frac{d\gamma_{dvsc}}{dt} = i_{dref} - i_{dvsc} \tag{6.20}$$

$$\frac{d\gamma_{qvsc}}{dt} = i_{qref} - i_{qvsc} \tag{6.21}$$

$$\tag{6.22}$$

6.3 The DC microgrid model

The closed loop equations of each device are required to obtain the final model. Hence, the DG_1 closed loop system is obtained by combining the controllers (6.13)-(6.13) and (6.10)-(6.11) with the boost dynamics (6.8)-(6.9). This set is presented

in (6.23) to (6.26).

$$\frac{di_1}{dt} = \frac{1}{L_1}\left(v_{s1} - i_1 r_1 + v_{dg1}\frac{\gamma_1 k_{i1} + k_{p1}\big(\gamma_{v1}k_{iv1} - i_1 + k_{pv1}\left(v_{dg1ref} - v_{dg1}\right)\big)}{v_{dg1ref}}\right) \tag{6.23}$$

$$\frac{dv_{dg1}}{dt} = \frac{1}{C_1}\left(i_1\frac{-\gamma_1 k_{i1} - k_{p1}\big(\gamma_{v1}k_{iv1} - i_1 + k_{pv1}\left(v_{dg1ref} - v_{dg1}\right)\big)}{v_{dg1ref}} - i_{g3}\right) \tag{6.24}$$

$$\frac{d\gamma_1}{dt} = \gamma_{v1}k_{iv1} - i_1 + k_{pv1}(v_{dg1ref} - v_{dg1}) \tag{6.25}$$

$$\frac{d\gamma_{v1}}{dt} = v_{dg1ref} - v_{dg1} \tag{6.26}$$

The next step combines the controller equations of Pex (6.18)-(6.22), with the dynamics defined in (6.14) to (6.17). The closed loop Pex is defined by (6.27)-(6.30).

$$\frac{di_d}{dt} = \frac{1}{L}\Big(-(r + k_{pvsc})i_d + \gamma_{dvsc}k_{ivsc} + i_{dref}k_{pvsc}\Big) \tag{6.27}$$

$$\frac{di_q}{dt} = \frac{1}{L}\Big(-(r + k_{pvsc})i_q + \gamma_{qvsc}k_{ivsc} + i_{qref}k_{pvsc}\Big) \tag{6.28}$$

$$\frac{d\gamma_{dvsc}}{dt} = i_{dref} - i_d \tag{6.29}$$

$$\frac{d\gamma_{qvsc}}{dt} = i_{qref} - i_q \tag{6.30}$$

The combination of the controller with (6.16) has been presented as a part of the network system. Therefore, the closed loop model of the voltage grid v_{g15} is (6.31).

$$\begin{aligned}\frac{dv_{g15}}{dt} = \frac{3}{2v_{g15}C_{pex}}\big(&-E_{sd}i_d - E_{sq}i_q - \gamma_{dvsc}i_d k_{ivsc} - \gamma_{qvsc}i_q k_{ivsc} + \\ &k_{pvsc}i_d^2 - i_d i_{dref}k_{pvsc} + k_{pvsc}i_q^2 - i_q i_{qref}k_{pvsc}\big) + \frac{i_{g14}}{C_{pex}}\end{aligned} \tag{6.31}$$

The remaining set of differential equations that describe the network are shown

below:

$$\frac{d}{dt}i_{g3} = \frac{R_{l2}(i_{g7} - i_{g5}) - (R_{l2} + r_{e1})i_{g3} + v_{dg1}}{L_{e1}} \tag{6.32}$$

$$\frac{d}{dt}i_{g7} = \frac{R_{l3}(i_{g11} - i_{g9}) - (R_{l3} + r_l + R_{l2})i_{g7} + R_{l2}(i_{g3} + i_{g5})}{L_l} \tag{6.33}$$

$$\frac{d}{dt}i_{g11} = \frac{R_{l4}i_{g14} - (r_{l2} + R_{l4} + R_{l3})i_{g11} + R_{l3}(i_{g7} + i_{g9})}{L_{l2}} \tag{6.34}$$

$$\frac{d}{dt}i_{g14} = \frac{R_{l4}i_{g11} - v_{g15} - (r_{l3} + R_{l4})i_{g14}}{L_{l3}} \tag{6.35}$$

6.4 Results

Loadability and controllability were tested for the DC-microgrid described in Fig. 3.2. In this test, the boost converter is used as the distributed generator and the VSC as the Pex. In the continuation method, the models of each system were carefully coupled to form a complete nonlinear system. A symbolic computation software [97] was used. The simulation results of the system operating with the designed set of parameters is consistent with the values presented in Fig. 6.7 and Fig. 6.10. The initialization point is the first value of the continuation parameter used (st). The grid values were initialized by applying a ladder DC power flow in addition to the distributed generation, according to the distribution power flow for complex power [98]. Initialization of the variables in the converters is performed using the set point obtained in the DC power flow as a known value.

The first analysis is based on the local properties, and involves the participation factors. Table 6.1 and Table 6.2 show the eigenvalues for cases A and B, respectively. The eigenvalue λ is defined as $\lambda = \sigma + j\beta$, and is composed of a real part σ and an imaginary part β. The relationship between states and eigenvalues is shown in Fig. 6.5 and Fig. 6.6. Values of the participation factor were used in the analysis. According to the damping ratio (ρ) defined in (6.36) [99], the weakest couple of modes for case A are $\lambda_{4,5}$. The complex eigenvalues $\lambda_{4,5}$ have a $\rho = 0.019$, which corresponds to an underdamped mode (*e.g.* $0 < \rho < 1$). From the participation factor analysis it is found that $\lambda_{4,5}$ are linked to the state variable i_{g14}, which can be associated with a loadability test at the node pcc_5.

$$\rho = \frac{\sigma}{\sqrt{\sigma^2 + \beta^2}} \tag{6.36}$$

In case B, the ratio for the couple of modes $\lambda_{6,7}$ is similar to the case A. In this case, $\rho = 0.031$.

Table 6.1: Participation factors for the micro-grid structure, case A.

No.	Eigenvalue (λ)	Main states (PFst value)
1	-2.447×10^7	$[\gamma_1, i_{g3}]$ (0.754, 0.192)
2	-1.691×10^7	$[i_{g11}, \gamma_1, i_{g3}]$ (0.3615, 0.223, 0.4128)
3	-1.521×10^6	$[i_{g3}, i_{g11}]$ (0.384, 0.579)
4,5	-69.034± 3.576 × $10^3 j$	$[v_{g15}, \imath_{g14}, \gamma_{v1}]$ (0.1057, 0.386, 0.463)
6,7	-1411.131± 1850.517j	$[i_{dvsc}, v_{g15}, i_1]$ (0.4925, -0.141, 0.6342)
8,9	-83.607± 18.477j	$[\gamma_{qvsc}, i_{g14}, i_1, v_{g15}]$ (0.501, 0.109, -0.148, 0.535)
10,11	-11553.133± 0j	$[v_{dg1}, i_{g7}]$ (1.0, 1.0)
12,13	-74.235 ± 0j	$[i_{qvsc}, \gamma_{dvsc}]$ (1.0, 1.0)

6.4.1 Loadability limits in case A

The load demand of the grid has been changed to obtain the limits. The aim is to ensure that the border for the power exchanger remains over one established operation in the microgrid. In the local analysis carried out above, the weakness of the modes λ_4 and λ_5 is associated with the state variables v_{dg1}, i_{g14} and v_{g15}. Therefore, if this part of the system is loaded, the limit can be obtained. The result with the continuation algorithm is shown in Fig. 6.7. The initial point is st, and the bifurcation point obtained is HB. The loci of the eigenvalues described above is shown in Fig. 6.8. The value at which the eigenvalues cross the imaginary axis is ±3584.16. Consequently, the Hopf point is 570.43 Hz for $i_{dref} = 6.46$ A. Hence, the states have linear displacement because of the increment in load at P_{ex}.

The loadability test during and increase in the demand of the constant impedance load R_{l2} is shown in Fig. 6.9. The limit of stability for $R_{l2} = 35.8$. It is crucial to point out that the state variables γ_{v1}, i_1 and i_{g3} are significantly displaced. which shows the importance of considering the change of states during the stability analysis.

Table 6.2: Participation factors for the micro-grid structure, case B.

No.	Eigenvalue (λ)	Main states (PFst value)
1	-2.435×10^7	$[i_{g3}, i_{g11}, \gamma_1]$ (0.198,0.050 , 0.751)
2	-1.686×10^7	$[i_{g3}, i_{g11}, \gamma_1]$ (0.406,0.360 , 0.233)
3	-1.484×10^6	$[i_{g3}, i_{g11}]$ (0.395,0.5892)
4,5	-1.299×10^3 ± 1.884 × 10^3j	$[i_{dvsc}, i_1, v_{g15}]$ (0.498,0.693,-0.187)
6,7	-11.1776 ± 364.4524j	$[i_{g14}, \gamma_{v1}, v_{g15}]$ (0.423, 0.529, 0.06)
8,9	-87.2128±13.4588j	$[v_{g15}, i_1, \gamma_{qvsc}]$ (0.626, -0.166, 0.489)
10,11	-11.553×10^3± 0j	$[v_{dg1}, i_{g7}]$ (1.0000, 1.0000)
12,13	-74.2305	$[i_{qvsc}, \gamma_{dvsc}]$ (1.00, 1.00)

6.4.2 Loadability limits in case B

The loadability test in case B is performed by increasing the power consumed by the Pex unit. In the local analysis carried out above, the modes λ_9 and λ_{10} are associated with the state variables i_{g14} and v_{g15}. Therefore, if this part of the system is loaded, the limit can be obtained. The result with the continuation algorithm is shown in Fig. 6.10. The initial point is st, and the bifurcation point obtained is HB. The loci of the eigenvalues described above are shown in Fig. 6.11. The value at which the eigenvalues cross the imaginary axis is ±361.33. Consequently, the Hopf point is 57.51 Hz for $i_{dref} = 4.55$ A.

6.4.3 Boundary values for the controllers in case A

This subsection describes the control gain limits for the PI controller in the DG_1 unit[1].

The results of the continuation algorithm are shown in Fig. 6.12, where the continuation parameter from the boost is the outer loop integral gain, k_{iv1} (x-axis). The continuous line represents the stable states, and the dashed line the unstable ones. Displacement occurs when the integral constant k_{iv1} is changed,

[1]The controllability test can be performed for the remaining systems by applying the same procedure described for this step.

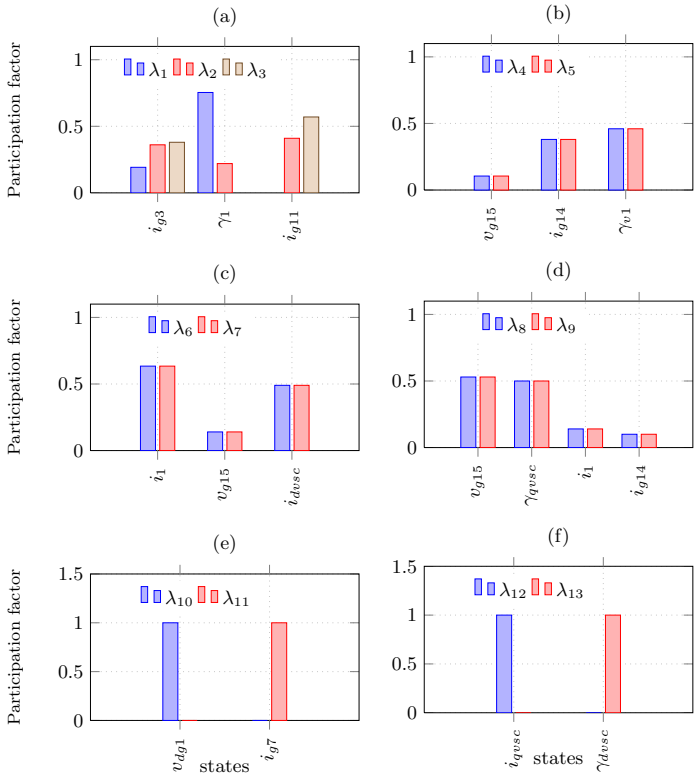

Figure 6.5: Participation factor for case A. Absolute values of the participation factors.

as shown by a state transition in the voltage controller.

Figure 6.13 shows the movement of the eigenvalues as a result of variation of k_{iv1}. Instability is reached around $k_{iv1} = 81.3$. The sign of the real part of two of the eigenvalues (λ_9, λ_{10}) changes. Thus, a non-stable operation can exist for large values of k_{iv1}. The eigenvalues cross the imaginary axis and are characterized by a Hopf bifurcation stability bound.

The second parameter tested in the controllability of the system is the proportional gain in the voltage loop. The loci of the eigenvalues with the continuation method are shown in Fig. 6.14. When the proportional gain is $k_{pv1} = 0.192$, the stability is lost by two modes crossing the imaginary axis. The states remain at the initial operation point without any movement.

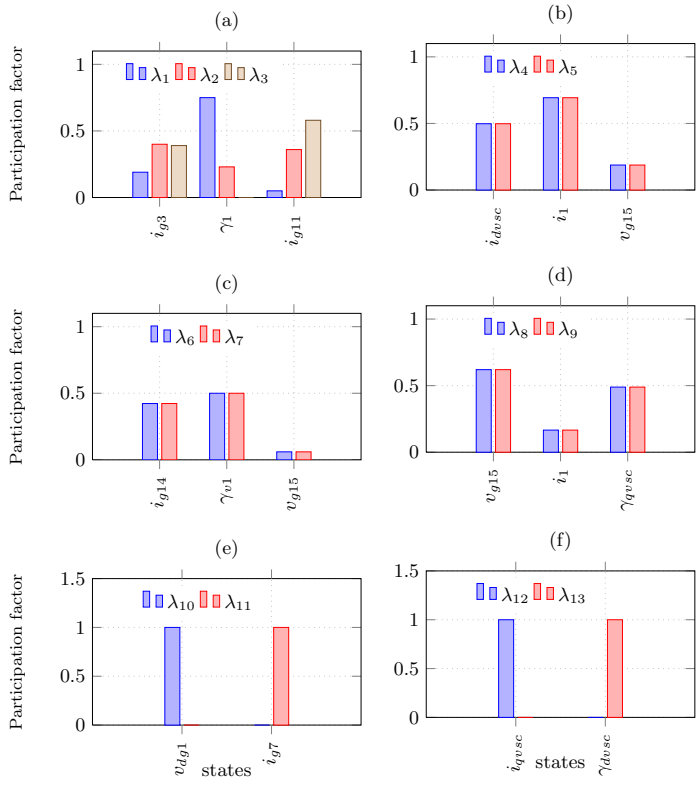

Figure 6.6: Participation factor for case B. Absolute values of the participation factors.

When the parameter under test is the controller gains in the inner loop, the instability margin is reached for values below zero. This test has been excluded because the procedure is already presented in [100], which demonstrates that the inner loop is stable for positive values of the controller gains in the boost converter. Hence, the problem can be reduced to the loadability.

6.4.4 Local stability test, case A

In this case, the linear matrix resulting from the linearization of the full model of the DC microgrid has been used. The operation point used is described for each local test. The loadability and controlability tests are described in the following subsections.

Loadability with the Pex

First, it is important to point out that this test uses the state values at its operation point $\bar{x} = [5.868,\ 0.000,\ 2.515 \times 10^{-5},\ 0.000,\ 3.039 \times 10^{1},\ 3.970 \times 10^{2},\ -8.273 \times 10^{-4},\ 2.575,\ 1.148 \times 10^{1},\ 1.010 \times 10^{1},\ 7.240,\ 4.457,\ 3.953 \times 10^{2}]$. They have not been changed to follow the same procedure used in a simple small signal test [60]. The parameter i_{dref} has been displaced. The operation point used is 10% below the unstable limit found with the continuation method for i_{dref}. The range used is $5.868 \leq i_{dref} \leq 6.968$ A. The loci of the eigenvalues is shown in Fig. 6.15. The eigenvalues λ_4 and λ_5 reach the imaginary axis at $i_{dref} \approx 6.6$. Therefore, this test gives rise to a misleading conclusion when the current consumed by the Pex is increased, because it suggests that unstable behavior can be reached above the limit found with the continuation method.

Controlability in DG_1, voltage loop test.

The parameter k_{iv1} in the voltage loop of DG_1 has been changed. The states have been kept constant at $\bar{x} = [2.000,\ 0.00,\ 8.573 \times 10^{-6},\ 0.00,\ 2.263 \times 10^{1},\ 3.970 \times 10^{2},\ -8.273 \times 10^{-4},\ 2.818 \times 10^{-1},\ 8.550,\ 7.165,\ 4.301,\ 1.515,\ 3.959 \times 10^{2}]$ and the parameter is displaced. The loci of the eigenvalues is shown in Fig. 6.16. In this case $k_{iv1} \approx 80.6$ shows an eigenvalue with real part crossing the positive half plane. Therefore, with the local test it is possible to find a boundary for k_{iv1}. However, it is missing information from the movement of the controller state γ_{v1} (the state remains constant). The test shows a lost of stability with λ_9 and λ_{10}.

6.5 Time domain behavior of the DC microgrid

The time domain behavior of case A is shown in Fig. 6.17. The system uses the complete switched devices. The simulation was carried out with Matlab SimPowersystems tool to ensure accuracy and to validate the obtained results. The sampling time used was T_s=10 μs. The power, current and voltage supplied or consumed by the DGs, ES and Pex devices are shown. The loadability test is used to validate the results of the stability study. The time simulation shows that the system has stable behavior at the operation point (from 7.5 s to 8 s). At 8 s, the system is loaded in i_{g14}, where i_{g14}=4.5 A and the Pex variable $i_{dref} = 6$ A. The stability is maintained during this load increment and the voltage is restored (Fig. 6.17c). At 9 s, the system is loaded again with a grid current $i_{g14} = 6$ A, which is equivalent to i_{dref}=8 A. The regulation of the grid voltage is lost at this load.

It is difficult to correlate the expected oscillation frequency found in the continuation algorithm (*i.e.* $f \approx 557$ Hz, which corresponds to λ_4 and λ_5) with the time behavior presented. Therefore, a Fourier spectrum of a segmented part of the power consumed by the Pex device is shown in Fig. 6.18. The sampling period of this test is $T_s = 0.1$ ms. The time range used for the Fourier representation is $9 < t < 9.5$ s. Furthermore, the frequency component (*i.e.* $f \approx 294$ Hz) of the eigenvalues λ_6 and λ_7 can be observed in the unstable representation.

The time behavior of case B is shown in Fig. 6.19. The behavior of the DC microgrid is presented with power sharing as in case A. Again, the loadability of the system is assessed at the node pcc_5. The time simulation shows that the system has stable behavior at the operation point (from 7.5 s to 8 s). At 8 s, the system is loaded in i_{g14} where i_{g14}=3 A and the Pex variable $i_{dref} = 4$ A. The stability is maintained during this load increment, and the voltage is restored (Fig. 6.19c). However, a low damped oscillation occurs. At 9 s, the system is loaded again with a grid current $i_{g14} = 3.75$ A, which is equivalent to i_{dref}=5 A. The grid voltage v_{g15} oscillates without damping effects at this load.

The Fourier spectrum of the segmented part of the power consumed by the Pex device is shown in Fig. 6.20. This range represents the unstable behavior in case B, the sampling period of this test is $T_s = 1$ ms. The time range used for the Fourier representation is $9 < t < 9.5$ s. The expected oscillation frequency is $f = 57.5$ Hz.

6.6 Final considerations on stability analysis with the continuation algorithm

In this chapter, a stability study of the DC microgrid based on a fixed points continuation method was presented. This method can be applied to multiple converters of the DC microgrid, and enables the limitations of stable operation to be predicted at the design stage. The models can be expanded to handle other loops added to the DC microgrid. A simple model of load has been used in this work to develop the methodology. The aim was to devise a stability test that can handle multiple configurations of a microgrid. A constant impedance type load was used. However, it is important to emphasize that other types of loads such as constant current, constant power or a full dynamic model of power electronic loads can be used with the procedure presented.

The parameters used for the tests were the load at different nodes and the controller gains. The influence of the parameters on the system was tested by

varying their value in a microgrid composed of 2 DG, 1 ES and 1 Pex, which revealed that the states strongly influence the stability estimation.

Some states double in value before reaching the stable boundary. The plot of the eigenvalues resulting from the variation of the selected parameter was used to validate the instability border obtained with each test. Additionally, the continuation method was compared with classical methods of analysis. Finally, the dynamic of each system was coupled to obtain the complete set of differential equations to apply the continuation method.

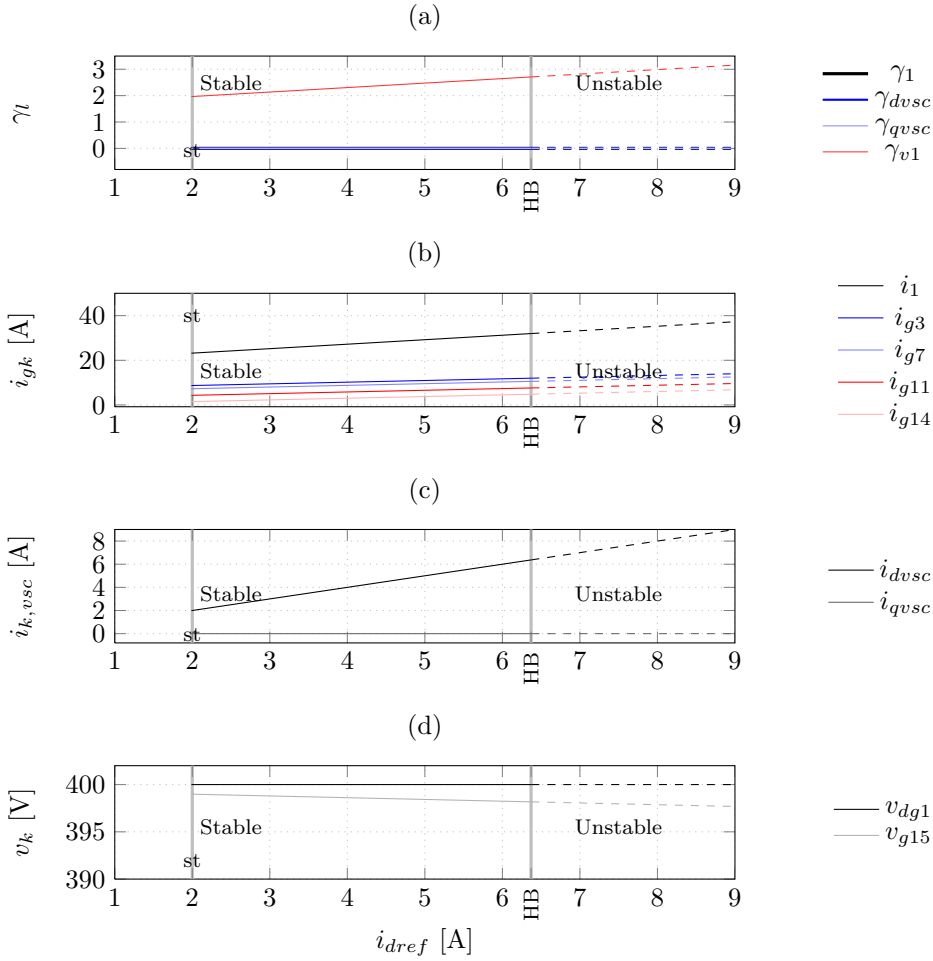

Figure 6.7: Loadability limit for case A, when Pex is increasing.

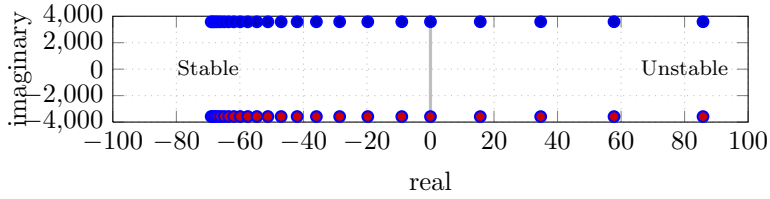

Figure 6.8: Loci of the eigenvalues (λ_4, λ_5) for the loadability limit (case A), when Pex is increasing.

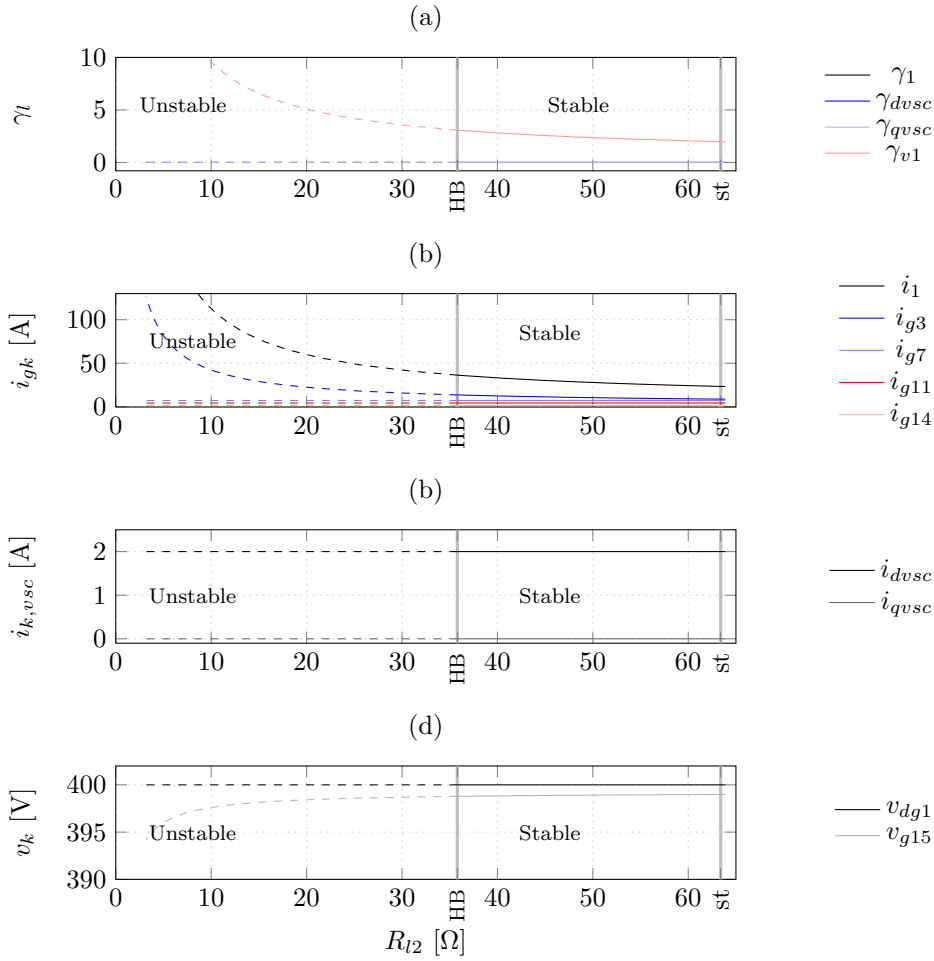

Figure 6.9: Loadability limit, when R_{l2} is decreasing.

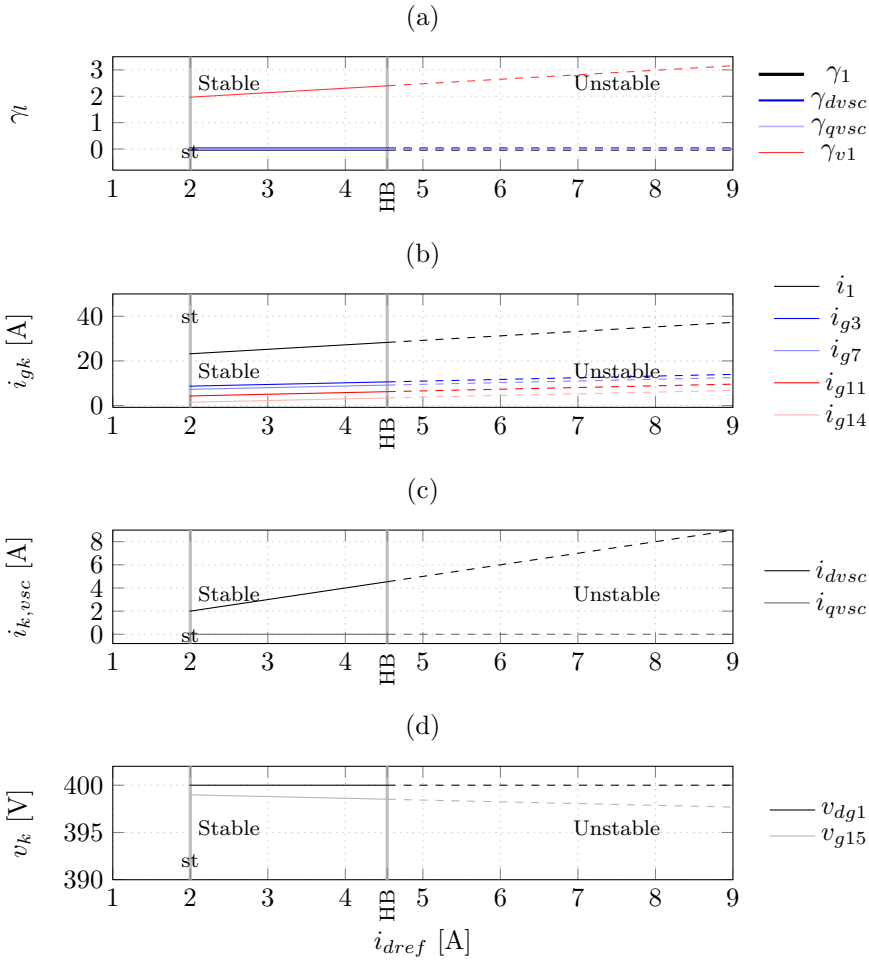

Figure 6.10: Loadability limit for case B, when Pex is increasing.

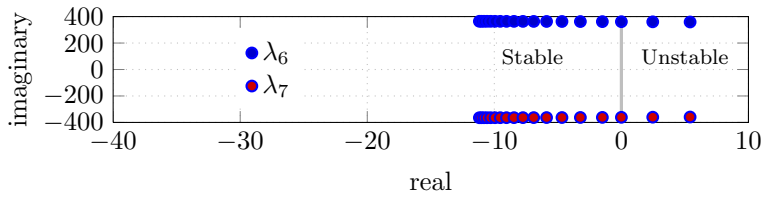

Figure 6.11: Loci eigenvalues (λ_6, λ_7) for the loadability limit (case B), when Pex is increasing.

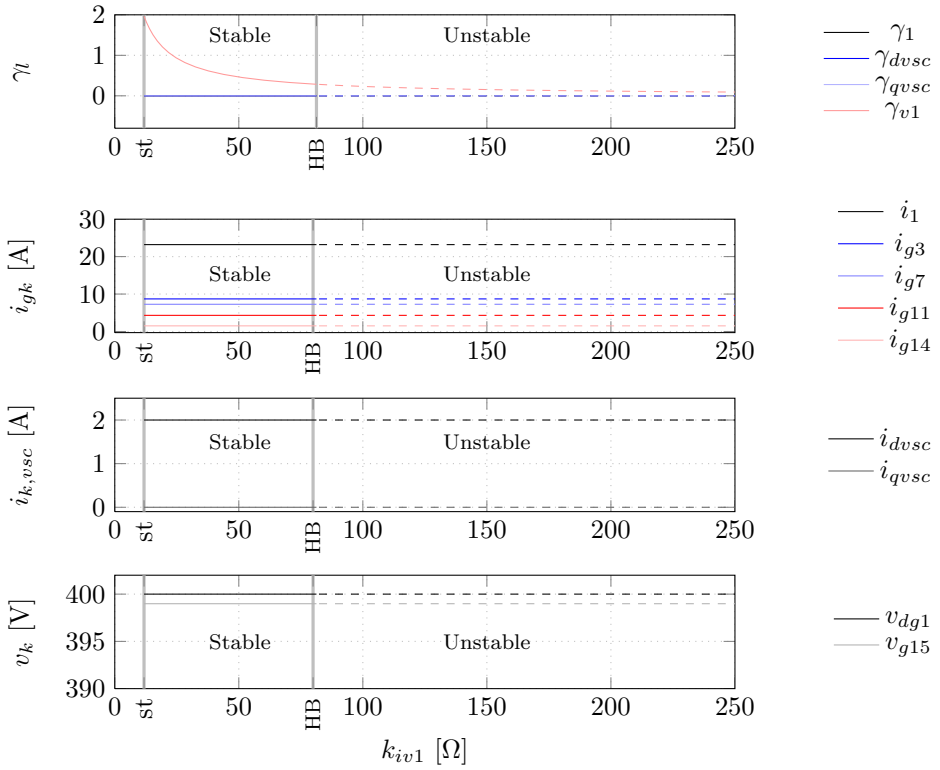

Figure 6.12: Continuation of the states as a function of k_{iv1}.

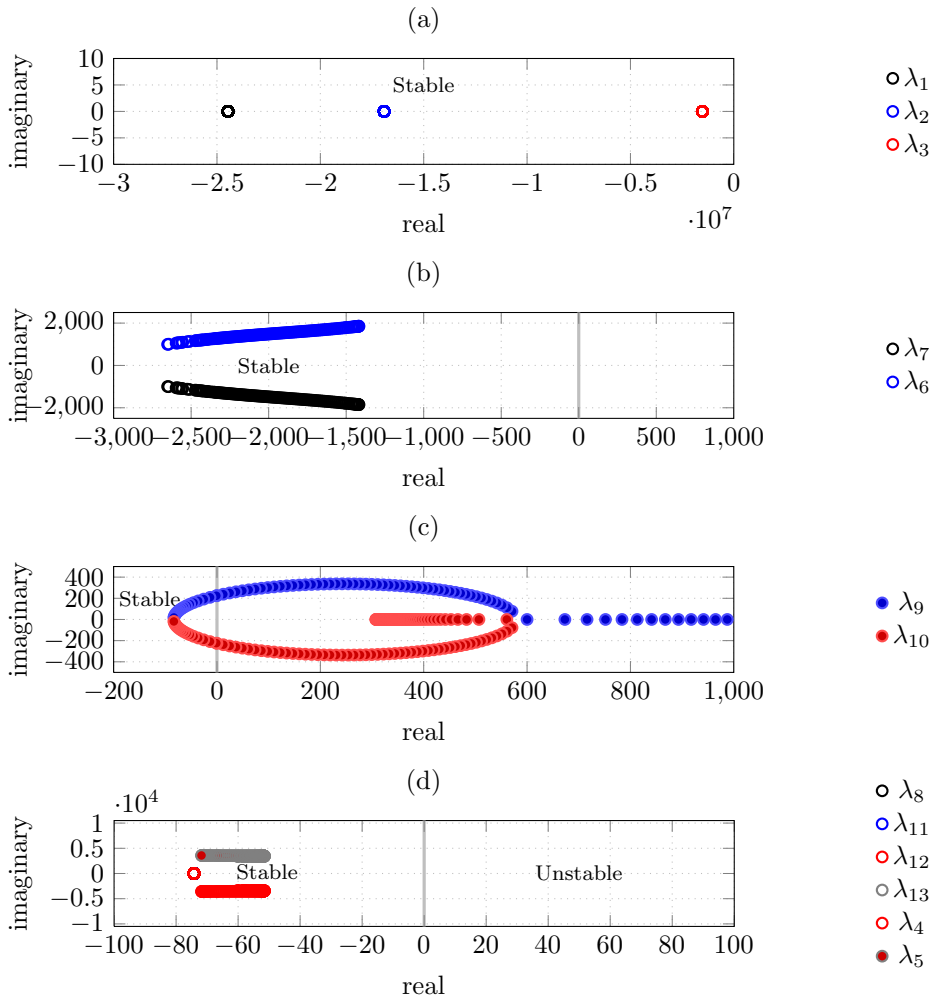

Figure 6.13: Variation of eigenvalues with k_{iv1} movement.

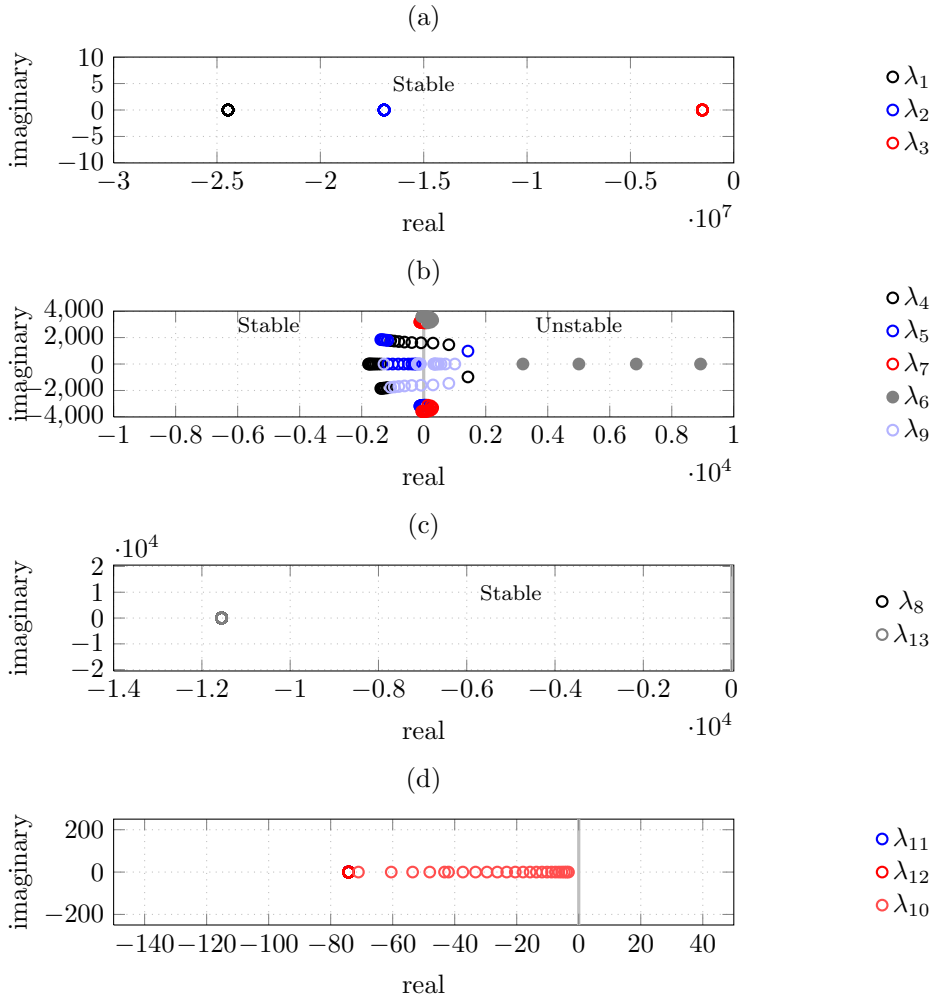

Figure 6.14: Variation of eigenvalues with k_{pv1} movement.

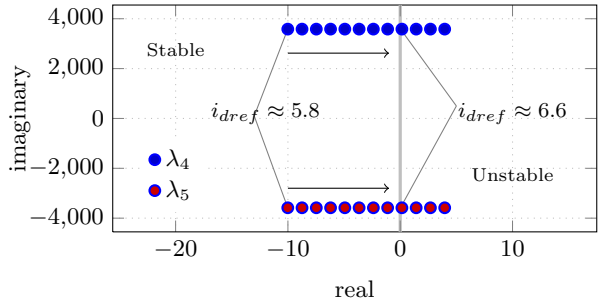

Figure 6.15: Local test for loadability. Eigenvalues (λ_4, λ_5), when Pex is increasing.

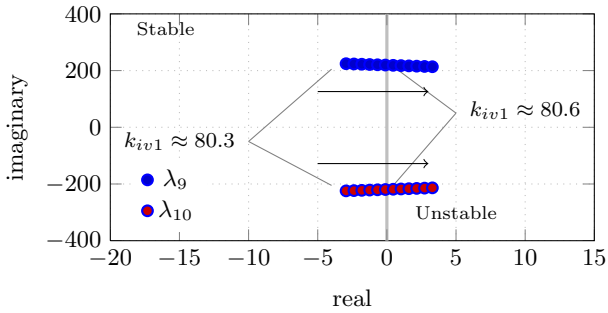

Figure 6.16: Local test for controlability. Eigenvalues (λ_8, λ_9), when k_{iv1} is increasing.

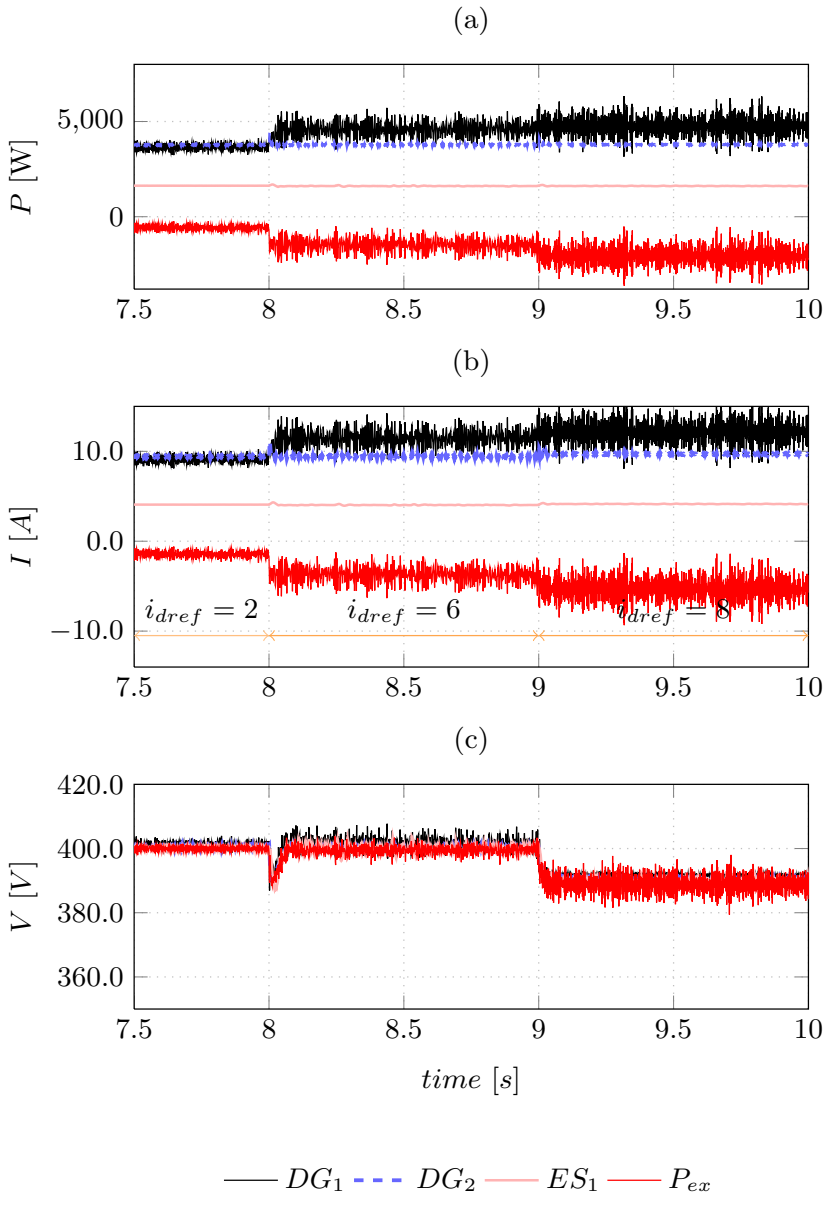

Figure 6.17: Time simulation for case A, loadability I_{dref} test.

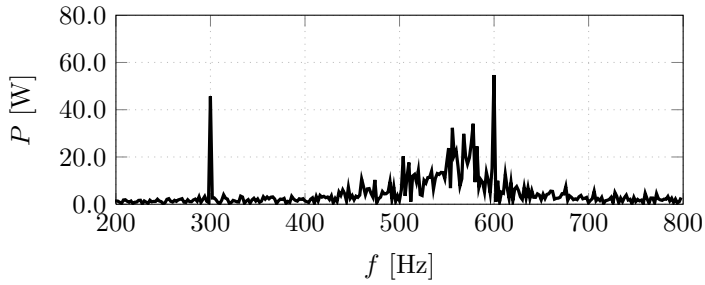

Figure 6.18: Spectrum of the unstable range of the power consumed by Pex.

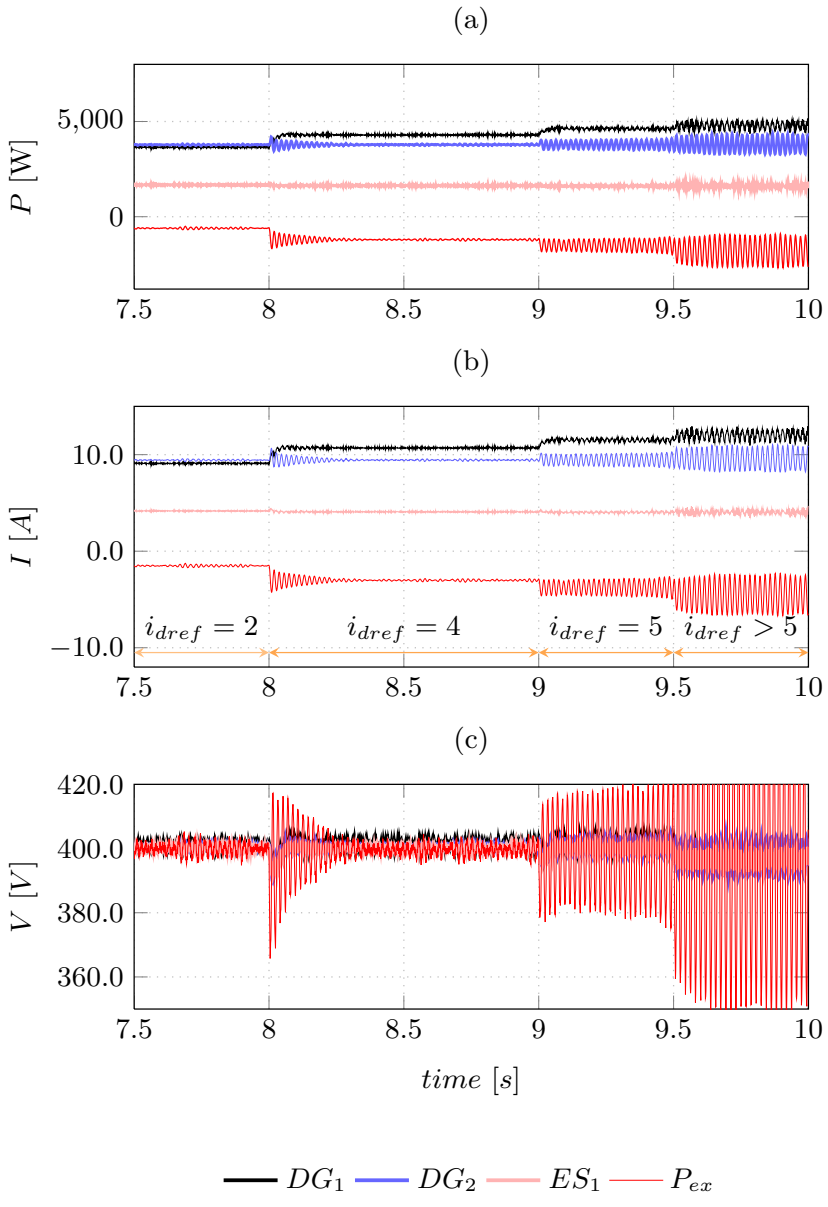

Figure 6.19: Time simulation for case B, loadability I_{dref} test.

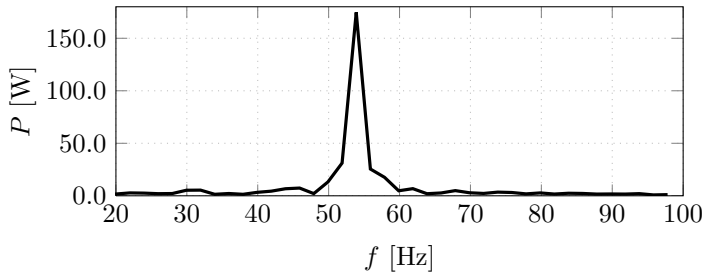

Figure 6.20: Spectrum of the unstable range of the power consumed by Pex.

Chapter 7

Conclusions

This chapter recapitulates the main results of the Thesis and describes recommendations for further work in the field.

7.1 Concluding remarks

One of the main conclusions of this Thesis that the analysis required depends on the information available about the microgrid. If the dynamics of the devices in the microgrid are unknown, then equivalent systems are necessary for the stability test. However, when the dynamics of the devices of the microgrid are known, models such as state-space can be used to perform the stability study. The response of the system in the short- and long-term is used as the principal paradigm.

In this Thesis, the stability at the interconnection point of the power exchanger device was studied by three approaches.

Two types of microgrid equivalent were presented in this research. The first is based on the frequency response, and it uses a range of frequency from the smallest practical perturbation up to half of the switching frequency of the device under test. This linear response is a function of the operation point of the microgrid. One advantage of this method is the use of blackbox modeling. This can be expected in systems with multiple components, where details of the devices are not provided.

Experimental studies were then carried out, which proved the models obtained for the converter used as an exchanger device. As expected, the behavior of the simulation and the analytical and experimental models was similar.

The second estimation of the microgrid equivalent uses the long-term model. It is based on the assumption that at low frequencies, the system will have a typical R-L Thevenin equivalent. A semi-recursive approach was applied here, and the Kalman filter and recursive least square methods were used as mathematical tools. The method was verified with an experimental test. A basic recursive process was developed, which is an advantage of the method to be used on a digital signal processor.

It can be seen from the comparison of the equivalents that at low frequencies, the dynamic of the microgrid presents a characteristic R-L. However, if short-term dynamics are required for the study, the behavior could add a capacitive effect and it is incorrect to consider a simple R-L equivalent as a model of the remaining part of the microgrid.

Finally, if all information about the microgrid is available, then a continuation algorithm can be used to study the loadability and controllability limits of the system. This method examines how the parameters and devices influence the stability of the microgrid. The movement of the states before the boundaries are reached was shown.

7.2 Future work

7.2.1 Short-term

The topology used for this work is based on a radial structure commonly seen in distribution level power systems. Some authors have proposed ring structures for the microgrid. The dynamic characteristics of this topology should also be studied.

A single operation point was used to study the stability of the system. In addition, the power supplied from the converters to the microgrid was considered constantly available. Additional studies that take into account the randomness of renewable sources should be carried out. It is possible to add computational tools such as a Montecarlo simulation to explore the scenarios of power availability from the resources.

7.2.2 Long-term

Further work should be focused on the application of the recursive estimation method to AC microgrids. This analysis can be easily performed with the variables

in the synchronous reference frame.

It is necessary to obtain a physical circuit equivalent as a function of the frequency response of the estimated equivalent impedance.

7.2.3 Hybrid short and long term

It is important to remark that microgrids can operate as supervised systems, where the converters communicate with the management system and an agent can define the power supplied by each source. Therefore, a more detailed stability study with complete hierarchical control over the microgrid can be carried out. It was shown that expansions in the models can be applied and they can handle other loops added to the microgrid

Appendix A

Parameters for simulation studies and experimental set-up

This appendix presents the parameters used in the simulations as well as in the experimental set-up

A.1 Network parameters

Table A.1 presents the parameters of the lines in the DC-AC microgrid. The loads are shown in Table A.2. The benchmark schematic used for the simulation of the microgrid is shown in Fig. A.1.

Table A.1: Line parameters for the microgrid structure.

Parameter	Value [units]
$\text{Line}_{service}$	$r_{(i+1)-i} = 1.380\ \Omega/\text{km}$, $X_{(i+1)-i} = 0.082\ \Omega/\text{km}$
$\text{Line}_{primary}$	$r_{(i+1)-i} = 0.284\ \Omega/\text{km}$, $X_{(i+1)-i} = 83 \times 10^{-3}\ \Omega/\text{km}$
$\text{Line}_{(2)-(1)}$	$r_{le} = 0.041\ \Omega$, $L_{le} = 7.83\ \mu\text{H}$
$\text{Line}_{(3)-(2)}$	$r_{l} = 0.041\ \Omega$, $L_{l} = 7.83\ \mu\text{H}$
$\text{Line}_{(4)-(3)}$	$r_{l2} = 0.041\ \Omega$, $L_{l2} = 7.83\ \mu\text{H}$
$\text{Line}_{(5)-(4)}$	$r_{l3} = 0.123\ \Omega$, $L_{l3} = 23.49\ \mu\text{H} + L_{fvsc}$
$\text{Line}_{(6)-(7)}$	$r_{l6-7} = 0.041\ \Omega$, $L_{l6-7} = 7.83\ \mu\text{H}$
$\text{Line}_{(7)-(8)}$	$r_{l7-8} = 0.00852\ \Omega$, $L_{l7-8} = 0.0025\ \text{H}$

Table A.2: Load parameters for the microgrid equivalent.

Load	Value [units]
R_{l2}	64.00 Ω (2.5 kW)
R_{l3}	32.00 Ω (5.0 kW)
R_{l4}	142.22 Ω (1.125 kW)
$S_{l6,7,8}$	10.0Ω (8 kVA$_{max}$)
$PF_{ACloads}$	0.85_{laggin}

A.2 DC-DC boost converter

DG_1 and DG_2 use a boost converter. The parameters are: $L_b = 0.025$ H, $r_b = 1$ mΩ, $C_b = 651$ μF, $f_{sw} = 3$ kHz. The inner loop gains are $k_{pi} = 95.19$, $k_{ii} = 1.8128 \times 10^5$, the outer loop parameters for voltage control are $k_{pv} = 0.1239$, and $k_{iv} = 11.80$.

A.3 DC-DC bidirectional converter

The parameters for the bidirectional converter are without loss of generality: $L_b = 0.024$ H, $r_b = 1$ mΩ, $C_b = 187.5$ μF, $f_{sw} = 3$ kHz. The inner loop gains are $k_{pi} = 106.609$, and $k_{ii} = 2.3686 \times 10^5$.

A.4 Voltage source converter for inverters at the AC microgrid and Pex between the DC and AC nodes

The parameters are: $L = 6.8$ mH, $r = 0.025$ Ω, $C_{pex} = 133.3$ μF, $w = 2\pi 50$ rad/s, $f_{sw} = 7.875$ kHz. The inner loop gains are $k_{pi} = 79.041$, and $k_{ii} = 5.832 \times 10^3$. The AC capacitor of the LCL filter is $C_{ac} = 24.102$ μF. The voltage controller gains for the AC side of the converters are: $k_{pv} = 0.0052$ and $k_{iv}19.44$.
PLL parameters are: frequency speed $\omega_{ref} = 2\pi 50$ rad/s. The PI controller has the following gains: $k_{p,pll} = 0.4500$ and $T_{i,pll} = 0.0562$.

The cases for the filter inductor at the DC side of the Pex are shown in Table A.3.

Table A.3: Cases for filter inductor at the DC side of the Pex.

Case	Inductor L_{fvsc}
A	0.68 mH
B	68 mH

The per unit design of the inductor is presented in Fig. A.2, the design has been taken from [101], (A.1) presents the equation to obtain the inductor as function of the voltages, switching frequency, current and ripple. In order to obtain high quality power a low ripple has been chosen in this project ($\delta_{\%,ripple} = 4.6$).

$$\left(V_{AC,peak} - \frac{V_{AC,peak}^2}{V_{DC}}\right) = f_{sw} L I_{AC} \delta_{ripple} \tag{A.1}$$

The per unit design of the capacitor is presented in Fig. A.3, the design has been taken from [73], (A.2) presents the equation to obtain the capacitor as function of the voltage, switching frequency, a percentage of the nominal current, modulation index and ripple. In order to obtain high quality power a low ripple has been chosen in this case ($\delta_{\%,vripple} = 5$), the modulation index D is 0.7.

$$C = \frac{D I_{dc}}{f_{sw} \delta_{v,ripple}} \tag{A.2}$$

A.5 Experimental voltage source converter

The parameters of the experimental VSC are: the DC voltage is 400 V, the DC capacitor 2200 μF, the AC filter is composed by a inductor of 3 mH with r=0.0037 Ω and a capacitor 33 μF. The switching frequency is 11 kHz, the controller gains are: $k_p = 13.3262$, and $k_i = 2.96 \times 10^4$.

The three-phase AC load is composed by a resistor bank of 120 Ω. An electronic source has been coupled at the AC side to regulate the voltage. Hence, converter and electronic source share the power supplied to the load.

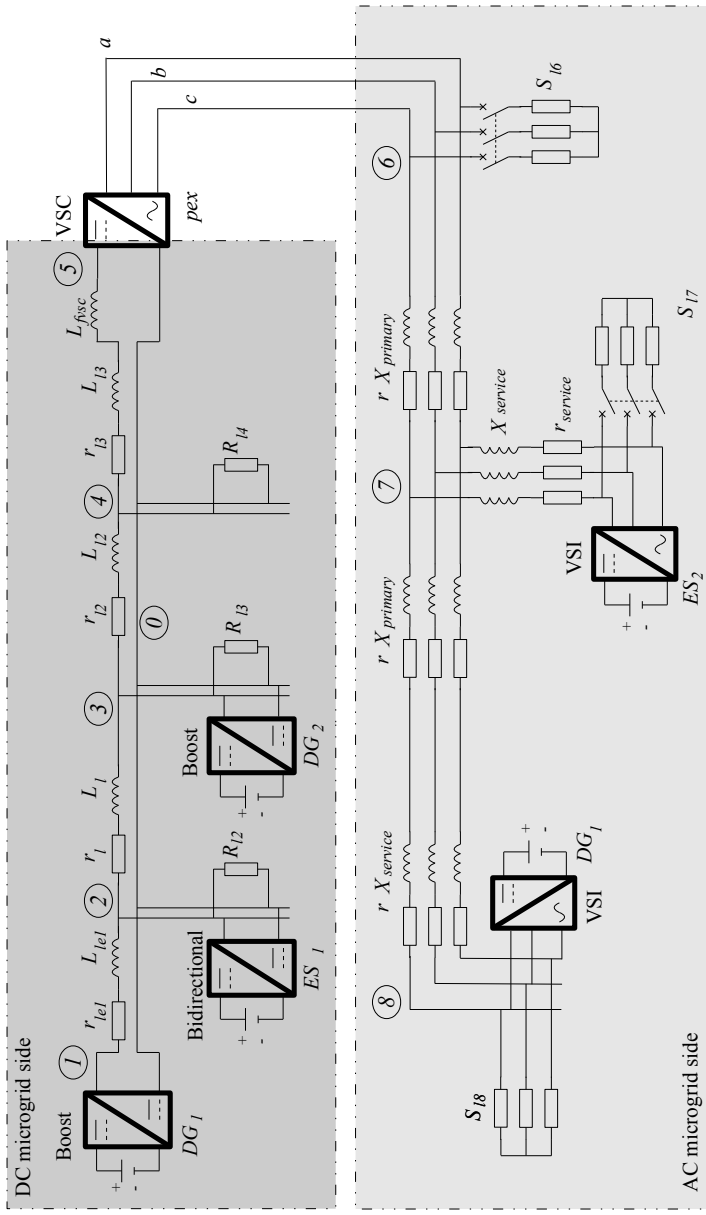

Figure A.1: Circuit diagram of the benchmark microgrid used for simulation.

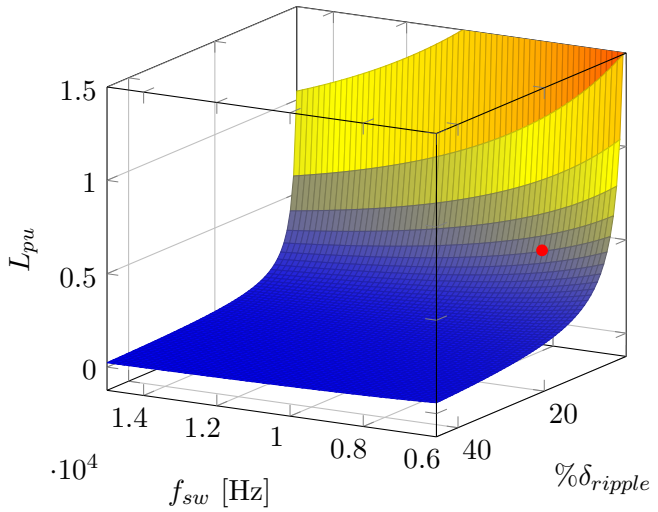

Figure A.2: AC inductor in per unit as function of the switching frequency and % current ripple.

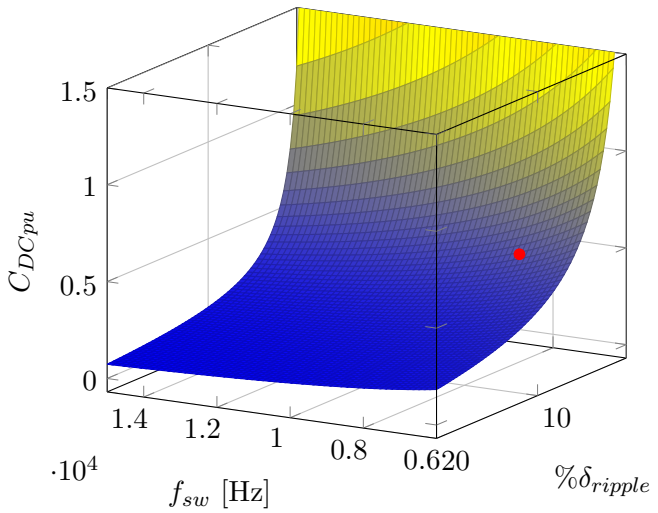

Figure A.3: DC capacitor in per unit as function of the switching frequency and % voltage ripple.

Appendix B

Conditions for the existence of equilibria in systems with constant power load

A lemma that grants the existence of the equilibria of systems with CPLs is described in this chapter, the dynamic equivlaent of the microgrid (i.e. a system linear time–invariant) is used to obtain the maximum power that can be consumed by the CPL. For the case necessary and sufficient conditions for existence of equilibria are given, which give an upper bound on the power dissipated in steady–state that should exceed the extracted constant power. The existence of the equilibrium is ensured if and only if the inequality is satisfied.

B.1 A preliminary lemma

The elementary lemma below is instrumental for further developments. The proof is given in detail, for the sake of completeness.

Lemma 1 *Consider the quadratic equation*

$$m(w) = w^\top S w + w^\top k + c \tag{B.1}$$

where $w \in \mathbb{R}^n$, $S \in \mathbb{R}^{n\times n}$, $S = S^\top > 0$, $k \in \mathbb{R}^n$, $c \in \mathbb{R}$. *There exist a vector* $\bar{w} \in \mathbb{R}^n$ *such that* $m(\bar{w}) = 0$ *if and only if*

$$c \leq \frac{1}{4} k^\top S^{-1} k. \tag{B.2}$$

Moreover, the solution is unique, and is given by $\bar{w} = -\frac{1}{2} S^{-1} k$, *if and only if* $c = \frac{1}{4} k^\top S^{-1} k$.

Proof The function $m(w)$ can be factored as

$$m(w) = (w + \frac{1}{2}S^{-1}k)^\top S(w + \frac{1}{2}S^{-1}k) + c - \frac{1}{4}k^\top S^{-1}k. \tag{B.3}$$

Now $S > 0$, implies that

$$(w + \frac{1}{2}S^{-1}k)^\top S(w + \frac{1}{2}S^{-1}k) \geq 0. \tag{B.4}$$

Let us prove necessity. For, assume $m(\bar{w}) = 0$. In view of (B.4), this clearly implies that (B.2) holds.

To prove sufficiency assume (B.2) holds. Let $d \in \mathbb{R}^n$ be the solution of

$$d^\top Sd = \frac{1}{4}k^\top S^{-1}k - c. \tag{B.5}$$

Then, $\bar{w} = -\frac{1}{2}S^{-1}k + d$ clearly solves $m(\bar{w}) = 0$.

To complete the proof notice that the only solution of (B.5) when $\frac{1}{4}k^\top S^{-1}k = c$ is $d = 0$.

Remark 1 The assumption of positivity of S can be relaxed to sign definite. Indeed, it is clear that, if $S < 0$, the lemma can still be applied multiplying (B.1) by -1.

B.2 Existence of equilibrium points for linear time–invariant systems

In this section we consider multi–input multi–output, square, LTI electrical circuits (*i.e.* as in Fig. B.1) with constant external signals described by the input–output model

$$y(t) = G(p)u(t) + k \tag{B.6}$$

where $p := \frac{d}{dt}$, $\mathrm{R}^{m\times m}(p)$ is the set of $m \times m$ rational matrices with real coefficients, $k \in \mathbb{R}^m$ and the port variables[1] $y, u \in \mathbb{R}^m$—with elements $y_i, u_i,\ i = 1, \ldots, m$—are conjugated variables, *i.e.* $y^\top u$ has units of power. See Fig. B.1. The port variables are connected to CPLs defined as

$$-y_i(t)u_i(t) = P_i > 0,\ i = 1, ..., m, \tag{B.7}$$

[1]In the interest of brevity, when clear from the context, the argument t is omitted from the time functions.

that holds for all $t \geq 0$.

The following assumption on the transfer matrix is in order. See Remark 2 below.

Assumption 1 *The symmetric part of $G(0)$ is sign–definite and, without loss of generality (see Remark 1), we assume is positive definite. That is,*

$$G(0) + G^\top(0) > 0. \tag{B.8}$$

Proposition 1 *The system* (B.6) *with CPLs* (B.7)*, verifying Assumption 1 admits an equilibrium, that is, there exist constant $\bar{u}, \bar{y} \in \mathbb{R}^m$ such that*

$$\begin{aligned} \bar{y} &= G(0)\bar{u} + k \\ \bar{y}^\top \bar{u} &= -\sum_{i=1}^{m} P_i, \end{aligned} \tag{B.9}$$

if and only if

$$\frac{1}{2} k^\top \left[G(0) + G^\top(0) \right]^{-1} k \geq \sum_{i=1}^{m} P_i. \tag{B.10}$$

The equilibrium is unique if and only if (B.10) *holds with identity.*

Proof From (B.9) we get

$$\bar{y}^\top \bar{u} = \frac{1}{2} \bar{u}^\top \left[G(0) + G^\top(0) \right] \bar{u} + \bar{u}^\top k,$$

where only the symmetric part of $G(0)$ is retained in the quadratic (in $\bar{u}$) term. Imposing the CPL condition (B.7) we get the quadratic equation

$$\frac{1}{2} \bar{u}^\top \left[G(0) + G^\top(0) \right] \bar{u} + \bar{u}^\top k \equiv -\sum_{i=1}^{m} P_i, \tag{B.11}$$

The proof is completed invoking Lemma 1 in Section B.1.

Remark 2 Assumption 1 is satisfied if $G(s)$ is the driving point impedance of a circuit consisting of (positive) constant resistors, inductors and capacitors, with the elements of u and y voltages and currents, and k representing constant, external current and voltage sources. In this case $\frac{1}{2} k^\top \left[G(0) + G^\top(0) \right]^{-1} k$ is an upper bound on the power dissipated in steady–state—*i.e.*, the so–called pervasive dissipation—that should exceed the extracted constant power to ensure the existence of equilibria.

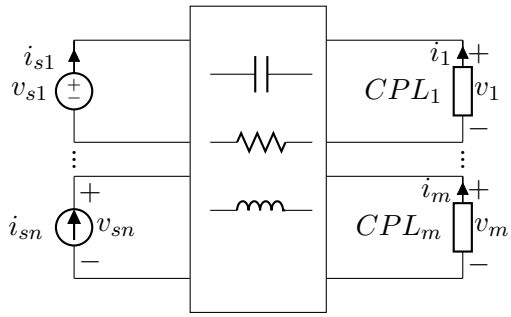

Figure B.1: Graphical description of the circuit (B.6) terminated by CPLs.

Remark 3 The result can also be established using a state space representation for the system. That is,

$$\begin{aligned} \dot{x} &= Ax + Bu \\ y &= Cx + Du + k. \end{aligned} \tag{B.12}$$

where x is the state vector of dimension equal to the McMillan degree[2] of $G(s)$ and A, B, C, D are constant matrices, of suitable dimensions, such that

$$G(s) = C(sI - A)^{-1}B + D.$$

Assumption 1 ensures that A is full rank. In this case, the steady state $\dot{\bar{x}} = 0$ satisfies

$$\bar{x} = -A^{-1}B\bar{u}$$

for some constant $\bar{u} \in \mathbb{R}^m$. Replacing in the system output function yields $\bar{y} = (-CA^{-1}B + D)\bar{u} + k$.
Noting that $-CA^{-1}B + D = G(0)$, the equation above coincides with (B.9).

B.3 Numerical results

The microgrid described in section 3.2 can be represented in matrix form, with state space variables vector $z = [i_{g3}, i_{g7}, i_{g11}, i_{g14}, v_{g15}]^T$, u is the current goin into the Pex. Then, the model is (B.13).

$$\begin{aligned} \dot{z} &= W^{-1}(Az + Bu + E) \\ y &= Cz \end{aligned} \tag{B.13}$$

[2]That is, the dimension of a minimal realization of $G(s)$.

where, $W = diag([L_{e1}, L_l, L_{l2}, L_{l3}, C_{pex}])$, $diag$ means a diagonal matrix. $B = [0, 0, 0, 0, 1]^T$, $E = [v_{g1} - R_{l2}I_{g5},\ -R_{l3}I_{g9} + R_{l2}I_{g5},\ R_{l3}I_{g9},\ 0,\ 0]^T$, and $C = [0, 0, 0, 0, 1]$. The matrix A is described in (B.14).

$$A = \begin{bmatrix} -(R_{l2} + r_{e1}) & R_{l2} & 0 & 0 & 0 \\ R_{l2} & -(R_{l3} + r_l + R_{l2}) & 0 & 0 & 0 \\ 0 & R_{l3} & -(R_{l4} + r_{l2} + R_{l3}) & R_{l4} & 0 \\ 0 & 0 & R_{l4} & -(R_{l4} + r_{l3}) & -1 \\ 0 & 0 & 0 & 1 & 0 \end{bmatrix} \tag{B.14}$$

Defining the matrices $A_o = W^{-1}A$, $B_o = W^{-1}B$, $E_o = W^{-1}E$. To obtain the system as the model in (B.12), the following transformation is realized.

$$z = x - A_o^{-1}k \tag{B.15}$$

$$k = CA_o^{-1}E_o \tag{B.16}$$

The conditions for the existence of the equilibria in the DC network coupled to the CPL device are listed in Table B.1. The two cases of the filter inductor have been considered.

Table B.1: Limits for the existence of equilibria for the DC microgrid with a CPL.

Case	Limit P_{CPL} [kW]
A	161.5
B	161.5

Appendix C

Time simulations for AC power sharing in case B

Figure C.1 presents the active power and reactive power shared by DG_3 and ES_2 at the AC side. Each device produces 5.6 kW of active power and the reactive power is 1 kVAR. The system remains stable as can be seen from the voltage at the node pcc_8 Fig. C.2, it is around 1 pu. The electrical frequency speed is also stable with a value of $2\pi 50$ rad/s.

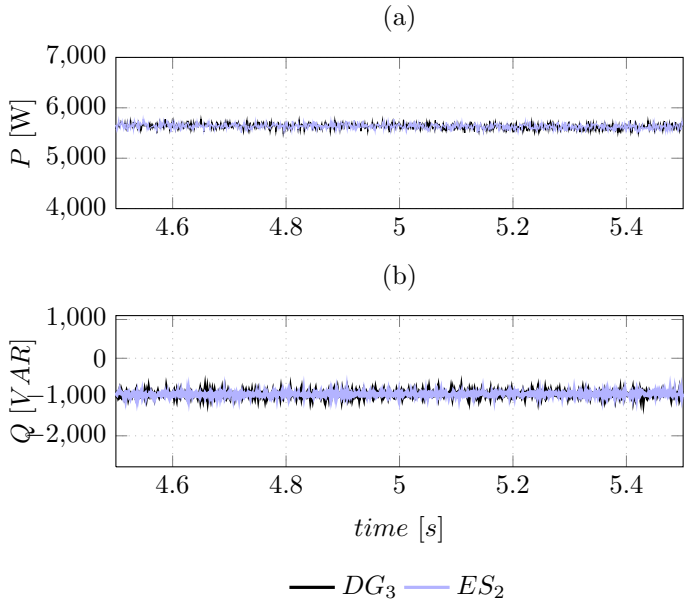

Figure C.1: Power sharing of DGs at the AC side of the microgrid, case B.

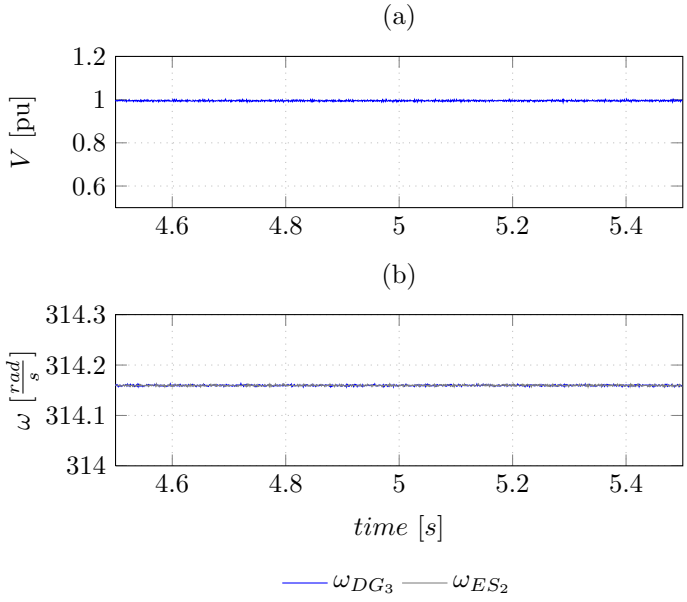

Figure C.2: Voltage at pcc_8 and frequency speed at terminlas of DG_3 and ES_2.

Appendix D

Estimation of a m-order model dynamical equivalent for the DC-microgrid

The tests presented in this section use the data set of section 5.6.4. This test uses different operation points to estimate the dynamic equivalent impedance of the DC microgrid. The order of the estimated parameters has been realized from the first order to a fifth order model. Additionally, the parameter smoother for the KF method has been presented. Finally, a sensitivity analysis of the equivalent DC microgrid circuit has been carried out, this analysis is used in order to understand the possible source of the spikes seen in the current and voltage measurements and finally observed in the $r - L$ estimation.

Figure D.1 presents the parameters ϕ_1 and γ_1 for the discrete system (5.51) using a first order model with KF. The first order model is used for the direct estimation of the $r - L$ impedance equivalent of the DC microgrid. It is shown in Fig. D.1 the spikes that are related with the spikes in Fig. 5.14.

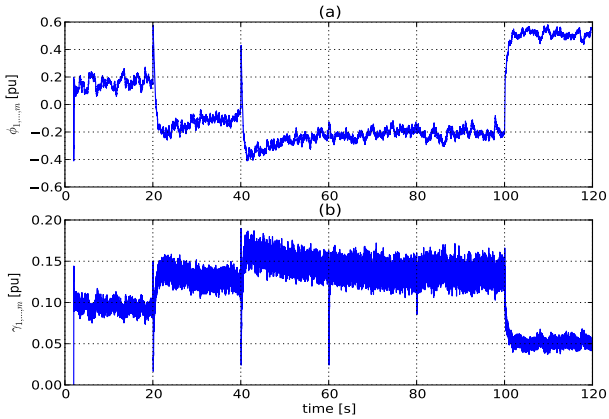

Figure D.1: Estimation parameters for the 1^{st}-order model. Parameter —ϕ_1 (a), parameter —γ_1 (b).

Figure D.2 presents the parameters ϕ_k and γ_k, with $k \in 1, 2$ for the discrete system (5.51) using a second order model. It is easy to verify that the spikes are not presented in the estimation of a second order model.

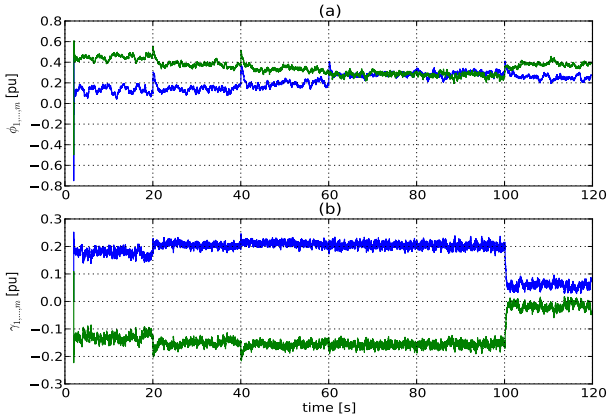

Figure D.2: Estimation parameters for the 2^{nd}-order model. Parameters —ϕ_1, —ϕ_2 (a), parameters —γ_1, —γ_2 (b).

Figure D.3 presents the parameters ϕ_k and γ_k, with $k \in 1, 2, 3$ for the discrete system (5.51) using a third order model.

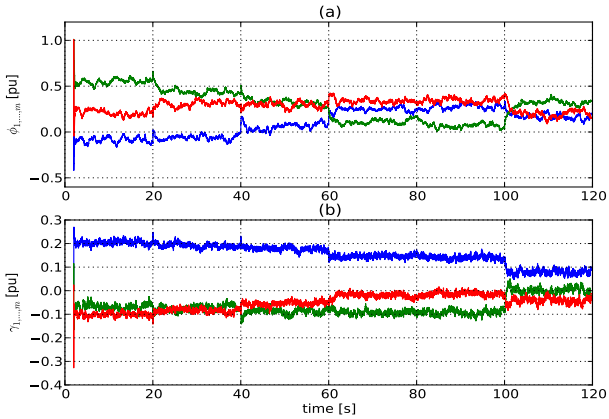

Figure D.3: Estimation parameters for the 3^{rd}-order model. Parameters —ϕ_1, —ϕ_2, —ϕ_3 (a), parameters —γ_1, —γ_2, —γ_3 (b).

The fourth order model is shown in Fig. D.4.

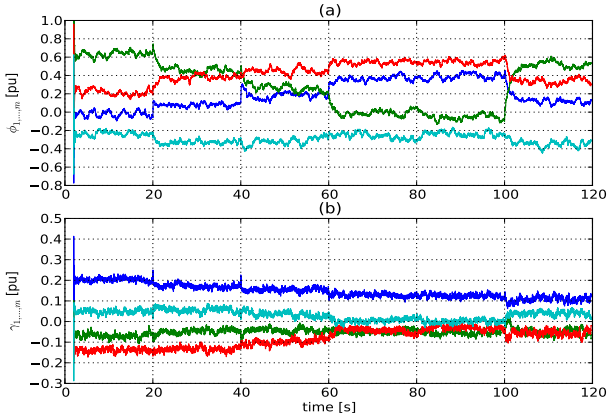

Figure D.4: Estimation parameters for the 4^{th}-order model. Parameters —ϕ_1, —ϕ_2, —ϕ_3, —ϕ_4 (a), parameters —γ_1, —γ_2, —γ_3, —γ_4 (b).

The fifth order model is shown in Fig. D.5.

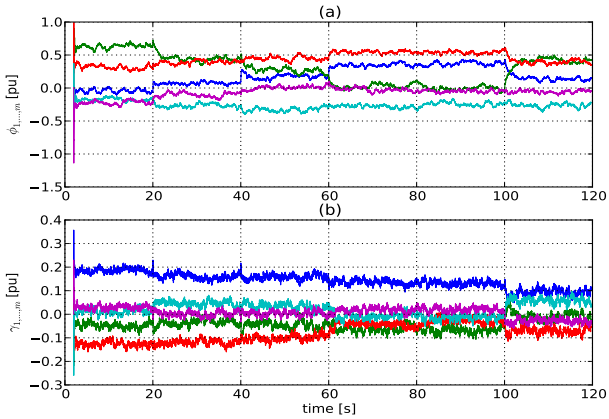

Figure D.5: Estimation parameters for the 5^{th}-order model. Parameters —ϕ_1, —ϕ_2, —ϕ_3, —ϕ_4, —ϕ_5 (a), parameters —γ_1, —γ_2, —γ_3, —γ_4, —γ_5 (b).

Smoothing of the r-L equivalents

It has been observed some spikes at the estimation parameters with KF method for the discrete first order model and the continuous time model (*i.e.* the model with the parameters r and L). This spikes can be related with the fast convergence of the KF method and its sensitivity to sudden changes of the measured values *i.e.* voltage Δv and Δi. One of the methods used in the literature to smooth the response of KF method is the use of the known smoothers [93, 102, 103]. In this section the fixed interval smoother has been used.

The fixed interval smoother is an off-line backward procedure that uses a set of data over the time interval $0 < k \leq N$, where N is the final time and fixed. The smoothed estimates is denoted as $\hat{\theta}_{k\|N}$. The smother method is written as:

$$\Sigma_{k-1}^{sm} = \Sigma_{k-1}[\Sigma_{k\|k-1}]^{-1} \tag{D.1}$$

$$\hat{\theta}_{k-1\|N} = \hat{\theta}_{k-1} + \Sigma_{k-1}^{sm}\left(\hat{\theta}_{k\|N} - \hat{\theta}_{k\|k-1}\right) \tag{D.2}$$

where, Σ_{k-1}^{sm} includes the error covariances stored in the run of KF. Also the parameters estimates $\hat{\theta}_k$ and $\hat{\theta}_{k-1}$ need to be stored. The smoother estimates $\hat{\theta}_{k-1\|N}$ are then obtained by running the stored estimates backward in time by taking $k = N, N-1, ..., 2$. The initialization is with the filtered estimate, that is $\hat{\theta}_{N\|N} = \hat{\theta}_N$.

The results of the application of the smoother on the parameters r and L are shown in Fig. D.6

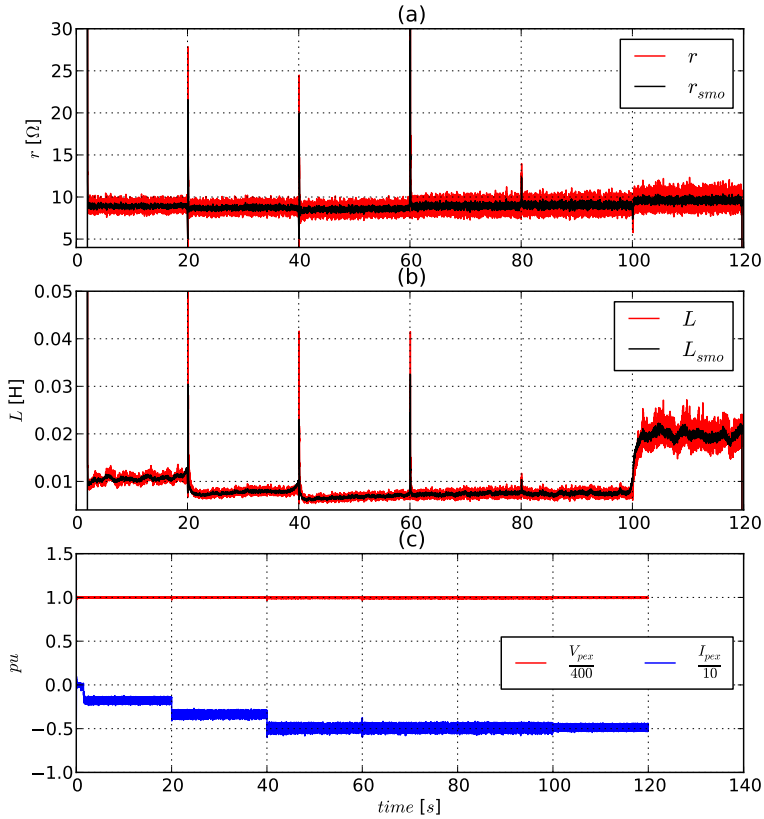

Figure D.6: Smoothed estimation of $r - L$ parameters. Resistance (a), inductor (b), voltage and current at the Pex terminals (c).

Sensitivity analysis of the equivalent DC microgrid system

The estimation of the $r - L$ equivalent impedance for the DC microgrid is based on the measurements of the current and voltage at terminals of the Pex. It has been shown some spikes on the estimation of the $r - L$ parameters at every step change of the operation point. In order to analyse how is the variation of the state variables respect the parameters a sensitivity analysis is required. The dynamic equations of the equivalent system are (D.3)-(D.4). The states of the system are

the current i and the voltage v, the state variable is defined as $x = [x_1, x_2] = [i, v]$.

$$L\frac{di}{dt} = -ri - v + Vs \tag{D.3}$$

$$C\frac{dv}{dt} = i - \frac{P}{v} \tag{D.4}$$

Let us define a vector x_α as the variation of the state variables respect to each parameter in the dynamic model.

$$x_\alpha = \frac{\partial x}{\partial \alpha} \tag{D.5}$$

with $\alpha \in \{r, L, C, P, V_s\}$.

The sensitivity function is obtaining by derivation of the system (D.3) and (D.4) for each parameter α.

$$\frac{dx_\alpha}{dt} = \left[\frac{\partial f}{\partial x}\right] x_\alpha + \left[\frac{\partial f}{\partial \alpha}\right], \; x_\alpha = 0 \tag{D.6}$$

where f is a vector function defined as $f = [\frac{di}{dt}, \; \frac{dv}{dt}]^T$.

Figure D.7 shows that the error for different x_α tends to zero. However, the current is very sensitive to variations on the resistor r (*i.e.* $x_{1,r}$), the power of the Pex and the source voltage V_s. Finally the voltage is sensitive to variations of the power at the Pex, the equivalent resistor r and the source voltage V_s.

Finally, it can be concluded that this spikes are related with the transient changes of the power and the voltage source of the DC microgrid (*i.e.* This voltage is related with the voltage control used in DG_1, this regulates the voltage of the complete DC microgrid). Figure D.8 shows the voltage and current behaviour for the $r - L$ estimation test of the ES_1 trip of chapter 5 (5.6.4). The spikes shows the control of the voltage at every step change every 20 s.

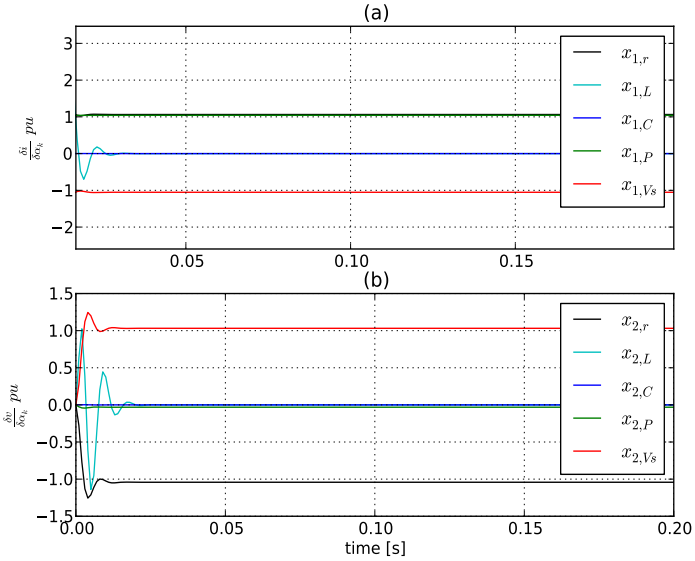

Figure D.7: Sensitivity for the current respect the parameters (a), Sensitivity for the voltage respect the parameters (b).

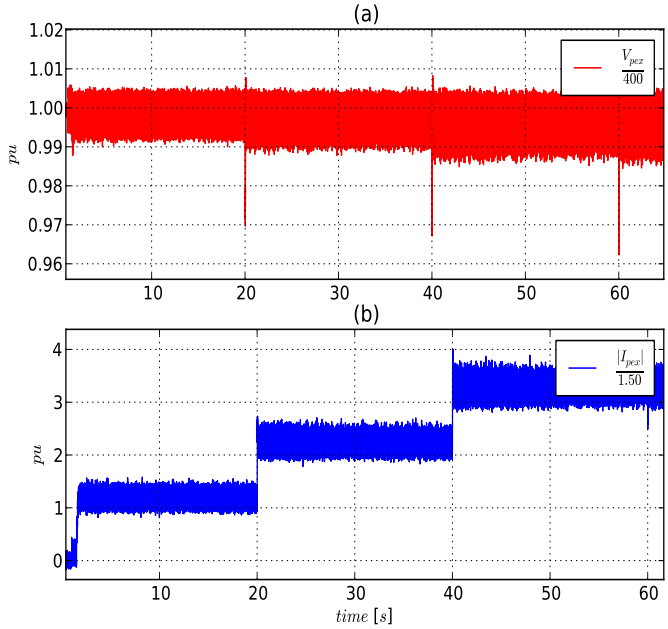

Figure D.8: Voltage at Pex (a), current at Pex (b).

Bibliography

[1] P. Bauer, L. Weldemariam, and E. Raijen, "Stand-alone microgrids," in *Telecommunications Energy Conference (INTELEC), 2011 IEEE 33rd International*, 2011, pp. 1–10.

[2] J. Guerrero, J. Vasquez, J. Matas, L. de Vicuna, and M. Castilla, "Hierarchical control of droop-controlled ac and dc microgrids :a general approach toward standardization," *IEEE Transactions on Industrial Electronics*, vol. 58, no. 1, pp. 158 –172, jan. 2011.

[3] T. Van-Cutsem and C. Vournas, *Voltage stability of electric power systems*. Boston: Kluwer academic publishers, 2001.

[4] L. A. de Sousa Ribeiro, O. R. Saavedra, S. L. de Lima, and J. G. de Matos, "Isolated micro-grids with renewable hybrid generation: The case of lecois island," *IEEE Transactions on sustainable energy*, vol. 2, no. 1, pp. 1–11, January 2011.

[5] P. Basak, A. K. Saha, S. Chowdhury, and S. P. Chowdhury, "Microgrid: Control techniques and modeling," in *Universities Power Engineering Conference (UPEC), 2009 Proceedings of the 44th International*, 2009, pp. 1–5.

[6] S. Sanchez Acevedo and M. Molinas, "Modeling of switching power interfaces for smart-grid stability studies," in *Innovative Smart Grid Technologies (ISGT Europe), 2011 2nd IEEE PES International Conference and Exhibition on*, dec. 2011, pp. 1 –6.

[7] S. Papathanassiou, N. Hatziargyriou, and K. Strunz, "A benchmark low voltage microgrid network," in *CIGRE Symposium*, Apr. 2005, pp. 1–8.

[8] J. Jimeno, J. Anduaga, J. Oyarzabal, and A. G. de Muro, "Architecture of a microgrid energy management system," *Electrical power*, vol. 21, no. 2, pp. 1142–1158, March. 2011.

[9] S. Sanchez, M. Molinas, M. Degano, and P. Zanchetta, "Stability evaluation of a dc micro-grid and future interconnection to an ac system," *Renewable Energy*, vol. 62, no. 0, pp. 649 – 656, 2014. [Online]. Available: http://www.sciencedirect.com/science/article/pii/S096014811300428X

[10] J. Sun, "Small-signal methods for ac distributed power systems-a review," *IEEE Transactions on Power Electronics*, vol. 4, no. 11, pp. 2545–2554, Nov. 2009.

[11] X. Feng, Z. Ye, F. C. Lee, and D. Borojevich, "Pebb system stability margin monitoring," *journal of Vibration and Control*, vol. 8, pp. 261–276, 2002.

[12] S. Sanchez, R. Ortega, R. Grino, G. Bergna, and M. Molinas, "Conditions for existence of equilibria of systems with constant power loads," *Circuits and Systems I: Regular Papers, IEEE Transactions on*, vol. PP, no. 99, pp. 1–8, 2014.

[13] S. Sanchez and M. Molinas, "Assessment of a stability analysis tool for constant power loads in dc-grids," in *15TH International power electronics and motion control conference, EPE-PEMC 2012 ECCE Europe, Novid Sad, Serbia*, sep. 2012, pp. 1 –5.

[14] A. Emadi, A. Khaligh, C. Rivetta, and G. Williamson, "Constant power loads and negative impedance instability in automotive systems: definition, modeling, stability, and control of power electronic converters and motor drives," *Vehicular Technology, IEEE Transactions on*, vol. 55, no. 4, pp. 1112–1125, 2006.

[15] S. Sanchez and M. Molinas, "Evaluation of the system parameters degree of influence on the stability of a dc microgrid," in *PowerTech (POWERTECH), 2013 IEEE Grenoble*, June 2013, pp. 1–5.

[16] J. Jimeno, J. Anduaga, J. Oyarzabal, and A. G. de Muro, "Architecture of a microgrid energy management system," *European Transactions on Electrical Power*, vol. 21, no. 2, pp. 1142–1158, 2011.

[17] H.-M. Kim and T. Kinoshita, "A new challenge of microgrid operation," *Communications in Computer and Information Science*, vol. 78, pp. 250–260, 2010.

[18] M. Ding, Y. Y. Zhang, M. Q. Mao, W. Yang, and X. P. Liu, "Operation optimization for microgrids under centralized control," in *IEEE International Symposium on Power Electronics for Distributed Generation Systems (PEDG), 2010 2nd*, june 2010, pp. 984 –987.

[19] P. Arboleda, D. Diaz, J. M. Guerrero, F. Briz, J. Gonzalez-Moran, and J. Gomez Aleixandre, "An improved control scheme based in droop characteristic for microgrid converters," *Electric power systems research*, no. 80, pp. 1215–1221, 2010.

[20] H. Kakigano, Y. Miura, and T. Ise, "Configuration and control of a dc microgrid for residential houses," in *IEEE Transmision and Distribution conference and Exposition Asia and Pacific*, Oct. 2009, pp. 1–4.

[21] D. Salomonsson and A. Sannino, "Low-voltage dc distribution system for commercial power systems with sensitive electronic loads," *Power Delivery, IEEE Transactions on*, vol. 22, no. 3, pp. 1620–1627, 2007.

[22] M. Baran and N. Mahajan, "Dc distribution for industrial systems: opportunities and challenges," *Industry Applications, IEEE Transactions on*, vol. 39, no. 6, pp. 1596–1601, 2003.

[23] R. Balog and P. Krein, "Bus selection in multibus dc microgrids," *IEEE Transactions on Power Electronics*, vol. 26, no. 3, pp. 860 –867, march 2011.

[24] Y. W. Li and C.-N. Kao, "An accurate power control strategy for power-electronics-interfaced distributed generation units operating in a low-voltage multibus microgrid," *Power Electronics, IEEE Transactions on*, vol. 24, no. 12, pp. 2977–2988, 2009.

[25] X. Liu, P. Wang, and P. C. Loh, "A hybrid ac/dc microgrid and its coordination control," *Smart Grid, IEEE Transactions on*, vol. 2, no. 2, pp. 278–286, 2011.

[26] J. Liu, X. Feng, Z. Ye, F. C. Lee, and D. Borojevich, "Stability monitoring using voltage perturbation for dc distributed power systems," *journal of Vibration and Control*, vol. 8, pp. 277–288, 2002.

[27] K. Areerak, S. Bozhko, G. Asher, L. De Lillo, and D. Thomas, "Stability study for a hybrid ac-dc more-electric aircraft power system," *Aerospace and Electronic Systems, IEEE Transactions on*, vol. 48, no. 1, pp. 329 –347, jan. 2012.

[28] K.-N. Areerak, S. Bozhko, G. Asher, and D. Thomas, "Dq-transformation approach for modelling and stability analysis of ac-dc power system with controlled pwm rectifier and constant power loads," in *Power Electronics and Motion Control Conference, 2008. EPE-PEMC 2008. 13th*, sept. 2008, pp. 2049 –2054.

[29] J. Liu, X. Feng, F. Lee, and D. Borojevich, "Stability margin monitoring for dc distributed power systems via current/voltage perturbation," in *Applied Power Electronics Conference and Exposition, 2001. APEC 2001. Sixteenth Annual IEEE*, vol. 2, March 2001, pp. 745 –751 vol.2.

[30] M. Belkhayat, "Stability criteria for ac power systems with regulated loads," Ph.D. dissertation, Purdue University, 1997.

[31] M. Cespedes and J. Sun, "Renewable energy systems instability involving grid-parallel inverters," in *Applied Power Electronics Conference and Exposition,2009*, February 2009, pp. 1971–1977.

[32] J. Sun and K. J. Karimi, "Small-signal input impedance modeling of line-frecuency rectifiers," *IEEE Transactions on Aerospace and Electronic Systems*, vol. 44, no. 4, pp. 1489–1497, October 2008.

[33] J. Sun and M. Chen, "Analysis and mitigation of interactions between pfc converters and the ac source," in *Power Electronics and Motion Control Conference, 2004. IPEMC*, October 2004, pp. 99–104.

[34] ——, "Low-frequency input impedance modeling of boost single phase pfc converters," *IEEE Transaction on Power Electronics*, vol. 22, no. 4, pp. 1402–1409, july 2007.

[35] J. Sun, "Ac power electronic systems: Stability and power quality," in *Control and Modelling for Power Electronics, 2008. COMPEL 2008. 11th Workshop on*, August 2008, pp. 1–10.

[36] A. Radwan and Y. Mohamed, "Assessment and mitigation of interaction dynamics in hybrid ac/dc distribution generation systems," *Smart Grid, IEEE Transactions on*, vol. 3, no. 3, pp. 1382 –1393, sept. 2012.

[37] S. Danielsen, M. Molinas, T. Toftevaag, and O. B. Fosso, "Constant power load characteristic‘s influence on the low-frequency interaction between advanced electrical rail vehicle and railway traction power supply with rotary converters," in *Modern Electric Traction,2009*, September 2009, pp. 1–6.

[38] M. Molinas, D. moltoni, G. Fscendini, J. A. Suul, R. Faranda, and T. Undeland, "Investigation on the role of power electronic controlled constant power loads for voltage support in distributed ac systems," in *Power Electronics Specialists Conference,2008*, june 2008, pp. 3597–3602.

[39] M. Molinas, J. A. Suul, and T. Undeland, "Low voltage ride trough of wind farms with cage generators: Statcom versus svc," *IEEE Transactions on Power Electronics*, vol. 23, no. 3, pp. 1104–1117, 2008.

[40] J. Segundo-Ramirez, A. Medina, A. Ghosh, and G. Ledwich, "Stability boundary analysis of the dynamic voltage restorer in weak systems with dynamic loads," *International journal of circuit theory and applications*, vol. 40, pp. 551–569, June 2012.

[41] ——, "Stability analysis based on bifurcation theory of the dstatcom operating in current control mode," *IEEE Transaction on Power Delivery*, vol. 24, pp. 1670–1678, july 2009.

[42] S. Sanchez and M. Molinas, "Degree of influence of system states transition on the stability of a dc microgrid," *Smart Grid, IEEE Transactions on*, vol. 5, no. 5, pp. 2535–2542, Sept 2014.

[43] A. Mohd, E. Ortjohann, D. Morton, and O. Omari, "Review of control techniques for inverters parallel operation," *Electric Power System Research*, vol. 80, pp. 1477–1487, 2010.

[44] K. Mizuguchi, S. Muroyama, Y. Kuwata, and Y. Ohashi, "A new decentralized dc power system for telecommunications systems," in *Telecommunications Energy Conference, 1990. INTELEC '90., 12th International*, 1990, pp. 55–62.

[45] A. Griffo and J. Wang, "Large signal stability analysis of 'more electric' aircraft power systems with constant power loads," *IEEE Transactions on Aerospace and Electronic Systems*, vol. 48, no. 1, pp. 477 –489, Jan. 2012.

[46] M. Barnes, J. Kondoh, H. Asano, J. Oyarzabal, G. Ventakaramanan, R. Lasseter, N. Hatziargyriou, and T. Green, "Real-world microgrids-an overview," in *System of Systems Engineering, 2007. SoSE '07. IEEE International Conference on*, 2007, pp. 1–8.

[47] T. Logenthiran, D. Srinivasan, and A. M. Khambadkone, "Multi-agent system for energy resource scheduling of integrated microgrids in a distributed system," *Electric Power Systems Research*, vol. 81, no. 1, pp. 138 – 148, 2011. [Online]. Available: http://www.sciencedirect.com/science/article/pii/S0378779610001823

[48] "Ieee guide for design, operation, and integration of distributed resource island systems with electric power systems," *IEEE Std 1547.4-2011*, pp. 1–54, July 2011.

[49] R. Majumder, M. Dewadasa, A. Ghosh, G. Ledwich, and F. Zare, "Control and protection of a microgrid connected to utility through back-to-back

converters," *Electric Power Systems Research*, vol. 81, no. 7, pp. 1424 – 1435, 2011.

[50] D. J. Cornforth, A. Berry, and T. Moore, "Building a microgrid laboratory," in *IEEE 8th International Conference on Power Electronics and ECCE Asia (ICPE ECCE)*, 30 2011-june 3 2011, pp. 2035 –2042.

[51] N. Hamsic, A. Schmelter, A. Mohd, E. Ortjohann, E. Schultze, A. Tuckey, and J. Zimmermann, "Increasing renewable energy penetration in isolated grids using a flywheel energy storage system," in *Power Engineering, Energy and Electrical Drives, 2007. POWERENG 2007. International Conference on*, April 2007, pp. 195–200.

[52] H. K. Khalil, *Nonlinear Systems*, 2nd ed. United States of America: Prentice Hall, 1996.

[53] L. Harnefors, M. Bongiorno, and S. Lundberg, "Input-admittance calculation and shaping for controlled voltage-source converters," *Industrial Electronics, IEEE Transactions on*, vol. 54, no. 6, pp. 3323 –3334, dec. 2007.

[54] S. Iyer, M. Belur, and M. Chandorkar, "A generalized computational method to determine stability of a multi-inverter microgrid," *Power Electronics, IEEE Transactions on*, vol. 25, no. 9, pp. 2420–2432, 2010.

[55] A. Ghosh and G. Ledwich, "Stability of hysteretic controlled voltage source converters in a power system," in *Innovative Smart Grid Technologies Asia (ISGT), 2011 IEEE PES*, Nov 2011, pp. 1–8.

[56] T. Bashkow, "The a matrix, new network description," *Circuit Theory, IRE Transactions on*, vol. 4, no. 3, pp. 117–119, Sep 1957.

[57] L. Weiss, W. Mathis, and L. Trajkovic, "A generalization of brayton-moser's mixed potential function," *Circuits and Systems I: Fundamental Theory and Applications, IEEE Transactions on*, vol. 45, no. 4, pp. 423–427, 1998.

[58] A. Dobakhshari, S. Azizi, and A. Ranjbar, "Control of microgrids: Aspects and prospects," in *IEEE International Conference on Networking, Sensing and Control (ICNSC), 2011*, april 2011, pp. 38 –43.

[59] J. Guerrero, J. Vasquez, J. Matas, M. Castilla, and L. de Vicuna, "Control strategy for flexible microgrid based on parallel line-interactive ups systems," *Industrial Electronics, IEEE Transactions on*, vol. 56, no. 3, pp. 726–736, March 2009.

[60] P. Kundur, *power System Stability and Control*. United States of America: McGraw-Hill, 1993.

[61] K. De Brabandere, K. Vanthournout, J. Driesen, G. Deconinck, and R. Belmans, "Control of microgrids," in *Proc of IEEE Power Engineering Society General Meeting, 2007.*, june 2007, pp. 1 –7.

[62] H. Kakigano, Y. Miura, and T. Ise, "Distribution voltage control for dc microgrids using fuzzy control and gain-scheduling technique," *Power Electronics, IEEE Transactions on*, vol. 28, no. 5, pp. 2246–2258, 2013.

[63] K. J. Åström and T. Hägglund, *Advanced PID Control*. Research Triangle Park, NC 27709: ISA - The Instrumentation, Systems, and Automation Society, 2005.

[64] M. Delghavi and A. Yazdani, "A control strategy for islanded operation of a distributed resource (dr) unit," in *Power Energy Society General Meeting, 2009. PES '09. IEEE*, July 2009, pp. 1–8.

[65] G.-C. Hsieh and J. Hung, "Phase-locked loop techniques. a survey," *Industrial Electronics, IEEE Transactions on*, vol. 43, no. 6, pp. 609–615, Dec 1996.

[66] M. Prodanovic, T. Green, and H. Mansir, "A survey of control methods for three-phase inverters in parallel connection," in *Power Electronics and Variable Speed Drives, 2000. Eighth International Conference on (IEE Conf. Publ. No. 475)*, 2000, pp. 472–477.

[67] J. Machowski, J. W. Bialek, and J. R. Bumby, *Power system dynamics, stability and control*, 2nd ed. New Delhi: Wiley, 2008.

[68] M. Shahidehpour and M. Khodayar, "Cutting campus energy costs with hierarchical control: The economical and reliable operation of a microgrid," *Electrification Magazine, IEEE*, vol. 1, no. 1, pp. 40–56, Sept 2013.

[69] K. Siri, C. Q. Lee, and T. F. Wu, "Current distribution control for parallel connected converters. i," *Aerospace and Electronic Systems, IEEE Transactions on*, vol. 28, no. 3, pp. 829–840, Jul 1992.

[70] J. Sun, "Impedance-based stability criterion for grid-connected inverters," *Power Electronics, IEEE Transactions on*, vol. 26, no. 11, pp. 3075–3078, Nov 2011.

[71] S. Girinon, C. Baumann, H. Piquet, and N. Roux, "Analytical modeling of the input admittance of an electric drive for stability analysis purposes," *European physical journal*, vol. 47, no. 1, pp. 1 –8, jul. 2009.

[72] A. Gelb and W. E. Vander Velde, *Multiple-Input Describing Functions and Nonlinear system Design.* United States of America: McGraw-Hill, 1968.

[73] N. Mohan, T. M. Undeland, and W. P. Robbins, *power Electronics, converters, applications, and design*, 3rd ed. United States of America: John Willey & Sons, 2003.

[74] N. Mohan, *first course on power electronics and dirves.* United States of America: MNPERE, 2003.

[75] J. Huang, K. Corzine, and M. Belkhayat, "Small-signal impedance measurement of power-electronics-based ac power systems using line-to-line current injection," *Power Electronics, IEEE Transactions on*, vol. 24, no. 2, pp. 445–455, Feb 2009.

[76] Z. Bing, K. Karimi, and J. Sun, "Input impedance modeling and analysis of line-commutated rectifiers," *Power Electronics, IEEE Transactions on*, vol. 24, no. 10, pp. 2338–2346, Oct 2009.

[77] S. Sanchez and M. Molinas, "Assessing the validity of a propose stability analysis method in a three phase system with constant power load," in *Power Electronics for Distributed Generation Systems (PEDG), 2012 3rd IEEE International Symposium on*, june 2012, pp. 41 –45.

[78] S. Cobreces, E. Bueno, D. Pizarro, F. Rodriguez, and F. Huerta, "Grid impedance monitoring system for distributed power generation electronic interfaces," *Instrumentation and Measurement, IEEE Transactions on*, vol. 58, no. 9, pp. 3112 –3121, sept. 2009.

[79] I. Cvetkovic, D. Boroyevich, D. Dong, P. Mattavelli, R. Burgos, M. Jaksic, G. Francis, Z. Shen, S. Ahmed, and F. Wang, "Dynamic interactions in hybrid ac/dc electronic power distribution systems," in *Power Electronics and ECCE Asia (ICPE ECCE), 2011 IEEE 8th International Conference on*, june 2011, pp. 2121 –2128.

[80] L. Asiminoaei, R. Teodorescu, F. Blaabjerg, and U. Borup, "Implementation and test of an online embedded grid impedance estimation technique for pv inverters," *Industrial Electronics, IEEE Transactions on*, vol. 52, no. 4, pp. 1136 – 1144, aug. 2005.

[81] ——, "A digital controlled pv-inverter with grid impedance estimation for ens detection," *Power Electronics, IEEE Transactions on*, vol. 20, no. 6, pp. 1480 – 1490, nov. 2005.

[82] M. Liserre, F. Blaabjerg, and R. Teodorescu, "Grid impedance estimation via excitation of lcl -filter resonance," *Industry Applications, IEEE Transactions on*, vol. 43, no. 5, pp. 1401 –1407, sept.-oct. 2007.

[83] M. Sumner, B. Palethorpe, D. Thomas, P. Zanchetta, and M. Di Piazza, "A technique for power supply harmonic impedance estimation using a controlled voltage disturbance," *Power Electronics, IEEE Transactions on*, vol. 17, no. 2, pp. 207 –215, mar 2002.

[84] M. Ciobotaru, R. Teodorescu, P. Rodriguez, A. Timbus, and F. Blaabjerg, "Online grid impedance estimation for single-phase grid-connected systems using pq variations," in *Power Electronics Specialists Conference, 2007. PESC 2007*, no. 11, Jun. 2007, pp. 2306–2312.

[85] S. Cobreces, P. Rodriguez, D. Pizarro, F. Rodriguez, and E. Bueno, "Complex-space recursive least squares power system identification," in *Power Electronics Specialists Conference, 2007. PESC 2007. IEEE*, june 2007, pp. 2478 –2484.

[86] G. G. C. and S. K. S., *Adaptive Filtering Prediction and Control*. New Jersey: Prentice-Hall, 1984.

[87] R. F. Stengel, *Optimal control and estimation*. New York: Dover, 1994.

[88] H. Kakigano, Y. Miura, and T. Ise, "Low-voltage bipolar type dc microgrid for super high quality distribution," *IEEE Transactions on Power Electronics*, vol. 25, no. 12, pp. 3066–3075, 2010.

[89] C. K. Tse, *Complex behavior of switching power converters*. United States of America: CRC, 2003.

[90] A. H. Nayfeh and B. Balachandran, *Applied nonlinear dynamics: analytical, computational, and experimental methods*. Germany: Wiley series, 2004.

[91] S. Sastry, *Nonlinear Systems: Analysis, Stability, and Control*. New York: Springer, 1999.

[92] L. Ljung, *System identifiaton, Theory for the user*, 2nd ed. Sweden: Prentice-Hall, 1999.

[93] B. D. O. Anderson and J. B. Moore, *Optimal Filtering*. New Jersey: Prentice-Hall, 1979.

[94] "Experimental verification of a voltage droop control for grid integration of offshore wind farms using multi-terminal hvdc," *Energy Procedia*, vol. 53, no. 0, pp. 104 – 113, 2014.

[95] V. Ajjarapu, *Computational techniques for voltage stability assessment and control*. New York: Springer, 2006.

[96] C. Guoyun, D. Hill, and R. Hui, "Continuation of local bifurcations for power system differential-algebraic equation stability model," *Generation, Transmission and Distribution, IEE Proceedings-*, vol. 152, no. 4, pp. 575–580, 2005.

[97] S. Development Team, "Sympy in python," http://http://sympy.org/, 2013.

[98] K. William H., *distribution system modeling and analysis*. New York: CRC press, 2001.

[99] O. Katsuhiko, *Modern control engineering*. New Jersey, 07458: Prentice Hall, 1997.

[100] M. Hernandez-Gomez, R. Ortega, F. Lamnabhi-Lagarrigue, and G. Escobar, "Adaptive pi stabilization of switched power converters," *IEEE Trans. Control Syst. Technology*, vol. 18, no. 3, pp. 688–698, 2010.

[101] T. Friedli, J. Kolar, J. Rodriguez, and P. Wheeler, "Comparative evaluation of three-phase ac-ac matrix converter and voltage dc-link back-to-back converter systems," *Industrial Electronics, IEEE Transactions on*, vol. 59, no. 12, pp. 4487–4510, Dec 2012.

[102] M. Tarvainen, J. Hiltunen, P. Ranta-aho, and P. A. Karjalainen, "Estimation of nonstationary eeg with kalman smoother approach: an application to event-related synchronization (ers)," *Biomedical Engineering, IEEE Transactions on*, vol. 51, no. 3, pp. 516–524, March 2004.

[103] S. S. Haykin, *Kalman Filtering and Neural Networks*. New York, NY, USA: John Wiley & Sons, Inc., 2001.